

© 2012 Taejin Min

QUANTITATIVE INVESTIGATION OF BACTERIAL CHEMOTAXIS
AT THE SINGLE-CELL LEVEL

BY

TAEJIN MIN

DISSERTATION

Submitted in partial fulfillment of the requirements
for the degree of Doctor of Philosophy in Physics
in the Graduate College of the
University of Illinois at Urbana-Champaign, 2012

Urbana, Illinois

Doctoral Committee:

Professor Taekjip Ha, Chair
Assistant Professor Yann R. Chemla, Director of Research
Professor Nigel D. Goldenfeld
Professor John D. Stack

Abstract

Living cells sense and respond to constantly changing environmental conditions. Depending on the type of stimuli, the cell may respond by altering gene expression pattern, secreting molecules, or migrating to a different environment. Directed movement of cells in response to chemical stimuli is called chemotaxis.

In bacterial chemotaxis, small extracellular molecules bind receptor proteins embedded in the cell membrane, which then transmit the signal inside the cell through a cascade of protein-protein interactions. This chain of events influences the behavior of motor proteins that drive the rotation of helical filaments called flagella. Individual cells of the gut-dwelling bacteria *Escherichia coli* (*E. coli*) have many such flagella, whose collective action results in the swimming behavior of the cell. A recent study found that in absence of chemical stimuli, fluctuations in the protein cascade can cause non-Poissonian switching behavior in the flagellar motor (2). A corollary was that extension of such behavior to the whole-cell swimming level would have implications for *E. coli*'s foraging strategy. However, existence of such behavior at the swimming cell level could not be predicted a priori, since the mapping from single flagellum behavior to the swimming behavior of a multi-flagellated cell is complex and poorly understood (3, 4).

Here we characterize the chemotactic behavior of swimming *E. coli* cells using a novel optical trap-based measurement technique. This technique allows us to trap individual cells and monitor their swimming behavior over long time periods with high temporal resolution. We find that swimming cells exhibit non-Poissonian switching statistics between different swimming states, in a manner similar to the rotational direction-switching behavior seen in individual flagella. Furthermore, we develop a data analysis routine that allows us to characterize higher order swimming features such as reversal of swimming direction and existence of multiple swimming speeds.

When stimulated with a step-increase in chemo-attractants, *E. coli* cells initially respond by reducing the frequency of swimming direction change. Over time, however, cells return to their pre-stimulus behavior despite the increased chemo-attractant concentration in the environment. This process is called chemotactic adaptation. Adaptation allows cells to maintain chemotactic sensitivity over a wide range of background chemical concentrations.

We study chemotactic adaptation of *E. coli* at the individual cell level using our optical trapping method. Chemical stimuli were delivered from the chemical gradient established in a custom-made laminar flow device. We observe two striking features of individual cell's adaptation and their dependence on stimulus strength. We also observe asymmetry between responses to positive and negative stimuli. Existing evidence and theoretical models suggest that the observed features of single-cell adaptation and their dependence on stimulus strength may be explained in terms of interactions of neighboring receptor proteins in large clusters. Further experiments using various mutant strains of *E. coli* would shed light on the molecular-level mechanisms of the observed behavior.

To my parents

Acknowledgements

I would like to extend my sincere gratitude to my advisor Professor Yann Chemla. Yann took me as a rotation student right when I arrived at UIUC and opened my eyes to the study of single molecules using high-resolution optical tweezers. I was fortunate enough to join the lab at a time when Yann was available to give hands-on help in the lab, and what I observed of Yann's technique at the time made a lasting impact on my conduct as an experimental scientist. All of subsequent training Yann knowingly and unknowingly provided by example – in programming, calculations, data analysis, and presentation of data – shaped me as a scientist that I am today.

I would like to extend my sincere gratitude to my co-advisor Professor Ido Golding. Ido took me as a rotation student during my first term and introduced me to the study of single bacteria using quantitative microscopy. Ido's uncompromising standards in the conduct of scientific research shaped my way of thinking and caught me off-guard when I was sloppy. Coupled with his warm personality, Ido's tireless passion for the pursuit of discovery provided a constant source of inspiration. I thank Ido especially for continuing to invest his utmost attention and dedication, and always making his time available despite the distance after his move.

I would like to also mention how grateful I am that Yann and Ido provided a training environment that included everything that I dreamed of as an undergraduate interested in both physics and biology – building instruments, high-resolution measurements, modeling biological systems, quantitative data analysis, giving talks at conferences – and much more, in a collegial team-environment.

I would like to extend special thanks to a fellow graduate student Patrick Mears. From the beginning, Patrick and I worked together on the *E. coli* chemotaxis project, sometimes dividing up different tasks, and other times sitting next to each other doing experiments together. Patrick was always available to bounce scientific ideas off of and figure things out together, and also to consult on all kinds of issues outside of science. My progress as a graduate student and an individual would be nowhere near where it is now without Patrick's help and influence.

I would also like to extend special thanks to Dr. Matt Comstock. Matt joined Yann's research group as a postdoc early on in my graduate career and provided countless advice and help in all matters scientific and non-scientific. Matt was never selfish with his time and I could always count on Matt to have the correct knowledge and/or more experienced perspective on things.

I would like to thank members of Chemla lab and Golding lab: Rustem Khafizov, Markita Landry, Zhi Qi, Sukrit Suksombat, Vishal Kottadiel, Kevin Whitley, Kiran Girdhar, Chenghang Zong, Lanying Zeng, Eli Rothenberg, Tommy So, Leonardo Sepulveda, Sam Skinner, and Heng Xu. They provided numerous help along the way and a very friendly and collaborative environment in which to conduct research. I also thank many members of Ha lab and Selvin lab, and students in the physics department and the biophysics program that I had close friendship with. I could not have survived graduate school without these individuals.

I would like to thank our collaborator Professor Chris Rao and his students Lon Chubiz and Supreet Saini for their help with constructing *E. coli* strains and providing expertise in bacterial

chemotaxis. I would also like to thank researchers in the *E. coli* chemotaxis field who provided gifts of strains and helpful comments on our studies: Professor Howard Berg, Professor Richard Berry, Professor Philippe Cluzel, and Professor John Parkinson.

I would like to thank my thesis committee members. I thank Professor Ha for his constant encouragement and the inspiration I take from him. I thank Professor Nigel Goldenfeld for his continued interest, attention, and stimulating discussions on my thesis project. I thank Professor John Stack for his warm encouragements on my prelim and final exams and his careful examination of my studies.

I thank Molecular Biophysics Training Grant (MBTG) for supporting the first three years of my studies, and Center for the Physics of Living cells (CPLC) for supporting me through the remaining years and providing funding to build a dedicated optical tweezers instrument. MBTG and CPLC also gave me opportunities to hone my leadership skills as a student symposium organizer and a summer school teaching assistant.

Lastly, but most importantly, I thank my family. Despite hardships as first generation immigrants, my parents always encouraged me to pursue my interests and dreams. They consoled me when I had difficulties and shared my joy when I had good news. The unconditional love and emotional support my parents and older brother provided over my lifetime cannot be described in words.

I thank In Hwa (Christine) Jun with love for lighting up my world since our first encounter and continuing to do so.

Table of Contents

Chapter 1. Background	1
1.1. Bacterial chemotaxis and why we study it	1
1.2. Importance of chemotaxis to bacteria	2
1.2.1. Chemotaxis confers dispersal advantages	2
1.2.2. Chemotaxis facilitates invasion of host organisms by bacteria	3
1.3. <i>E. coli</i> chemotaxis	3
1.3.1. <i>E. coli</i> as a microscopic swimmer	3
1.3.2. How <i>E. coli</i> cells respond to environmental stimuli	4
1.3.3. <i>E. coli</i> chemotaxis network	6
1.4. Studying chemotaxis at the single-cell level	7
1.4.1. Individuality in bacteria provides motivation for single cell studies	7
1.4.2. Individual <i>E. coli</i> cells show long-term fluctuations in chemotactic behavior	8
1.4.3. A new technique is needed to study chemotaxis at the single-cell level	8
1.5. Scope of this thesis	9
Chapter 2. Measurement of bacterial motility using optical tweezers	11
2.1. Introduction to optical trapping in biology	11
2.1.1. Physical principles of optical trapping	11
2.1.2. Application of optical traps in biology	11
2.1.3. Photo-induced damage and heating	12
2.2. Description of the optical trapping method	13
2.2.1. Optical trap instrument design	13
2.2.2. Trapping medium	14
2.2.3. Trapping chamber	16
2.2.4. Experimental procedure	16
2.3. Swimming signal measurement and data analysis	17
2.3.1. Swimming signal observed from trapped <i>E. coli</i>	17
2.3.2. Imaging flagella confirms correlation between swimming signal and run-tumble	19
2.3.3. Wavelet analysis of the swimming signal	20
2.3.4. Control experiments show trapped <i>E. coli</i> swimming is normal	21
Chapter 3. Long-term, single-cell bacterial motility	24
3.1. Swimming motility at the single cell level	24

3.1.1. Examples of single cell swimming parameters obtained from long time traces ...	24
3.1.2. Run durations in wild-type cells show heavy-tailed exponential distribution.....	25
3.1.3. Heavy-tailed run duration distribution is also seen in a non-nutritious buffer	27
3.1.4. Tumble durations are exponentially distributed	28
3.2. Higher-order features in swimming motility.....	29
3.2.1. Observation of multiple swimming states	29
3.2.2. Reversals in swimming direction	31
3.2.3. Observation of multiple swimming speeds	33
3.2.4. Bias in swimming direction.....	34
Chapter 4. Single-cell chemotactic adaptation.....	35
4.1. Optical trapping enables following adaptation kinetics in individual swimming cells	35
4.1.1. Motivation for studying chemotactic adaptation at the single-cell level.....	35
4.1.2. Combined optical trapping and laminar flow for stimulus application.....	36
4.1.3. Description of single cell chemotactic adaptation.....	38
4.1.4. Population average response reproduces old studies.....	39
4.2. Analysis of chemotactic adaptation at the individual cell level.....	41
4.2.1. Event-based analysis of swimming data.....	41
4.2.2. Abruptness of adaptation as a function of stimulus.....	42
4.2.3. Overshoot response.....	46
4.3. Adaptation kinetics show asymmetry in response to a step up vs. a step down	47
Chapter 5. Theoretical investigation of chemotactic adaptation in <i>E. coli</i>	49
5.1. Review of the <i>E. coli</i> chemotaxis network.....	49
5.2. Ultrasensitive flagellar motor is not the cause of abruptness.....	51
5.3. Role of receptor clustering in stimulus-dependent adaptation abruptness.....	55
5.3.1. Chemoreceptors cluster at the cell poles	55
5.3.2. Chemoreceptor clustering is dynamic	56
5.3.3. Simulating the effect of chemoreceptor clustering on abruptness of adaptation...	56
5.3.4. Fluctuations alone cannot cause abrupt adaptation	59
Chapter 6. Summary and outlook	61
6.1. Studying <i>E. coli</i> chemotaxis using optical traps	61
6.2. Outstanding questions	62
6.3. Receptor expression and its effect on adaptation abruptness.....	62
6.4. Receptor dynamics during the chemotactic response	63

6.5. Cross talk between receptors for different ligands and its effect on the adaptive overshoot	64
Appendix A. Strains, growth media, and trapping media.....	66
A.1. Strains.....	66
A.2. Growth media and conditions.....	66
A.3. Solutions used in trapping experiments	66
A.3.1. Trapping medium.....	66
A.3.2. Trap motility buffer	67
Appendix B. Detailed Description of Experimental Protocols.....	69
B.1. Flagella labeling protocol	69
B.2. 2-D assay protocol.....	69
B.2.1. Construction of the 2-D chamber.....	69
B.2.2. Analysis of the 2-D swimming track data.....	69
References.....	71

Chapter 1. Background

We open this chapter by defining bacterial chemotaxis and discussing its importance to bacteria's survival and fitness. We then introduce chemotaxis of our model organism *E. coli*, with a brief overview of its swimming motility, chemotactic behavior, and the protein network that gives rise to the observed behavior. Lastly, we discuss the reasons for studying chemotaxis at the single-cell level and our motivation for developing a new method optimized for single-cell chemotaxis study. We close this chapter with an overview of subsequent chapters.

1.1. Bacterial chemotaxis and why we study it

The term “bacterial chemotaxis” refers to the directed motion of bacteria in response to chemicals in the environment. Along with growth and division, response to environmental signals constitutes some of the most fundamental tasks that living cells perform. In most cases, cellular response to environment occurs via a process called signal transduction. Signal transduction starts when extracellular stimuli such as chemicals, temperature, and physical tension activate receptor proteins on the cell's surface. The signal then propagates along a chain of biochemical reactions internal to the cell, eventually resulting in behavioral modifications. Responses can manifest in various ways including changes in the gene expression pattern, secretion of molecules, and migration to a different environment.

The model organism *Escherichia coli* (*E. coli*) is known to sense and respond to a wide variety of stimuli, including chemical attractants and repellents, temperature, osmotic pressure, light, and pH (5-9). Over the past half century, chemotaxis of *E. coli* has served as the model system for studying signal transduction (10). *E. coli* cells are easy to cultivate, are amenable to various genetic manipulations, and appear to have relatively simple chemotaxis network compared with most other bacteria and archaea (11). Despite its simplicity, this system is far from being trivial: Chemotaxing *E. coli* cells show high sensitivity through signal amplification (12-14), have a wide dynamic range of response (15), and adapt to various stimulus strengths with high precision (16). By understanding this “hydrogen atom” of signal transduction using quantitative tools, we seek to gain quantitative insights that are applicable to other signal transduction systems in general.

1.2. Importance of chemotaxis to bacteria

1.2.1. Chemotaxis confers dispersal advantages

Due to their small size, bacteria experience their surroundings very differently than macroscopic organisms do. A quantity that captures this experience concisely is the Reynolds number. Reynolds number, defined as $Re = vL\rho/\eta$, quantifies the ratio between the inertial and viscous forces applied upon an object by its medium (17). Here v and L are velocity and size of the moving object, and ρ and η are density and viscosity of the surrounding medium. In water, Reynolds number for a 1 μm -long bacterium swimming at 10 $\mu\text{m}/\text{second}$ is $\sim 10^{-5}$, whereas Reynolds number for a 10 cm-long fish swimming at 1 m/second is $\sim 10^5$. Since for bacteria viscous forces vastly overwhelm inertial forces, gliding motion becomes virtually impossible. In addition, any sense of direction quickly gets lost in rotational diffusion.

Due to the overwhelming presence of diffusion, it is not immediately clear that swimming will bring enough benefits over diffusion to offset the cost of building the swimming machinery. One way of assessing the potential benefits of swimming is by examining the effective diffusion coefficient, D_m , of a motile object and comparing it to the diffusion coefficient of a non-motile object, D_0 (18). D_m is obtained by considering a spherical object of radius r swimming at speed u (measured in units of r), whose swimming direction is randomized by rotational diffusion (17, 18):

$$D_m = \frac{4\pi\eta u^2 r^5}{3k_B T} \quad (1-1)$$

Here, k_B is Boltzmann's constant, T is the absolute temperature, and η is viscosity of the surrounding fluid. Then the ratio D_m/D_0 is:

$$\frac{D_m}{D_0} = \left(\frac{4\pi\eta}{k_B T}\right)^2 \left(\frac{1}{2}\right) u^2 r^6 \quad (1-2)$$

In order for swimming to be worth the effort, this ratio needs to be bigger than one. Otherwise the object could disperse just as effectively by passive diffusion. This condition yields,

$$u > \frac{\sqrt{2}k_B T}{4\pi\eta r^3} \quad (1-3)$$

As the cell gets bigger, the swimming speed (relative to its body size) required for beating diffusion becomes smaller. A spherical cell of 1 μm radius has only to swim half of its body length every second to beat diffusion, whereas a cell ten times smaller has to swim 500 body lengths per second.

Therefore it is reasonable to suspect that a rudimentary form of motility first arose in bacteria that were relatively large in size. Indeed, an analysis of 218 genera of bacteria revealed that 97 genera that were motile are statistically larger in size than 94 genera that were non-motile (27 genera were of mixed motility type) (18). Increased dispersal capacity, even in random directions, would help cells move away from a local environment where food becomes scarcer and toxic byproducts more abundant by the minute. It follows intuitively that the ability to sense chemical cues to bias the dispersal direction would further enhance the cell's chances of proliferation.

1.2.2. Chemotaxis facilitates invasion of host organisms by bacteria

In addition to conferring dispersal advantages, there are evidences suggesting motility's role in facilitating bacteria's invasion of host organisms. In the petri dish, motility was found to be a key factor in irreversible attachment of *Salmonella typhimurium* cells to human cells in early stages of invasion (19). In animal studies, expression of motility genes was found to coincide spatiotemporally with ascension of urinary tract infection by *Escherichia coli* from bladder to kidneys, and a strain carrying a mutation in the motility gene had much reduced ability to ascend to the upper urinary tract (20). *Helicobacter pylori*, the only species of bacteria that is known to colonize the highly acidic mammalian stomach, uses motility to drill through the acidic mucus layer like a corkscrew to reach the epithelial layer where it can cause gastric disorders (21). Non-motile strains of *Helicobacter pylori* showed reduced capability to colonize the stomach (22).

1.3. *E. coli* chemotaxis

1.3.1. *E. coli* as a microscopic swimmer

A typical *E. coli* cell is a 3 μm cylinder with hemispherical end caps 1 μm in diameter. When observed under a microscope, *E. coli* cells are seen to swim in straight segments interrupted by

bursts of reorientation (**Figure 1-1a**) (5). These are called “runs” and “tumbles”, respectively. A great deal is known about how the run-tumble behavior is generated (23-25). A swimming *E. coli* cell possesses 3-5 flagella, with each flagellum consisting of a 10 μm -long helical filament and a bi-directional rotary motor driving the filament rotation (26). When motors rotate counter-clockwise (CCW), filaments coalesce into a coherent bundle due to hydrodynamic interactions. This bundle propels the cell to run at a speed of 10 body lengths per second. Motors switching from CCW to clockwise (CW) rotation exert strain on the filament being driven, which induces a shape transition. Filaments undergoing shape transition break apart from the bundle and cause the cell body to tumble (**Figure 1-1b**) (27).

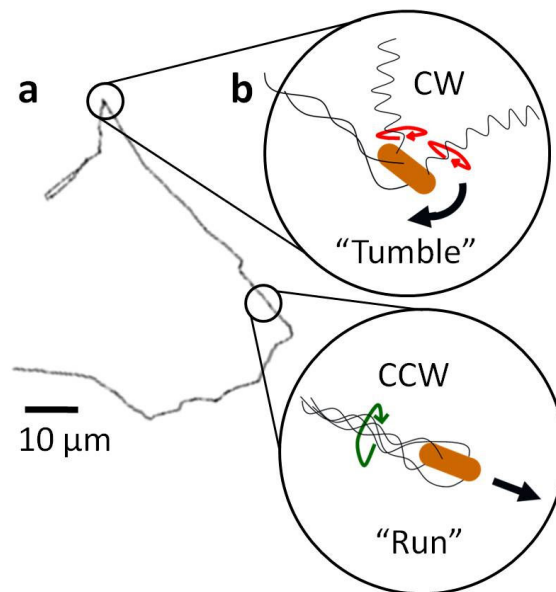


Figure 1-1. The bacterium *E. coli* navigates its environment by switching between runs and tumbles. (a) A microscopic tracking of a swimming cell. Long straight segments correspond to runs and sharp turns to tumbles. (b) Schematic drawing of the tumbling and the running cell. Runs occur when all flagella are rotating counter-clockwise to form a bundle. Tumbles occur when one or more flagella rotate clockwise.

1.3.2. How *E. coli* cells respond to environmental stimuli

In the absence of chemical stimuli, switching between runs and tumbles is commonly assumed to be a random process with a constant switching probability, which leads to exponentially distributed run and tumble durations. On average, runs and tumbles last about 2.5

seconds and 0.5 seconds, respectively (28). As a result, un-stimulated *E. coli* cells search for food in a random-walk manner, with reorientation occurring every few seconds. When the cell senses an increase in chemical attractant, it responds by decreasing the bias of tumbling (**Figure 1-2**) (5). The heuristic reasoning of this response is that the cell lengthens the run if it is moving in the direction of increasing attractant concentration. This leads to chemotactic migration in a biased-random-walk manner.

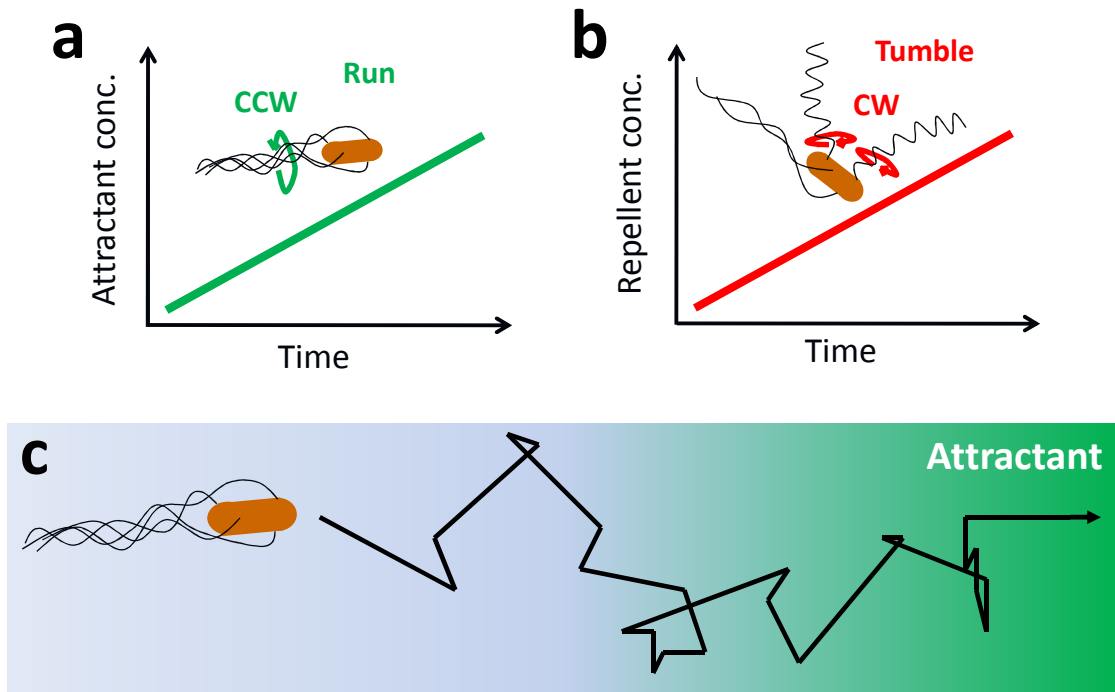


Figure 1-2. *E. coli* cells respond to stimuli by modulating their tumble bias. (a) When the cell senses increasing attractant concentration in time, it decreases its tumble bias. (b) When the cell senses increasing repellent or decreasing attractant concentration, it increases its tumble bias. (c) The resulting swimming pattern resembles biased random walk.

E. coli cells show adaptation to prolonged stimuli (29). If a cell is excited with a step-increase in attractants, it quickly responds (<1 second) by entering a prolonged run, then relaxes (seconds to minutes, depending on stimulus strength) back to the pre-stimulus behavior, getting ready to respond to subsequent stimuli (**Figure 1-3**). This adaptation is exact (29, 30), robust to variations in the chemotaxis protein expression level (31), and serve to increase the dynamic range of *E. coli*'s chemotactic response.

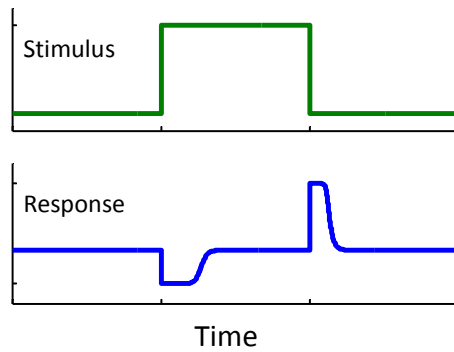


Figure 1-3. Schematic drawings showing *E. coli*'s chemotactic adaptation to step-up and step-down stimuli. Responses are transient and the chemotactic behavior returns to the steady-state when changes in environment persist in time.

1.3.3. *E. coli* chemotaxis network

The network of proteins responsible for *E. coli*'s chemotactic behavior can be divided into three modules (**Figure 1-4**). In the excitation module, receptor proteins located on the cell membrane bind the signaling molecules on the outside, and affect the activity of the kinase protein CheA (a protein that adds a phosphate group to another protein) on the inside. The signal then gets relayed to the flagellar motor behavior in the response module, with the protein CheY acting as a messenger protein. CheY is active in its phosphorylated form, CheY-P, and binds the flagellar motor to biases the motor's rotation to CW direction (32, 33). As mentioned above, CW rotation leads to tumbling behavior (34). Binding of attractant to the receptor deactivates CheA, leading to less tumbling behavior. As the cell responds to the chemical stimuli, it also adapts to them. This is done by an antagonistic pair of proteins CheR and CheB in the adaptation module. CheR and CheB adds and takes off a methyl group from the receptor protein, which activate and deactivate it, respectively. This equips the cell with the ability to internally adjust the activity of CheA, independent of the external stimuli. Adaptation by CheR and CheB is a slower process that takes from a few seconds to minutes depending on the stimulus strength (16).

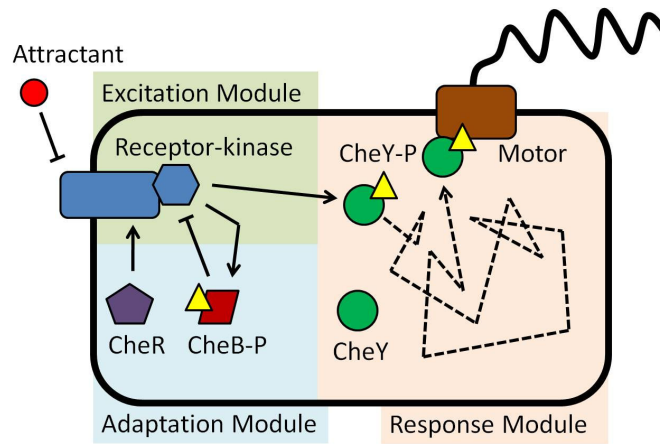


Figure 1-4. The three modules of the *E. coli* chemotaxis network. Solid arrows indicate activating interactions, and the solid lines ending with a bar indicate de-activating interactions. Dashed lines depict diffusion of CheY-P molecules.

1.4. Studying chemotaxis at the single-cell level

1.4.1. Individuality in bacteria provides motivation for single cell studies

While microbiology experiments are often conducted by growing a genetically identical culture of bacteria derived from a single cell, one finds a surprising degree of heterogeneity under the microscope (35, 36). Heterogeneity can arise from random genetic mutations or epigenetic mechanisms such as DNA methylation. Such processes change the properties of the population as a whole in successive generations. Examples include evolution of antibiotic resistance and differentiation of stem cells into specialized tissue cells (37, 38).

Heterogeneity can also arise in a non-genetic, non-heritable way. In these cases the properties of the population remain the same in successive generations. Examples include antibiotic persistence, where a small fraction of a susceptible population can withstand the antibiotic pressure to give rise to equal fractions of both susceptible and resistant population upon removal of antibiotic pressure (39, 40); bistable gene expression, where sub-saturating induction of a gene leads to all-or-none expression in individual cells (41, 42); and chemotactic adaptation, where individuals in an isogenic population exhibit widely distributed adaptation times in response to an identical stimulus (30, 43). Such non-genetic heterogeneity is commonly thought to occur due to the stochastic noise in the biochemical reactions involving low number of molecules (44, 45).

1.4.2. Individual *E. coli* cells show long-term fluctuations in chemotactic behavior

Noise can not only give rise to population heterogeneity, but also to behavioral fluctuations in a single cell. In a study where the switching behavior of individual flagellar motor was observed for very long time periods (hours), the CW rotation bias of a given motor was found to have long-term fluctuations on the order of minutes, and dwell time distribution of the CCW rotation state exhibited a heavy tail (46). Previous studies (5, 13, 16, 47) had not observed these fluctuations because in these studies, responses of many cells or repeated responses of individual cells were averaged together. The long-term fluctuations of the motor switching behavior are believed to arise from fluctuations in the CheA activity (46, 48, 49), although direct evidence showing the existence and the extent of CheA activity fluctuations in individual cells is lacking. A corollary of this result was that extension of such behavior to the whole-cell swimming level would have implications for *E. coli*'s foraging strategy (50), especially in environments where sources of food are few and far between and highly variable in intensity (51). However, existence of such behavior at the swimming cell level could not be predicted a priori, since the mapping from single flagellum behavior to the swimming behavior of a multi-flagellated cell is complex and poorly understood (3, 4).

1.4.3. A new technique is needed to study chemotaxis at the single-cell level

Standard methods for assaying bacterial chemotaxis at the single-cell level typically fall into two categories: The first consists of observing freely swimming cells, typically in a micro-fluidic chamber setup. Chemoeffector variation is then created in space or in time, e.g. by fluid flow (52), by an enzymatic reaction (53), by UV-light-activated release of caged-molecules (54-56), or by using an iontophoretic micropipette (57). Cellular response, in terms of change in swimming behavior – e.g. frequency of tumbles – is then examined, sometimes with the aid of computerized cell recognition and motion tracking (58-60). The second type of assay uses cells that are tethered to a surface – usually a microscope slide – so that the rotation of flagellar motors can be followed, either because the motion results in the cell itself rotating (61), or by using a fluorescent bead to follow the resulting flagellar rotation (62).

The approaches above have enabled the acquisition of large amounts of data that yielded important insights into the mechanism of bacterial chemotaxis. However, both assays suffer from significant limitations. The free swimming assay typically yields very noisy data, limited to

relatively short time periods (53, 60, 63). When three-dimensional motion is followed, sophisticated custom-made optics need to be used to allow tracking the cells as they move out of the optical focus. The acquired trajectories are limited to ~30 seconds (53, 63), not enough to characterize such features as inter-event statistics and adaptation times. When bacterial swimming is limited to two dimensions (2D), longer trajectories can be acquired (several minutes (34)). Still, data acquisition is limited by multiple factors. Rotational Brownian motion (though a relevant factor in bacterial motion and perception of chemicals) limits the ability to classify “runs” and “tumbles” (64). Interaction with the surface may also become a hindering factor in such assays (65, 66). Lastly, the fact that the cells actually swim – thereby changing their position – makes it impossible to impose a particular stimulus (e.g. a constant gradient of attractant) on each cell throughout the experiment.

As for the tethered-cell assay, one of the main limitations is that this assay examines the activity of a single motor, rather than the physiologically relevant whole-cell swimming phenotype. A typical cell has 3-5 flagella (4), each driven by its own motor. These motors exhibit asynchronous activity with regards to their direction of rotation (67, 68), and the resulting cell’s swimming behavior is a complex outcome of the multi-motor state. Tethered-cell assays are also notorious for their low efficiency; typically multiple tethered cells are tracked under the microscope, with only a few exhibiting the “proper” phenotype.

1.5. Scope of this thesis

The goal of this thesis is to investigate the swimming motility and chemotactic response of *E. coli* at the single-cell level. The specific aims of this work were to:

1. Develop an optical trap-based motility assay for long-term, high-resolution characterization of swimming motility in individual *E. coli* cells.
2. Analyze long-term swimming statistics of individual *E. coli* to look for evidence of behavioral fluctuations and higher-order features not observed in population average studies.
3. Characterize chemotactic adaptation of *E. coli* at the individual cell level, and observe the dependence of various behavioral features of adaptation on stimulus strength.

In chapter 2, we develop a novel experimental method where individual *E. coli* cells are pinned down in space by optical traps and their swimming behavior measured over long-time periods. We discuss the photo-induced damage due to infrared trapping laser and optimal trapping conditions, and describe the motion exhibited by trapped swimming cell. We also discuss how the swimming signals are converted to binary run-tumble traces and verify that optically trapped cells exhibit normal swimming behavior.

In chapter 3, we examine the statistics of single cell motility parameters, and show that swimming cells exhibit heavy-tailed run duration distributions in the way analogous to the CCW duration distributions of single flagella. We also describe high-order swimming features observed at the single-cell level such as reversal of swimming direction and multiple swimming speeds.

In chapter 4, we describe our custom laminar flow chamber setup used to apply chemical stimuli to optically trapped *E. coli* cells, and the resulting chemotactic adaptation at the single-cell level. We characterize individual cells' response in terms of two behavioral features of chemotactic adaptation and examine their dependence on applied stimulus strength. We also describe the asymmetry between responses to positive and negative stimuli.

In chapter 5, we describe the existing mathematical model of *E. coli* chemotaxis and examine aspects of the model that can explain the observed trends in the adaptation behavior. Future directions are discussed in chapter 6.

Chapter 2. Measurement of bacterial motility using optical tweezers¹

This chapter describes our novel experimental technique that uses optical traps to measure bacterial motility. We start with a brief introduction to optical trapping, discussing the physical principles, modes of application in biology, and the issues of optical damage and heating. We then describe our specific method: the instrument design, buffer conditions, sample chamber, and the experimental procedure. Features of the swimming signal observed from trapped bacteria are described, as well as the automated data analysis routine used to distinguish runs from tumbles in the swimming signal. Control experiments are discussed to demonstrate that trapped *E. coli* cells exhibit normal swimming behavior.

2.1. Introduction to optical trapping in biology

2.1.1. Physical principles of optical trapping

Optical traps are formed by tightly focusing a Gaussian-profile laser beam using a high-numerical aperture microscope objective. A dielectric object in the beam path near the focus experiences two types of forces, the scattering force and the gradient force. Scattering force simply pushes the object in the direction of the beam. The gradient force, on the other hand, attracts the electric dipole induced in the object toward the laser focus, where the electric field intensity is highest. A stable trap in three dimensions is formed slightly downstream of the beam focus where the gradient force balances out the scattering force (69). In the linear force regime, optical traps behave like three-dimensional Hookean springs (70).

2.1.2. Application of optical traps in biology

Optical traps have found widespread use in biology. In particular, optical traps have been used to measure forces and displacements from single proteins, shedding light on detailed mechanistic properties of a biologically important class of molecules. In single molecule studies, DNA or proteins of interest are typically attached to polystyrene beads that optical traps can easily manipulate and use as “handles”. Use of spherical bead handles allows a relatively straight-forward calibration scheme to yield the spring constant, or “stiffness”, of the optical trap (71). When coupled with an extremely sensitive detection method for measuring the bead

¹ Chapter 2 was adapted from a published work:
Min TL, Mears PJ, Chubiz L, Rao CV, Golding I, Chemla YR, (2009) “High-resolution, long-term characterization of bacterial motility using optical tweezers.” *Nature Methods* 6(11):831-835.

displacement (72), optical traps enable precision measurements on the scale of pico-Newtons and nano-meters (70, 73). Using this general strategy, optical traps have elucidated fundamental biochemical processes such as duplex DNA unwinding (74), viral DNA packaging (75, 76), transcription and translation (77, 78) at the level of single proteins. Mechanical properties of DNA have also been extensively studied using optical traps (79).

Optical traps have also been used to study living cells. Optically trapped polystyrene beads were utilized in various ways to study cell membrane tension and shear modulus (80, 81), as well as mobility of membrane-bound proteins (82, 83). Trapped beads have also been used to stimulate cells either by making a direct contact (84) or manipulating the concentration of chemicals in the local environment (85). Yet other studies have used optical traps to directly trap and manipulate cellular organelles such as chromosomes (86), mitochondria (87), and even whole yeast cells (88). In such studies, optical traps were primarily used as a manipulation tool rather than as a quantitative measurement tool.

2.1.3. Photo-induced damage and heating

Since their very first biological applications, optical traps have been known to cause photo-induced damage to the trapped specimen (69, 89). This is not surprising when one considers the high level of light intensity at the focus of the laser beam. The intensity of a 100-mW laser beam at the diffraction-limited focus is about 10^{11} W/m², or 10^8 times that of sunlight at the surface of the earth.

While optical traps can be formed using light of any wavelength in the visible and near-visible range, some wavelengths are preferable to others due to damage considerations. Ultraviolet light is known to cause DNA damage (90) and visible light may induce unwanted physiological response or auto-fluorescence excitation (8, 91). Near-infrared light also causes damage via generation of reactive oxygen species in the surrounding medium, although it is preferable to ultraviolet and visible wavelengths due to its relative transparency to biological samples (92).

Damage caused by near-infrared light due to generation of reactive oxygen species was observed to be minimal around 830 and 970 nm (93, 94), and was significantly reduced when oxygen was removed from the surrounding medium (93, 95). Although 1064 nm lasers are about

twice as damaging as 830 and 970 nm lasers in the presence of oxygen (93, 94), this difference becomes negligible when oxygen is removed (data not shown). 1064 nm lasers are commonly used in optical trap instruments (including our work) due to the commercial availability of high-power, high-quality 1064 nm lasers.

Heating caused by the trapping light, while a frequent source of concern (96, 97), is generally not a big issue when moderate laser intensities are used. For 1064 nm lasers, temperature increase due to absorption of the trapping light was reported to be around 1 C° per 100 mW of laser power at the sample plane (96-98). 980 nm laser can cause 3.5 times more heating than 1064 nm (99).

2.2. Description of the optical trapping method

2.2.1. Optical trap instrument design

Figure 2-1 shows a simplified layout of the instrument used in this work. We used a single-beam 5-W, 1,064-nm diode-pumped solid-state laser (BL-106C; Spectra-Physics). The beam diameter coming out of the laser head was about 1 mm, and we expanded the beam using a set of two afocal lenses (T1) for the ease of alignment. The beam was then separated into two paths using a polarizing beam splitter (BS1). One path was reflected by a mirror mounted on a piezo-actuated stage (Nano-MTA; Mad City Labs), which controls the separation between the two beams, and eventually the two optical traps formed at the sample plane. The two beam paths were co-aligned using a second polarizing beam splitter (BS2) and expanded once more (T2) before they reached the front objective (O1). The final diameter of the beams reaching the front objective were 8 mm, just enough to slightly over-fill the back aperture of the objective. The front objective was a water-immersion objective with numerical aperture of 1.2, and it tightly focused the two incoming beams to diffraction-limited spots. The objective's transmission efficiency for the 1,064-nm light was about 50%. The transmitted light was collected and collimated by a second, identical back objective (O2), and mapped to quadrant photo-diodes (QPD) for position measurement of the trapped object.

The sample chamber was positioned between the two objectives and could be displaced relative to the two traps in three dimensions by a motorized translational stage (ESP300; Newport). For bright field imaging, a white light from a light-emitting diode (LED) was aligned for Khoeler

illumination geometry. The front objective (O1) in this case served the function of a condenser in a conventional light microscope, and the back objective (O2) collected the transmitted light and sent it to the charge-coupled device (CCD) camera (Watec). For fluorescence imaging, 532 nm laser from a 30-mW source (World Star Tech) was aligned for epi-fluorescence excitation geometry. Emitted fluorescence was directed to an electron-multiplying charge-coupled device (EMCCD) camera (Princeton Instruments).

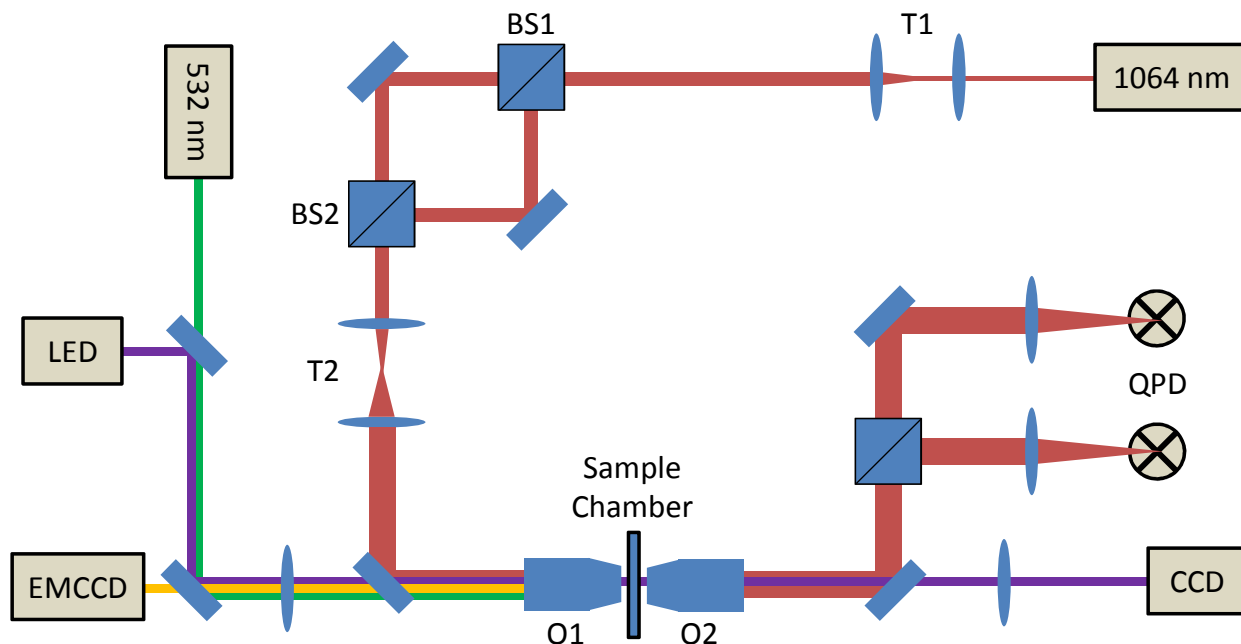


Figure 2-1. Layout of the instrument used throughout this work. (Abbreviations) T1&2: Telescope 1&2, BS1&2: polarizing beam splitter 1&2, O1&2: Objective 1&2, LED: light-emitting diode, EMCCD: electron-multiplying charge-coupled device, CCD: charge-coupled device, QPD: quadrant photo diode. Various colored lines show the light pathways from different sources. Red: 1064 nm laser, Green: 532 nm laser, Purple: LED, Yellow: fluorescence emission from the sample.

2.2.2. Trapping medium

Of primary importance to our work was characterizing the health of the optically-trapped cells. We found that ~ 100 mW of laser power at the sample plane was needed to stably trap swimming cells (see below). With such laser power, cells trapped in oxygenated growth medium (Tryptone Broth) exhibited rapid deterioration in health, with their motility coming to a complete halt within tens of seconds (data not shown).

To combat this problem, we removed oxygen from the trapping medium (93). This was done by adding the oxygen-scavenging enzyme glucose oxidase. As its name suggests, glucose oxidase oxidizes glucose by consuming molecular oxygen dissolved in liquid medium. One of the byproducts of this reaction, hydrogen peroxide, was removed by adding another enzyme, catalase. The other byproduct, gluconic acid, was buffered by adding Tris buffer to the medium. Under this “trapping medium” (Tryptone Broth supplemented with 100 mM Tris-Cl (pH 7.5), 2% (wt/vol) glucose and oxygen scavenging enzymes), we found that trapped *E. coli* cells displayed healthy behavior. Furthermore, *E. coli* cells trapped in the trapping medium displayed growth, elongating and dividing at a rate comparable to standard values from the literature (~2 hour doubling time at room temperature (100)) (**Figure 2-2**).

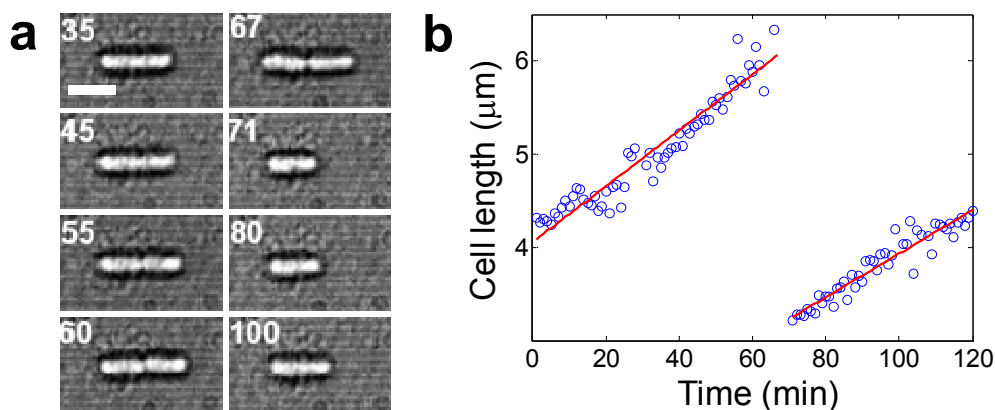


Figure 2-2. Optically trapped cell grows and divides. (a) Brightfield images showing an *E. coli* cell continuously trapped in a nutrient-rich medium. The cell divides ~ 70 minutes into observation. Following division, growth of the trapped daughter cell continues. Numbers are in minutes. Scale bar: 2 μm. **(b)** Length of the cell in panel **a** measured from brightfield images taken at 1-minute intervals. Red lines are linear fits.

We also found Tryptone Broth to be unnecessary for maintaining healthy motility, although growth was halted in its absence. In case where presence of amino acids in the Tryptone Broth needed to be avoided, we used “trap motility buffer” (100 mM Tris-Cl (pH 7.5), 70 mM NaCl, 2% (wt/vol) glucose and oxygen scavenging enzymes) instead. Our trapping protocol constitutes a significant improvement over a previously reported trap-based study of bacterial swimming under oxygenated conditions (101), where cells could be monitored only for very short times (<

10 s). See *Appendix A.3.* for detailed protocols for making trapping medium and trap motility buffer.

2.2.3. Trapping chamber

Glass coverslips (Fisher, number 1) were sonicated in dry acetone for 5 min and rinsed with deionized water. Flow channel patterns were cut out from Nescofilm (Karlan) and placed in between two coverslips, one of which had custom-drilled holes (0.05-inch diameter) for inlets and outlets. A short piece of glass capillary (100 μm outer diameter) was positioned near the experimental region as a spacer and a point of reference. The Nescofilm flow channel pattern was bonded to coverslips by melting on a hot plate for 4 min. The completed flow cell was inserted into a custom metal frame where inlet and outlet tubing were screwed on for a tight seal (*Figure 2-3*).

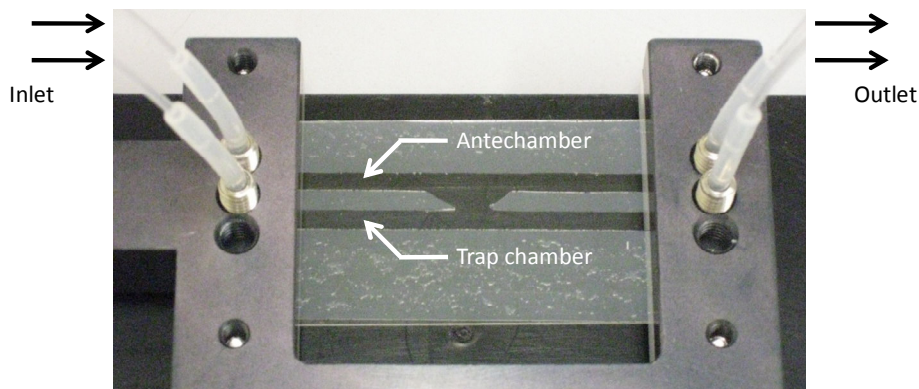


Figure 2-3. Trapping chamber. The antechamber holds trapping medium containing cells. After a cell is trapped, it is moved to the trap chamber, which contains trapping medium but no additional cells. Channel cross-section dimensions are 100 μm x 4000 μm .

2.2.4. Experimental procedure

E. coli cells suspended in trapping medium at a low density ($\text{OD}_{600} = \sim 0.01$, or 10^{-5} cells per $1 \mu\text{m}^3$) were injected into the top ‘antechamber’, and flowed through an opening into the bottom channel containing blank trapping medium. Cells were initially trapped by a single beam along the beam axis, and the second beam was repeatedly brought near the first and pulled away until the two ends of the rod-shaped cell were held by each trap. The separation between the two traps was adjusted until it appeared roughly equal to the cell length. We used 50 mW of trapping

power at the sample plane in each trap, sufficient to stably trap and manipulate the cells yet low enough to minimize photodamage.

Before data acquisition, the trapped cell was moved sufficiently far away from the connecting region between the top and the bottom channels to prevent possible interruptions by other cells in the flow cell. In addition, the use of water-immersion objectives to form our traps allowed us to position cells far from the sample chamber surfaces (50 μm), minimizing potential cell-surface interactions.

2.3. Swimming signal measurement and data analysis

2.3.1. Swimming signal observed from trapped *E. coli*

Despite immobilization by the optical traps, cells displayed motile behavior, evinced by flagellar bundle rotation and counter-rotation (“rolling”) of the cell body (102). This behavior was detected directly and sensitively by the optical traps themselves, by imaging light from both orthogonally polarized trapping beams onto two separate quadrant photo-diodes (QPD). Consistent with previous reports on optically-trapped cells (101, 102), power spectra from the QPD outputs upon trapping of a swimming cell revealed two peaks with frequencies $\omega \sim 100$ and $\Omega \sim 10$ Hz (**Figure 2-4a**). These oscillatory signals correspond to flagellar bundle rotation and cell body counter-rotation or “roll” (101, 102), respectively (**Figure 2-4b**). Our measured flagellar rotation (ω) and body-roll rates (Ω) are consistent with those observed in experiments with freely swimming cells (3), demonstrating that the optical traps did not inhibit motility other than in fixing the cell’s position.

Although cell swimming was not observed directly, the flagellar rotation rate ω and body roll frequency Ω shed light on the swimming mechanics of the cell. Loosely speaking, ω determines the propulsive force and torque generated by the flagellar bundle (both also depend on parameters such as the number, spatial arrangement, and geometry of the flagella: length, helical pitch, etc. (101)). The swimming speed v and body roll Ω are determined by the balance between the propulsive force and torque and the viscous linear and rotational drag of the cell body, respectively (101). Importantly, it follows that any variation in rate or conformational state of the flagellar bundle will likely be manifested in changes in both v and Ω .

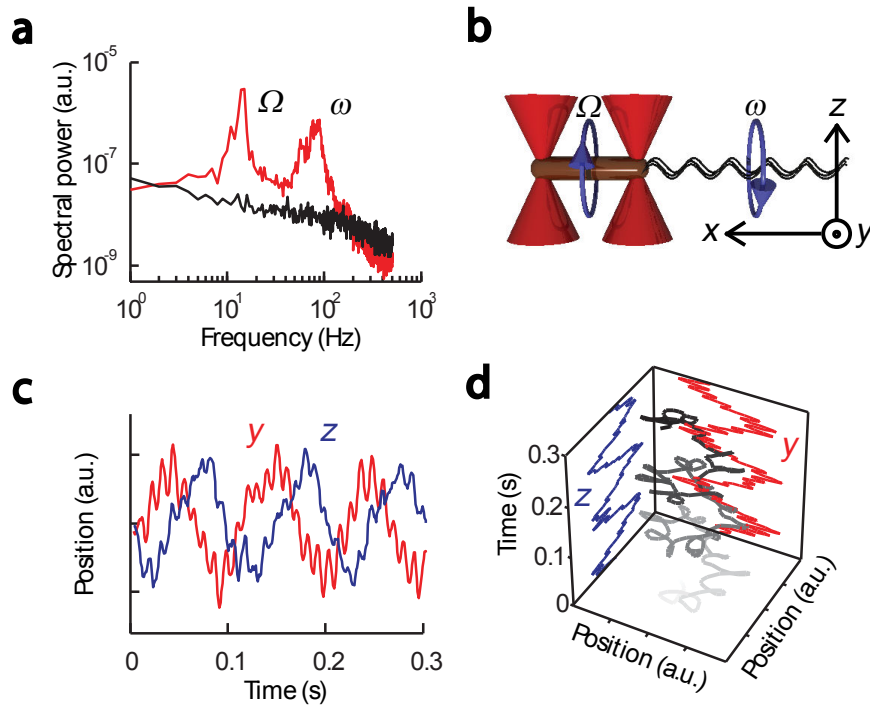


Figure 2-4. Optical traps detect cell motility. (a) Power spectra of the optical trap signal from a swimming cell (red) and a nonmotile cell (red). Swimming cell signal shows oscillatory peaks at 10 Hz and 100 Hz corresponding to body roll (Ω) and flagellar bundle rotation (ω) frequencies, respectively. (b) Schematic optical traps (red cones) and a trapped cell. Circular arrows indicate the rotational direction of the cell body (brown cylinder) and the flagellar bundle (black wavy lines). Also shown is the coordinate axis notation for the optical trap signal. (c) Typical optical trap signal of a swimming cell along y and z directions. (d) A three-dimensional plot (grayscale line) of the swimming cell signal. Color darkens with time. Rotational motion of the cell body (large radius rotations) and the flagellar bundle (small radius rotations) are easily recognizable.

Figure 2-4c displays a short time trace of a trapped, swimming *E. coli* cell (strain RP437, wild-type for chemotaxis (103)). The cell was trapped horizontally (a direction we define as x , *Figure 2-4b*). The motion of each trapped end in the orthogonal plane, along the vertical direction (y) and along the optical axis (z), was detected by one QPD and displayed in the red and blue time traces, respectively, revealing both frequencies of oscillation. The y and z components of the low-frequency signal are 90° out of phase, indicating that the cell end moved in a circular trajectory perpendicular to its body axis (*Figure 2-4d*). The rotation is clockwise (CW, as measured looking at the tail of the cell in the direction of swimming), consistent with

the expected direction of body roll (104). The higher-frequency oscillatory signal corresponding to flagellar bundle rotation also reveals a circular motion, in the counterclockwise (CCW) direction, as expected (*Figure 2-4d*).

2.3.2. Imaging flagella confirms correlation between swimming signal and run-tumble

Closer examination of swimming traces revealed regions of alternating oscillatory and non-oscillatory (“erratic”) signals (compare 1-1.5 s and 1.5-2 s regions in *Figure 2-5b*; only the low-frequency component corresponding to body roll is shown for clarity). By imaging the motion of a Cy3-labeled cell using epifluorescence microscopy and simultaneously monitoring the trap signals generated by this motion, we established that these oscillatory and erratic signals correspond to runs and tumbles of the cell, respectively (see *Appendix B.1* for the labeling protocol). As shown in *Figure 2-5a*, cell images taken during oscillatory periods (1.2 s, 2.2 s, 2.7 s, 3.2 s) display a well-formed flagellar bundle extending from the tail of the cell as expected for a run, whereas those taken during erratic periods (1.7 s) exhibit a disrupted bundle, indicative of a tumbling conformation (4).

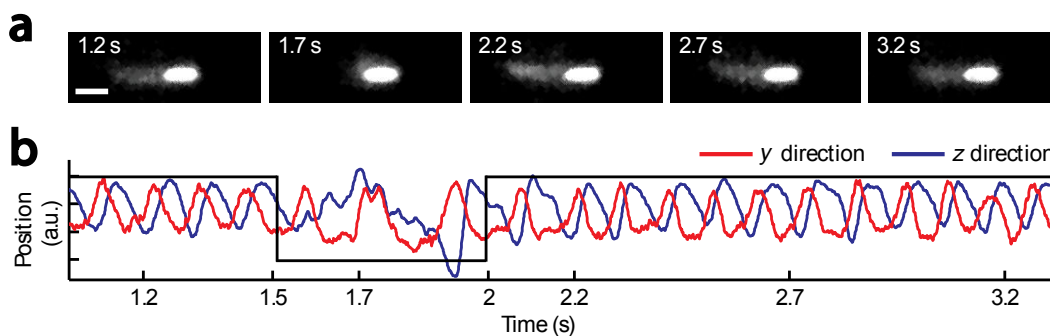


Figure 2-5. Direct observation of tumbles in an optically trapped cell. (a) Fluorescence images of a trapped cell. Shown in the first frame is the trapped cell body (bright oval shape) and the flagellar bundle (faint cloud) formed to the left of the cell body. The second frame shows the cell tumbling, with the appearance of a disrupted flagellar bundle. Subsequent frames show the reformed flagellar bundle and the running cell. Each frame was obtained by averaging three successive images collected at a rate of 10 Hz, with the marked time point in the middle. Scale bar, 2 μm . (b) Optical trap signals in the y and z directions, recorded simultaneously with the fluorescence images. Black lines delineate the run (high) and tumble (low) periods. Only the low-frequency component corresponding to body roll (Ω) is shown for clarity.

2.3.3. Wavelet analysis of the swimming signal

To quantify the long-term swimming behavior of optically-trapped cells, we developed an automated run-tumble detection routine using the continuous wavelet transform (105) to discriminate regions of oscillatory and non-oscillatory behavior.

All routines for analyzing optical trap data were written in Matlab (Mathworks). Raw data obtained at 1,000 Hz sampling frequency were low-pass– filtered to 100 Hz, and the amplitude was normalized in nonoverlapping 1-s windows. Two separate sets of y and z signals obtained from the two ends of the cell body were combined by taking the difference for enhancement in signal-to-noise ratio (73). Motion of the cell in the x direction was also detected by the position-sensitive photodetector but was more inconsistent. We believe this is because the cell trajectory was predominantly in the orthogonal y – z plane. Thus, signals along the x direction were not used in our analysis.

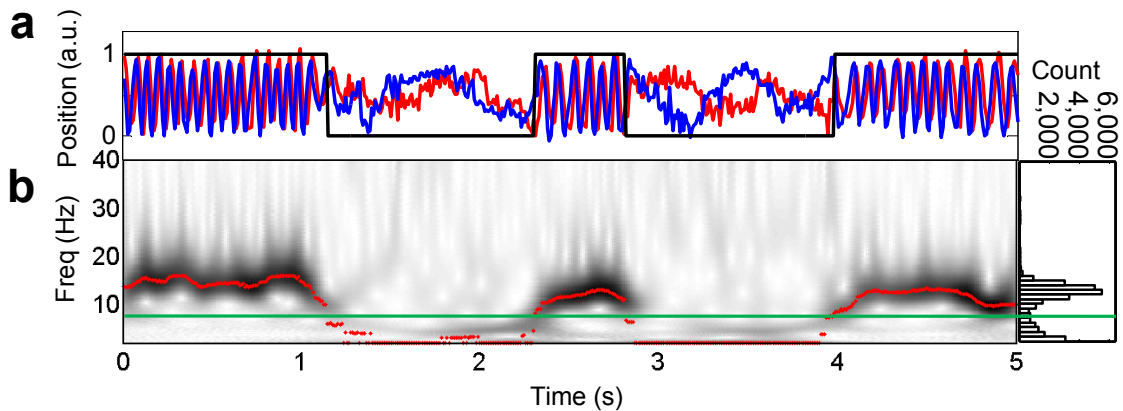


Figure 2-6. Run-tumble analysis of optical trap data. (a) Swimming signal in y (red) and z (blue) directions from an optically trapped cell, and the binary signal (black) indicating regions of runs (1) and tumbles (0). **(b)** Continuous wavelet transform of the y signal in the frequency range of 2 – 40 Hz. Red dots indicate the peak frequency component at each time point. Shown on the right is the histogram of peak frequencies from the entire time trace. The frequency value at the local minimum of the histogram is chosen as the threshold (green line), which is used to distinguish runs from tumbles.

Using the y and z signals, the peak frequency component (Ω) at each time point was obtained from a continuous wavelet transform. This method is preferable to a Fourier transform over a running time window. Whereas the Fourier transform is limited by the tradeoff between temporal

and spectral resolution for a given window size (a larger time window results in high frequency resolution but low time resolution and vice versa), the continuous wavelet transform does not require a characteristic window size. Instead, this transform makes use of a ‘mother wavelet’ that can be scaled and shifted to find the best match for the data trace at each time point. The scale can then be converted to a corresponding frequency. Our wavelet analysis was performed using the complex Morlet mother wavelet in a linearly scaled frequency range of 2–40 Hz (105).

A typical result is shown in **Figure 2-6a**. Runs and tumbles were distinguished by applying a single threshold value to the Ω time trace. The threshold was determined by examining the distribution of Ω and finding the local minimum between peaks corresponding to run and tumble (**Figure 2-6b**). For cases in which a clear local minimum could not be found, an arbitrary threshold of 4 Hz was applied. Detected runs and tumbles that were shorter than 100 ms were removed, as our detection limit was expected to be one cycle in the sinusoidal pattern of the running cell (10 Hz body-roll frequency is taken as an arbitrary standard). We obtained two separate binary traces from the signals in y and z directions from each cell. The same threshold value was used for both y and z directions, and the two resulting binary traces were combined using an ‘and’ gate to produce a single binary trace for the cell.

2.3.4. Control experiments show trapped *E. coli* swimming is normal

To ascertain that the observed run-tumble behavior in trapped cells is physiologically relevant and rule out the possibility of an artifact induced by the optical traps, we performed two control experiments. In the first, we examined the motility of two mutant strains (**Figure 2-7abc**): a *cheY* deletion (strain CR20; see **Appendix A.1.** for list of strains used in this study), which does not tumble, and a *cheZ* deletion (strain CR33), which mostly tumbles and does not run. As shown in **Figure 2-7d**, data traces obtained from these mutants display the expected phenotypes: “runners” generate prolonged oscillatory signals, whereas “tumblers” undergo continuous erratic motion.

In the second control experiment, we quantified the run-tumble behavior of strain PS2001-pMS164 (34), in which a permanently active CheYD13K mutant protein is expressed from an inducible promoter, under the control of isopropyl β -D-1-thiogalactopyranoside (IPTG) (**Figure 2-7e**). This strain allowed us to modulate run-tumble statistics and to compare them to those

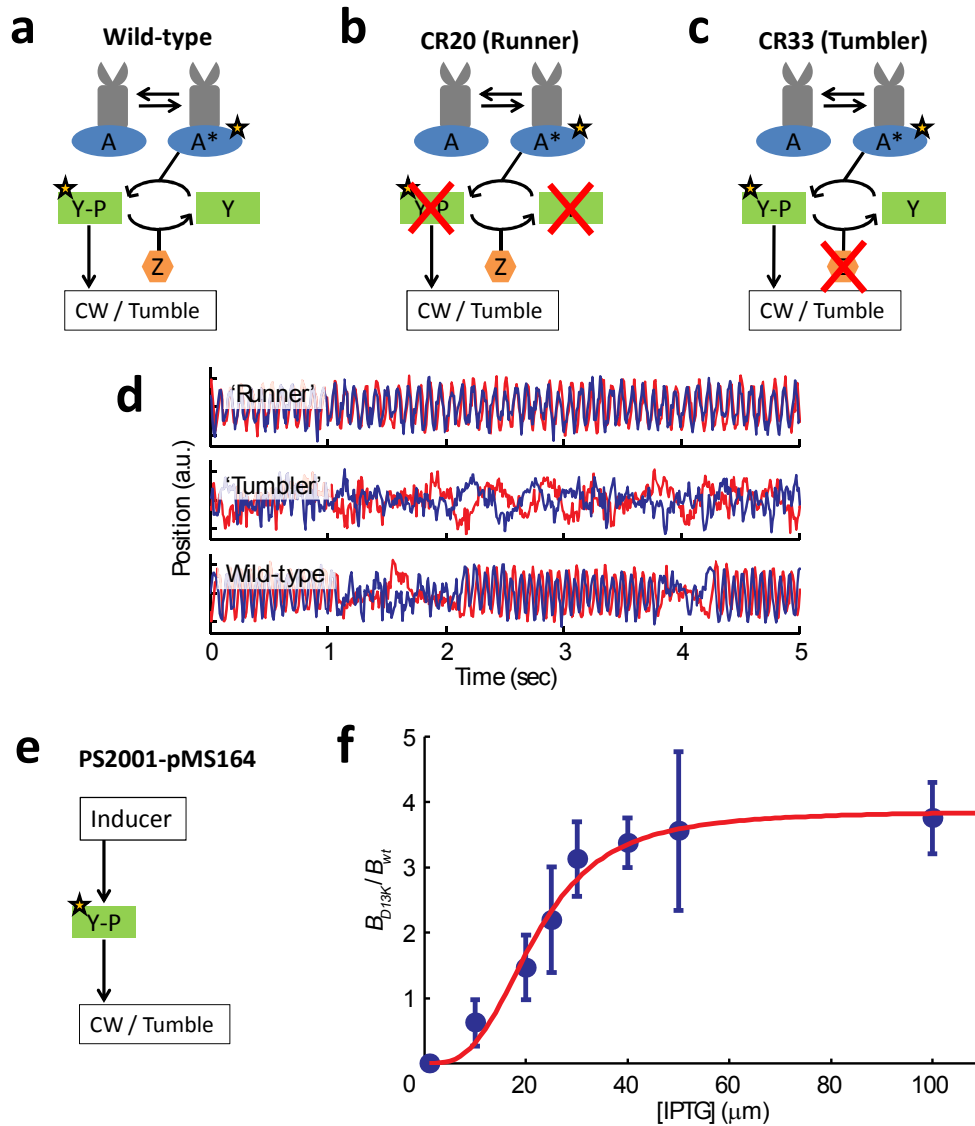


Figure 2-7. Run-tumble phenotyping using the optical trapping assay. (a) Wild-type *E. coli* chemotaxis network. **(b)** A ‘runner’ mutant lacks CheY. **(c)** A ‘tumbler’ mutant lacks CheZ. **(d)** Optical trap signals characteristic of each strain’s behavior. Runner strain generates predominantly oscillatory signals. Tumbler strain generates predominantly erratic signals. Wild-type generates oscillatory signals interrupted by intermittent erratic signals. **(e)** An inducible mutant where the amount of CheY-P can be controlled externally. **(f)** Induction response (average tumble bias B_{D13K} of individually trapped cells at various levels of induction, normalized by the average tumble bias of the wild-type cells B_{wt}) of the inducible strain. Higher CheY_{D13K} levels increase the probability of tumbling. Errorbars are standard errors of mean. (n = 6, 8, 8, 5, 13, 4, 3, 6, from lowest to highest [IPTG]. Fitting to Hill function gives a Hill coefficient of ~ 3 (red line).

obtained with our wild-type strain. Analysis of 53 PS2001-pMS164 mutant cells at various induction levels revealed that, as expected, run durations are longer than in wild-type cells at low (1 μM) IPTG concentrations and shorter at high (100 μM) IPTG concentrations. As shown in **Figure 2-7f**, the tumble bias B — defined as the fraction of time the cell spends tumbling, $B = t_{\text{tum}}/(t_{\text{tum}}+t_{\text{run}})$ — exhibits a sigmoidal response to [IPTG]. The midpoint of the response is at ~ 20 μM and the enhancement in bias relative to wild-type cells is a factor of ~ 4 . This behavior is in good agreement with the literature (34), further confirming our view that tumbles exhibited by trapped *E. coli* represent physiologically relevant events.

Chapter 3. Long-term, single-cell bacterial motility²

In this chapter, we examine various properties of *E. coli* swimming motility at the individual cell level. This is made possible by monitoring the swimming behavior of individual cells over a long time period in a steady environment. In the wild-type cells, run durations are found to exhibit a heavy-tailed distribution, a feature which is absent in the PS2001-pMS164 strain (see *Appendix A.1.* for a description of strains). In light of similar results previously seen in individual flagellar (2), our results from swimming cells suggest that fluctuations in CheA activity gets propagated through the flagellar motor to the level of swimming behavior in wild-type cells. Active metabolism is ruled out as a source of CheA fluctuations. Tumble durations are exponentially distributed regardless of the strain. We also describe high-order swimming features observed at the single cell level, such as changes in swimming speed and orientation.

3.1. Swimming motility at the single cell level

3.1.1. Examples of single cell swimming parameters obtained from long time traces

Using the optical trapping assay and the data analysis routine described in chapter 2, we

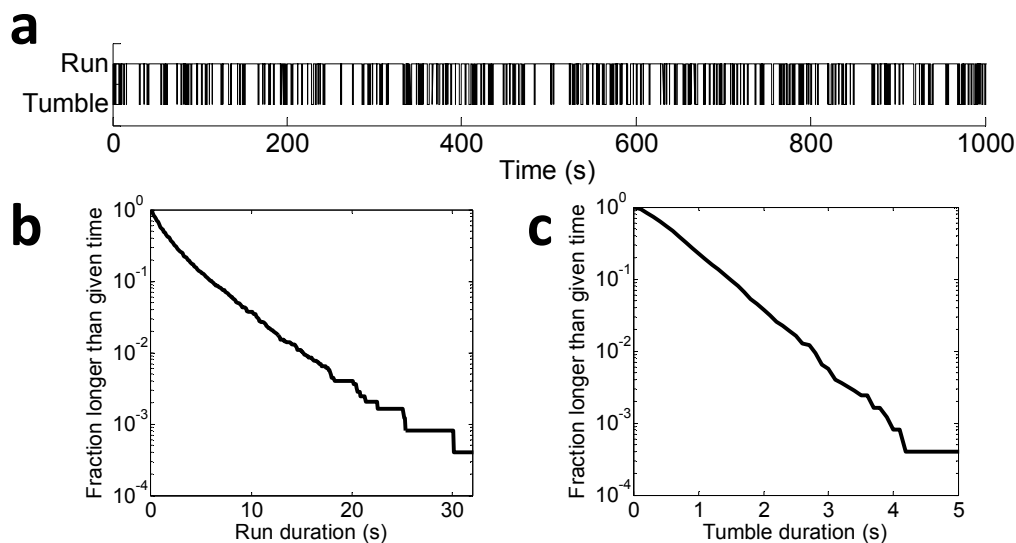


Figure 3-1. Single cell statistics obtained from long measurements. (a) A typical binary time series generated from the swimming signal of a single trapped cell. (b,c) Cumulative distributions of run (b) and tumble (c) durations comprising 2,474 runs and tumbles observed from a single wild-type *E. coli* cell.

² Chapter 2 was adapted from a published work:

Min TL, Mears PJ, Chubiz L, Rao CV, Golding I, Chemla YR, (2009) “High-resolution, long-term characterization of bacterial motility using optical tweezers.” *Nature Methods* 6(11):831-835.

obtained and analyzed long (up to 2 hours) swimming traces from individual cells. *Figure 3-1a* shows part of a run-tumble binary trace from a single cell. Such traces contain numerous switching events between runs and tumbles, and provide a statistically meaningful description of the swimming behavior of individual cells. For example, the cumulative distributions of run and tumble durations constructed from over 2000 events shown in *Figures 3-1b,c* can provide detailed insights into the swimming behavior happening at the single cell level (2, 106).

We also examined the distribution of swimming parameters in populations of cells. *Figure 3-2* shows the distribution of the steady-state tumble bias from 186 individual cells of the same strain measured for about 5 minutes each. The distribution reveals the presence of varying levels of steady-state swimming behavior within the genetically identical population of cells (43).

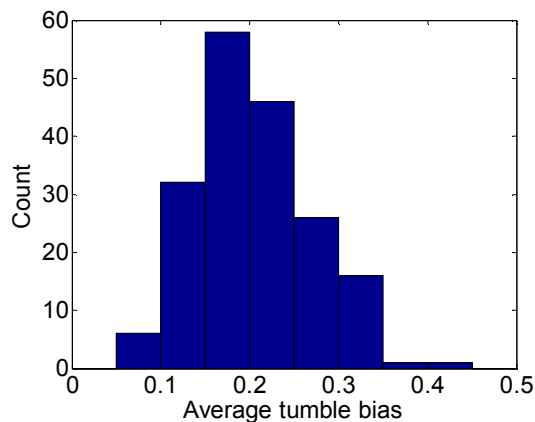


Figure 3-2. Distribution of steady-state tumble bias in a population of 186 wild-type cells. A wide distribution in the steady-state behavior is observed although every cell comes from a genetically identical population.

3.1.2. Run durations in wild-type cells show heavy-tailed exponential distribution

Figures 3-3a,b display the cumulative run duration distributions for 43 individual wild-type and 44 individual PS2001-pMS164 cells at a range of induction levels in the trapping medium (only cells exhibiting 20 or more runs were analyzed). Single-cell distributions are predominantly exponential but also display significant cell-to-cell variability. To determine more accurately the shape of the distributions, we normalized each curve by the individual-cell mean run duration (as determined by an exponential fit) along the time axis (63). *Figures 3-3c,d* show

the result of normalizing the data in *Figures 3-3a,b* maximizing the overlap of the individual distributions.

By pooling all normalized data, we were able to characterize the “average” single-cell run duration distribution (solid black lines, *Figures 3-3c,d*). Both wild-type and PS2001-pMS164 strains displayed exponential distributions at short times, but the former additionally exhibited a

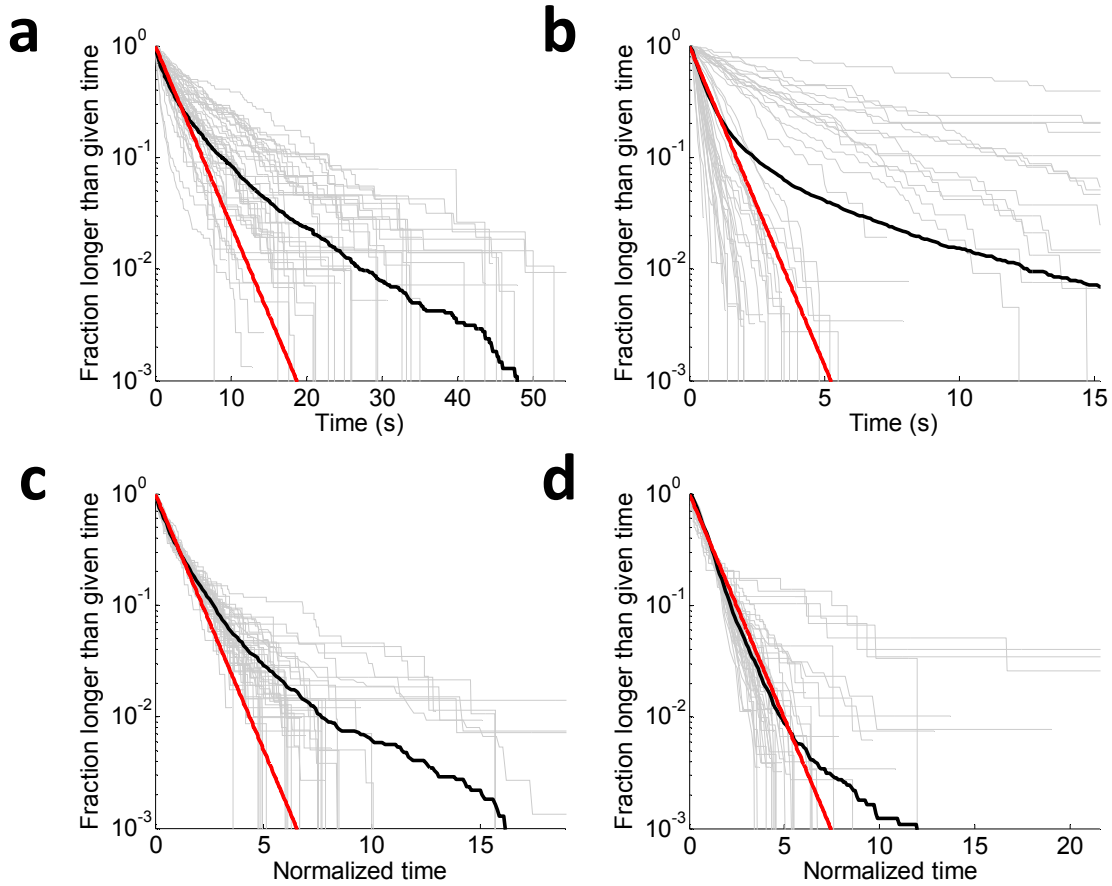


Figure 3-3. Run duration statistics. (a,b) Cumulative distribution of run durations, comprising 5,473 runs observed in 43 wild-type cells (a) and 7,317 runs observed in 44 PS2001-pMS164 strain cells that showed 20 or more runs (b). Each gray line shows the fraction of runs observed from a single cell that were longer than a given time. The thick black line is the population ensemble. The red line is an exponential fit to 90% of the ensemble data, encompassing the shorter events. (c,d) Cumulative distribution for wild-type cells (c) and inducible bias mutants (d) in which individual cell’s run durations were scaled so that the individual’s mean run duration equals the population ensemble mean. This scaling procedure collapses data by effectively removing individual variability, thus revealing the underlying universal behavior in the population ensemble.

pronounced “heavy tail” corresponding to very long runs, which was almost absent in the PS2001-pMS164 strain. The individual wild-type cell distributions further indicate that very long runs are taken in the majority of cells, rather than in a few outliers. Interestingly, this behavior matches that previously reported in single-motor tethered cell studies (2) and may similarly represent the inherent stochasticity in the chemotactic signaling pathway in wild-type cells. The extension of such behavior from the flagellar motor level to the whole-cell swimming level suggests that *E. coli*'s foraging strategy may resemble “Levy-flight”, rather than random-walk (50). This type of search strategy is thought to be advantageous in environments where food sources are sparsely distributed and highly variable in intensity (51, 107). The same kind of evidence for signaling-path stochasticity was not observed in the PS2001-pMS164 strain, where the concentration of signaling protein CheYD13K is externally controlled. The ability to collect sufficient statistics from individual trapped bacteria provides information not available in population distributions. Note that taking the population ensemble of the single-cell distributions prior to normalization (**Figure 3-3a**) does not give an accurate representation of the average distribution (**Figure 3-3c**), emphasizing the importance of collecting single-cell statistics.

3.1.3. Heavy-tailed run duration distribution is also seen in a non-nutritious buffer

In order to rule out the possibility that the heavy-tailed run duration distributions of wild-type cells was caused by active metabolism in the nutrient-rich trapping medium, we examined the

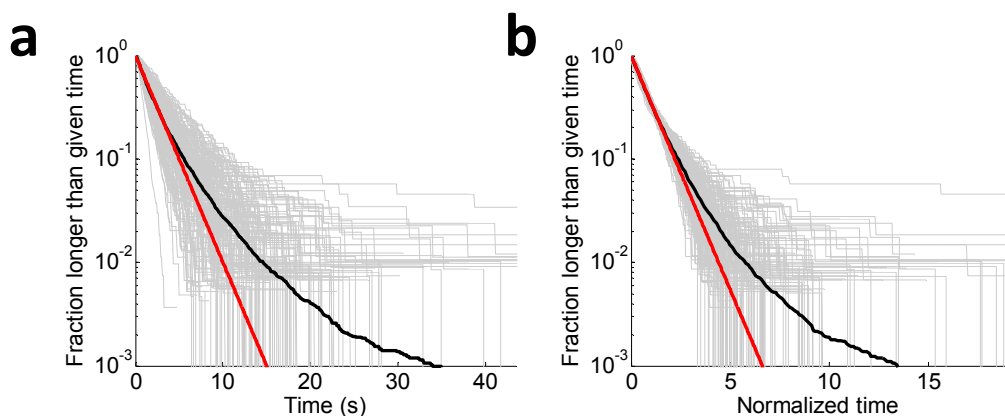


Figure 3-4. Run duration statistics in the absence of nutrients. (a) Each gray line shows the fraction of tumbles that are longer than the given time. Thick black line is from the population ensemble. Red line is an exponential fit to the 90% of the ensemble data, encompassing shorter events. **(b)** Same as **a**, except that individual run duration distributions were scaled so that the mean tumble duration equals the sensembles mean.

run duration distributions of wild-type cells trapped in “trap motility buffer” (*Figure 3-4*). Due to lack of necessary nutrients such as amino acids, trap motility buffer does not support production of new proteins (see *Appendix A.3.* for details on the media used in this work). In trap motility buffer, wild-type run duration distributions also exhibited heavy tails with and without normalization by the mean run duration. This showed that the heavy tails did not come from active metabolism and expression of new proteins..

3.1.4. Tumble durations are exponentially distributed

Examination of tumble duration distributions from both the wild-type and the PS2001-

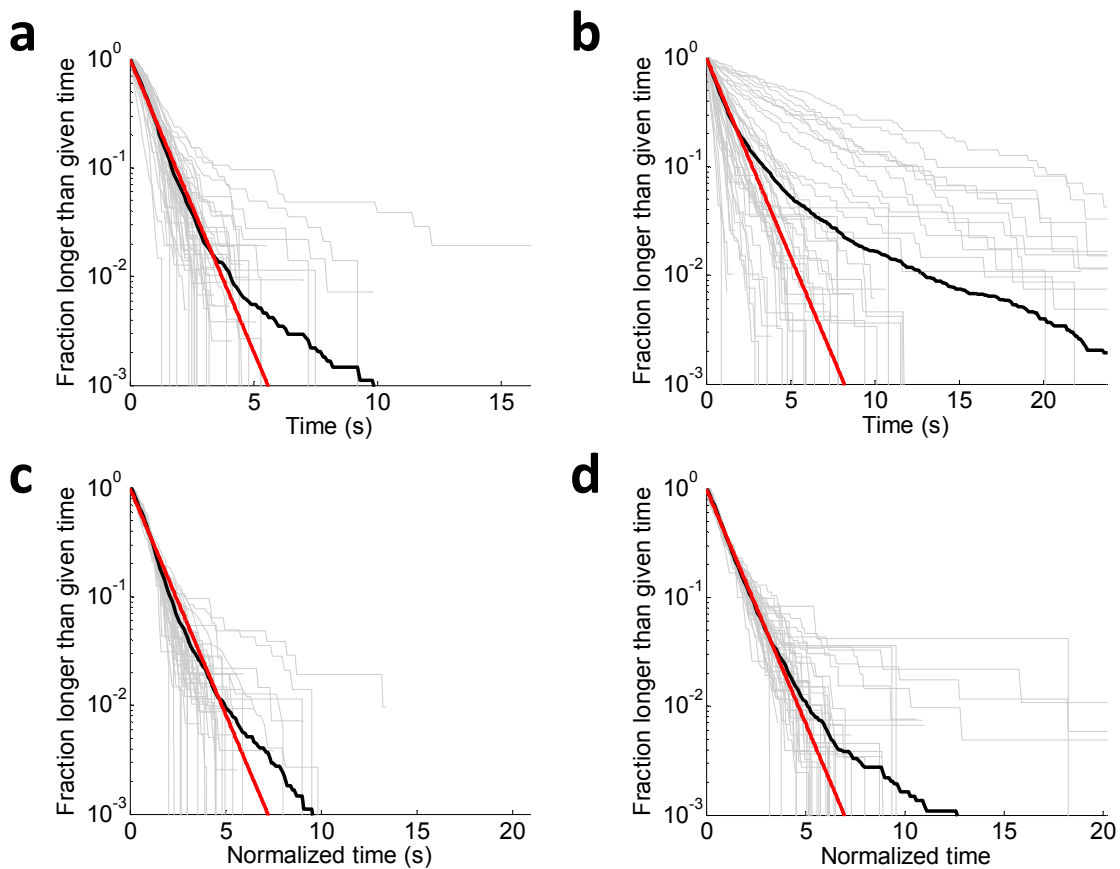


Figure 3-5. Tumble duration statistics. (a) Wild-type cell. Each gray line shows the fraction of tumbles that are longer than the given time. Thick black line is from the population ensemble, comprising 5,348 tumbles observed from 43 wild-type cells. Red line is an exponential fit to the 90% of the ensemble data, encompassing shorter events. (b) Same as a, for the inducible-bias strain PS2001-pMS164. (c) Same as a, except that individual tumble duration distributions were scaled so that the mean tumble duration equals the sensemble mean. This scaling procedure collapses data by effectively removing individual variability, thus revealing the underlying universal behavior in the population ensemble. (d) Same as c, for the inducible-bias strain.

pMS164 strain showed that unlike run durations, tumble durations do not show much deviation from exponential behavior (**Figure 3-5**). This is likely due to the fact that runs result from binding of CheY-P to flagellar motors, whereas tumbles result from unbinding of CheY-P. Since unbinding is a zeroth-order process, it would not be affected by fluctuations in the CheY-P concentration.

3.2. Higher-order features in swimming motility

3.2.1. Observation of multiple swimming states

Our preceding analysis of trapped cells characterized their motility in terms of the standard two-state, “run-tumble” model. Yet, this abstraction of the cell swimming is only a first approximation. Researchers in the field have already pointed to aspects of movement beyond this approximation, including changes in cell velocity after a tumble (63), reversal of swimming direction when the flagellar bundle changes its orientation (108, 109) and changes in motor and swimming velocity as a function of multiple physiological and mechanical factors (60, 101). Most of these observations, however, were sporadic in nature, limited by the noise or short time duration of available techniques.

As shown in **Figures 3-6a**, swimming traces collected by our technique also exhibited “higher order” swimming dynamics, in particular reversals in phase difference between y and z signals (compare $s2$ and $s4$ in **Figure 3-6a**) indicating reversals in swimming direction, and changes in oscillation frequency (compare $s3$ and $s4$ in **Figure 3-6a**) corresponding to changes in swimming speed (3, 101). To fully analyze such higher-order behavioral patterns, we used the continuous wavelet transform to determine not only the body roll frequency Ω but also the phase difference $\Delta\phi$ between y and z signals at every point in time (**Figure 3-6b & c**). 2-D histograms of Ω and $\Delta\phi$ were manually examined to define different swimming states as follows: 1) A threshold in Ω that divides the tumble state from the run states was determined from the local minimum in the Ω histogram. 2) A threshold in $\Delta\phi$ that divides the run states into runs in two opposite directions was determined as the mid-point between the two peaks in the $\Delta\phi$ histogram. 3) If multiple run states were clearly visible from the 2-D histogram in either of the run directions, a threshold dividing those states was determined as the mid-point between the center points in the 2-D histogram. Each time point in the data trace was then assigned to a particular state according to Ω and $\Delta\phi$ values (**Figure 3-6d**). A typical result of these procedures is shown

in *Figure 3-6e*. Detected events shorter than 100 ms were removed for the same reason as discussed in chapter 2. Unlike the case of two-state analysis, we did not obtain two separate multi-state traces from the y and z directions. Instead, the average Ω of the y and z directions was used.

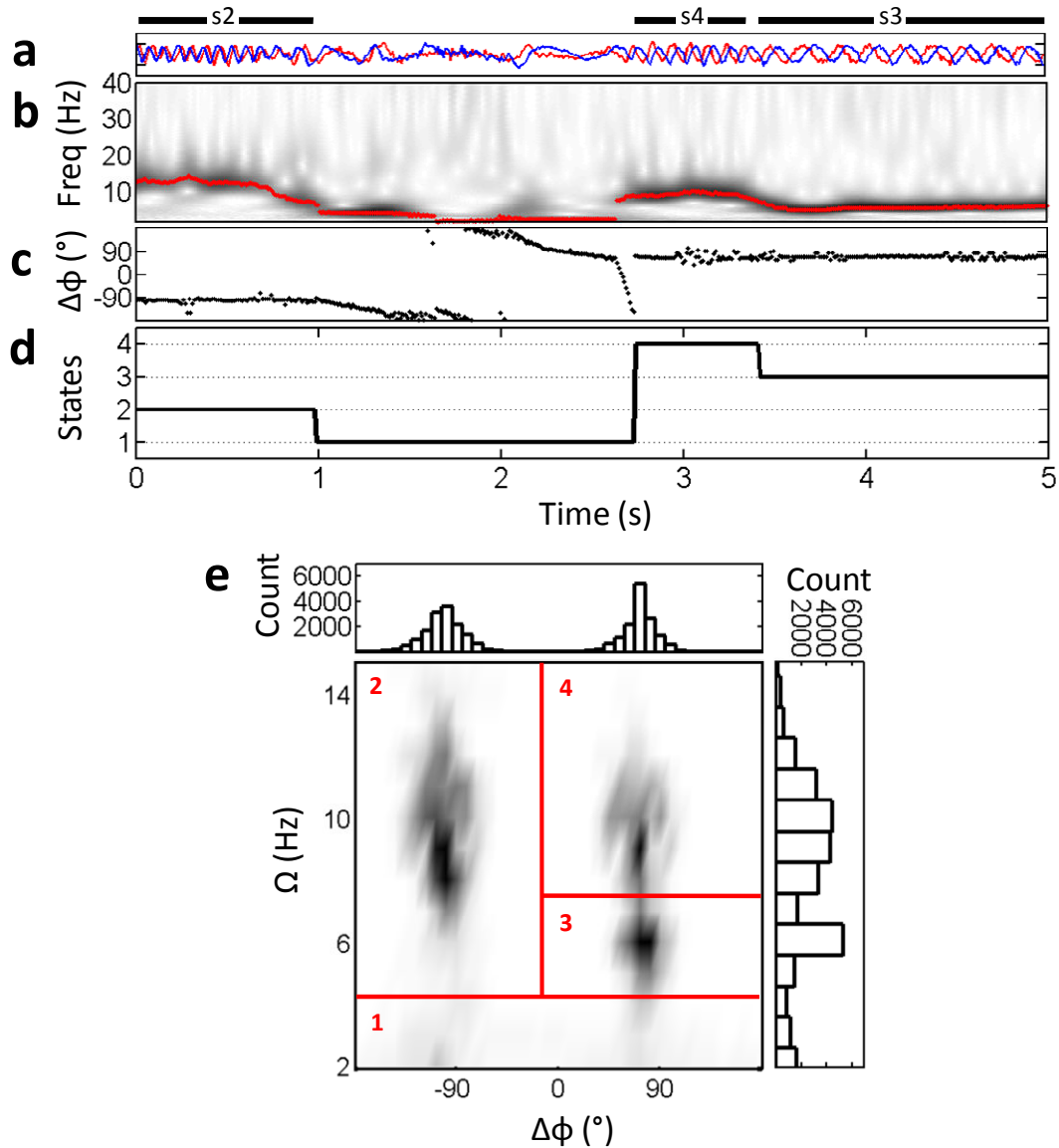


Figure 3-6. Analysis of optical trap data for multi-state swimming behavior. (a) The swimming signal in y (red) and z (blue) directions. **(b)** Continuous wavelet transform of the y signal in the frequency range 2-40 Hz. Peak frequency component at each time point (Ω) is marked by a red dot. **(c)** Phase difference ($\Delta\phi$) obtained from the phases corresponding to the peak frequency components in y and z directions. **(d)** Assignment into different states according to Ω and $\Delta\phi$ values at each time point. **(e)** 2-D histogram of body roll frequency and phase difference between swimming signal in y and z directions. Red lines divide the histogram into regions of different swimming states (1-4) defined by appropriate ranges of Ω and $\Delta\phi$.

3.2.2. Reversals in swimming direction

The majority of trapped wild-type cells (42 of 43 cells) exhibited reversals, illustrated by the two peaks along the horizontal $\Delta\phi$ axis in the histograms. A representative trap signal and a two-dimensional histogram in Ω and $\Delta\phi$ are shown in **Figures 3-7a & b**. Reversals occurred frequently and exclusively after the cell tumbles, on average one out of every 6 tumbles, or every 21.2 ± 1.1 s (mean \pm s.e.m., $n = 859$) (the distribution of inter-reversal durations for a typical cell is shown in **Figure 3-7c**). In certain cases (29 of 42 reversing cells), reversals were also accompanied by an observable change in body-roll rate Ω (**Figure 3-7b**), and thus presumably swimming speed. Interestingly, a similar analysis on the flagellar bundle rotation signal indicated no corresponding changes in rotation rate ω in the majority of cells (data not shown), indicating that reversals provide a mechanism for swimming speed change independently of flagellar motor rotation rate. These observations suggest that reversals may play an important role in the motility of cells.

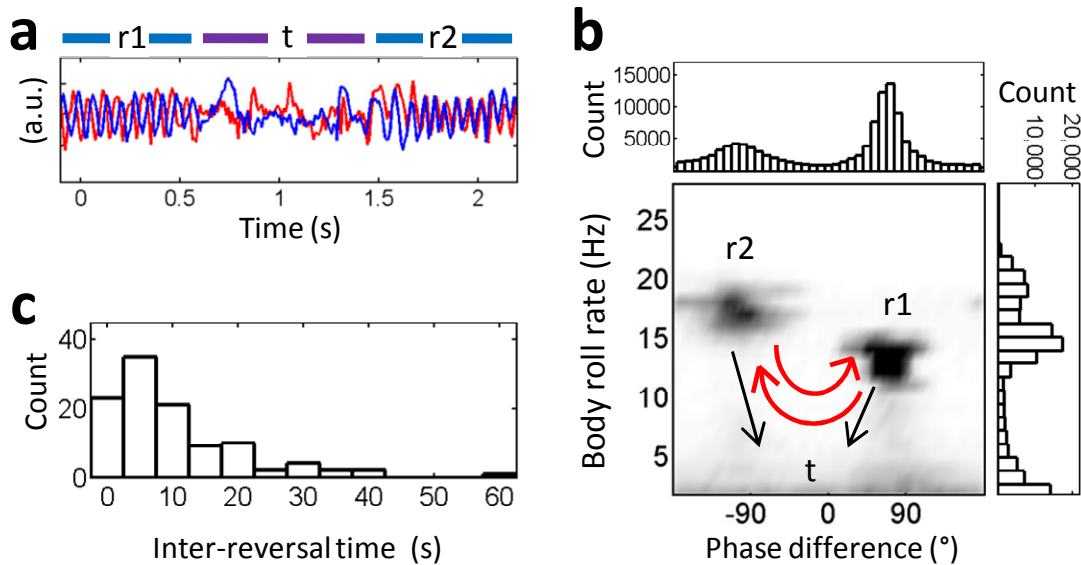


Figure 3-7. Reversals in swimming direction. (a) The swimming signal in y (red) and z (blue) directions showing a reversal in run direction (periods designated r1 and r2) after a tumble (designated t). (b) Image is a two-dimensional histogram of body roll rate (Ω) and phase difference ($\Delta\phi$) between y and z direction signals. All possible transitions between different swimming states are marked by arrows. (c) Waiting time distribution for the transitions highlighted by red arrows in b. All data shown on this figure were from a single swimming trace of a given cell.

It is well established that the distribution of turn-angles after a tumble is biased toward the initial swimming direction (4), and reversals thus may be utilized by cells to randomize their orientation more efficiently. To corroborate this interpretation, we performed cell tracking experiments in a 2-D chamber (see *Appendix B.2.* for detailed methods) (34) with the same strain, and monitored the change in orientation of individual bacteria after a tumble. As shown in *Figure 3-8*, the distribution of angular change was biased toward the initial orientation, as expected, but also indicated events at large angles ($>90^\circ$). The probability of reorientation by large angles was $18.1 \pm 0.1\%$ (mean \pm s.e.m., $n = 61$), consistent with previous studies ($\sim 25\%$ (63)) and in good agreement with the 1 in 6 likelihood of reversing after a tumble observed in the trap. The reversal probability represents the likelihood of reforming the flagellar bundle on the opposite end of the cell after a tumble. The fact that this probability is less than 50% is probably due to the maintenance of a partial bundle during most tumbles (4). Changes in velocity upon reversals likely reflect the fact that bundles formed on opposite ends of the cell may have different spatial arrangements and may thus couple different propulsive forces and torques to the cell body despite identical flagellar rotation rates.

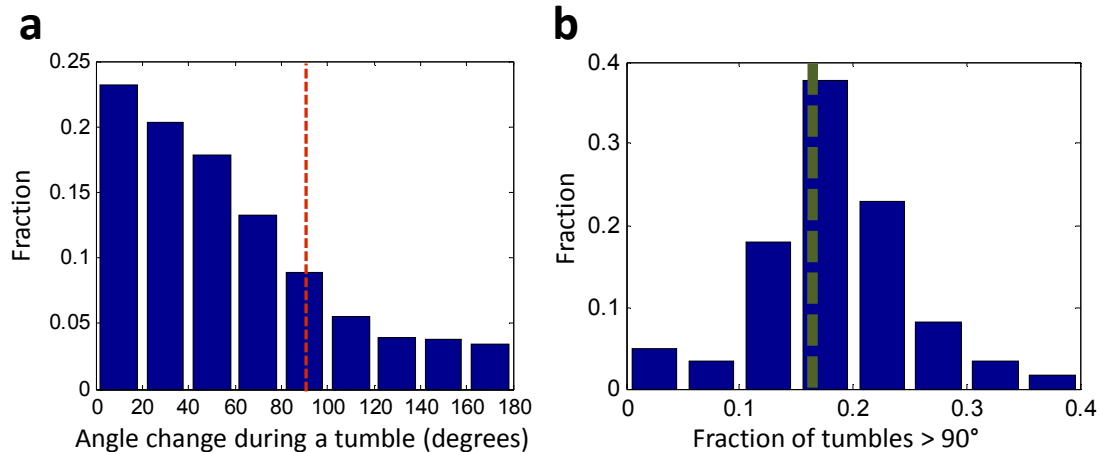


Figure 3-8. Detection of swimming direction reversal in the 2-D swimming assay. (a) Fraction of individual tumble events that result in the given angle changes (change in swimming direction), as detected in a 2-D swimming movie. Changes greater than 90° (marked by the red dashed line) are assumed to correspond to direction reversals of the 2-D swimming cells. **(b)** Fraction of a population of cells that had the given fraction of tumbles that resulted in angle changes greater than 90° . For comparison, the average fraction of tumbles that resulted in direction reversal from 42 wild-type trapped cells is denoted by the green dashed line.

3.2.3. Observation of multiple swimming speeds

Occasionally (in 6 of 42 cells), cells exhibited noticeable, discrete changes in body roll rate with no corresponding change in swimming direction (illustrated by the two peaks along the vertical Ω axis in the histogram in **Figure 3-9b**). Changes in speed occurred both spontaneously, without tumbling (69.5%) as shown in the time trace **Figure 3-9a**, or following a tumble (30.5%). Furthermore, the flagellar bundle exhibited no corresponding changes in rotation rate ω (data not shown). These observations suggest that speed changes may represent different conformational states of the flagellar bundle.

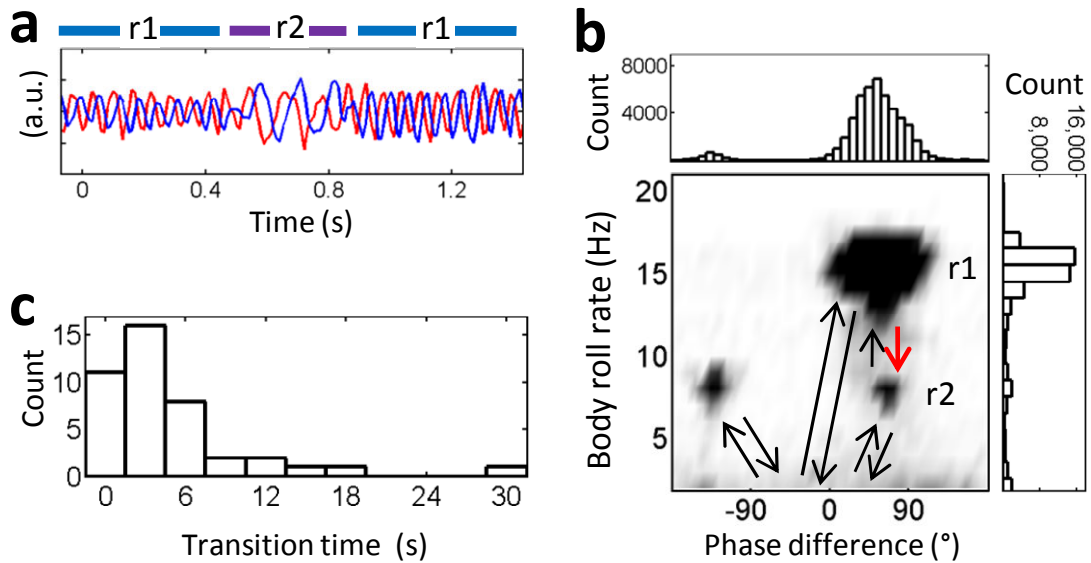


Figure 3-9. Multiple swimming speeds in the same swimming direction. (a) The swimming signal in y (red) and z (blue) directions showing a change in body roll rate (r_2) in the middle of a run (r_1). **(b)** Image is a two-dimensional histogram of body roll rate (Ω) and phase difference ($\Delta\phi$) between y and z direction signals. All possible transitions between different swimming states are marked by arrows. **(c)** Waiting time distribution for the transition highlighted by a red arrow in **b**. All data shown on this figure were from a single swimming trace of a given cell.

The observations of changes in body roll rate Ω with no accompanying reversal in swimming direction or corresponding changes in flagellar rotation frequency ω may again reflect changes in propulsive force and torque coupled to the cell body from the flagellar bundle. In contrast to the case of reversals, however, the spatial orientation of the flagella is unlikely to change in these events, and we speculate that changes in the number of flagella involved in the bundle may be

the ultimate cause. This mechanism may explain why speed changes only occasionally follow tumbles, as counter-rotation of one flagellum is necessary to trigger a tumbling event, but does not guarantee a tumble (4).

3.2.4. Bias in swimming direction

In addition to these higher order features, many cells exhibited asymmetric $\Delta\phi$ distributions (**Figures 3-7b & 3-9b**), indicating a bias in swimming direction. While we found no preferred swimming direction in the cell population, reflecting the fact that our traps do not impose directionality, many individual bacteria do display a statistically significant swimming direction bias.

Bias in swimming direction could be quantified in terms of the number of runs r_{\pm} in the $\pm x$ direction for each individual cell ($\pm x$ corresponds to $\Delta\phi = \pm 90^\circ$ in the histograms). While the “preference” in direction, defined as $(r_+ - r_-)/(r_+ + r_-)$, had a negligibly small value of 0.008 ± 0.061 averaged over the cell population ($49.6 \pm 4.3\%$ of all runs are along the $+x$ direction, compared to $50.4 \pm 4.3\%$ along $-x$), the “bias” in individual cells, defined as $|r_+ - r_-|/(r_+ + r_-)$, had a mean of 0.47 ± 0.04 (all values are mean \pm s.e.m., $n = 42$). This value represents a significant deviation from the expected random statistical variations due to the finite sample size (a total of 5404 runs observed). Although this bias was larger than that reported in a previous study (108), it may similarly reflect asymmetries in the spatial arrangements of flagella at the cell ends.

Chapter 4. Single-cell chemotactic adaptation

In this chapter, we probe the chemotactic response of individual *E. coli* cells to sudden changes in the environment. First we describe the laminar flow gradient used to apply chemical stimuli to trapped cells. Then we describe the chemotactic adaptation response observed at the single cell level. When the responses of a population of cells are averaged together, we see many of the features that were previously described in population studies. However, when we analyze the adaptation response at the single-cell level, we begin to observe detailed features of adaptation that are distinct for each cell and also vary on average as a function of stimulus strength. Additionally, we observe asymmetry in the responses to addition and removal of attractants.

4.1. Optical trapping enables following adaptation kinetics in individual swimming cells

4.1.1. Motivation for studying chemotactic adaptation at the single-cell level

E. coli cells swim by rotating helical filaments (flagella) driven by bi-directional rotary motors (25), alternating between straight-swimming runs and direction-changing tumbles to explore their surroundings (63). The flagellar motor's rotational bias, and thus the cell's swimming behavior, is modulated by chemicals in the surrounding environment. Exposure to attractants causes cells to tumble less, whereas depletion of attractant causes them to tumble more. Modulation of tumble bias leads to net migration toward favorable environments (110). This chemotactic response is governed by a protein network that is well characterized (23, 24). One hallmark of this network is its ability to adapt to a wide range of chemical environments. When cells are exposed to a sudden change in environment, they respond by temporarily changing their swimming behavior (tumbling more or less), but then return over time to their pre-stimulus swimming state (111, 112). Chemotactic adaptation is believed to be exact (29), allowing cells to maintain a high sensitivity to their environment over a wide range of background chemoeffector concentrations.

Various techniques have been used to study chemotactic response and adaptation in *E. coli*. By following populations of swimming cells, the relation between adaptation time and stimulus strength, as well as the robustness of exact adaptation, have been studied (29, 31, 43, 112). Detailed features of the flagellar motor's response to chemical stimuli of various forms have

been characterized by tethering individual cells to the surface of a microscope slide and monitoring the motors' rotational direction (30, 52, 111, 113). More recently, a Förster Resonance Energy Transfer (FRET) reporter system was used to probe the activity of the essential kinase (CheA) in the chemotactic protein network from a population of cells (14, 114, 115). None of these techniques, however, have allowed long-term measurements of the swimming behavior of individual, multi-flagellated cells as they undergo chemotactic adaptation.

In our study, we utilized the optical trap technique described above to apply controlled step-up and step-down chemical stimuli to individual swimming *E. coli* cells and to monitor their chemotactic adaptation. The acquisition of trajectories from many individual cells, for a long duration (> 10 minutes) at high temporal resolution (~ 100 Hz) allowed us to characterize adaptation kinetics at an unprecedented level of detail. In particular, we quantified two features of adaptation: (1) *abruptness*, the degree to which return to pre-stimulus behavior occurs within a small number of run-tumble events; and (2) *overshoot*, the degree of excessive response before the return to pre-stimulus behavior. These features have been previously mentioned in the literature (30, 111, 116-118) but not characterized in detail. In the following sections, we show how we quantified them and describe how they vary as a function of stimulus strength.

4.1.2. Combined optical trapping and laminar flow for stimulus application

To deliver chemical stimuli to the optically trapped cells, we created a spatial concentration gradient of L-aspartate, a chemical attractant for *E. coli*, inside our sample flow chamber. In this chamber, three separate streams containing different solutions merged into a central channel: a “cell-injection” stream, a “blank” stream, and an “attractant” stream (**Figures 4-1a & b**). The cross section of the flow chamber ($100\ \mu\text{m} \times 1000\ \mu\text{m}$ per inlet) and the flow speed ($70\ \mu\text{m/s}$) ensured that fluid flow was laminar with mixing occurring only through diffusion in a predictable manner, creating well-defined boundaries in the chemical profile along the direction perpendicular to the flow. Based on the fluorescence intensity profile measured using Rhodamine B, we estimated that the change from 10% to 90% of the maximum concentration of L-aspartate would occur within $\sim 300\ \mu\text{m}$; see *Figure 4-1c*). In a control experiment using a range of flow speeds, we observed $12 \pm 14\ \%$ and $20 \pm 4\ \%$ decrease in run and tumble durations going from no flow to $70\ \mu\text{m/s}$ flow, respectively. Tumble bias stayed relatively constant ($5 \pm 15\ \%$ increase) over that range (all numbers are mean \pm s.e.m from 8 cells).

In a typical experiment, a swimming cell was captured from the “cell-injection” stream of the flow chamber containing many cells and oriented along the flow direction using the optical traps. By moving the flow chamber using a motorized translation stage, the trapped cell was then

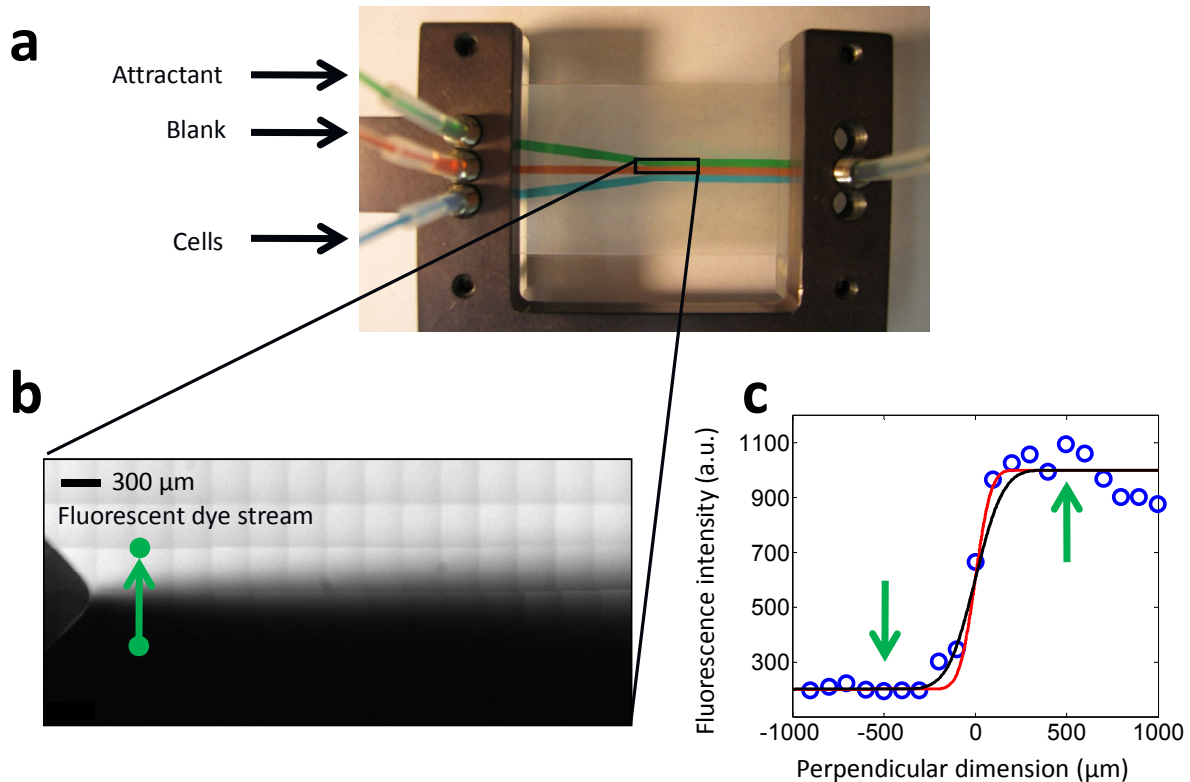


Figure 4-1. Laminar flow chamber. (a) Photo of the laminar flow chamber used in this study. Food dyes of different colors were injected into different streams for illustration. (b) Fluorescence microscopy image of a typical gradient established in the flow chamber. The pixilated appearance of the image comes from the montage of multiple fields of view. Green dots indicate the pre- and post-stimulus measurement locations, and the green arrow indicates the translocation direction of the trapped cell when stimuli are applied. (c) Concentration profile measured under the experimental conditions (linear flow speed = 70 $\mu\text{m}/\text{s}$, 500 μm downstream from where two streams merge). Fluorescence intensity of rhodamine B was measured at various points along the perpendicular direction (blue circles). Red and black smooth lines are theoretical concentration gradient curves with diffusion coefficient $D = 320 \mu\text{m}^2/\text{s}$ (rhodamine B) and $D = 1000 \mu\text{m}^2/\text{s}$ (small molecules), respectively. Green arrows indicate the pre- and post-stimulus measurement locations. Theoretical concentrations at these locations are $< 1\%$ and $> 99\%$ of the maximum concentration at the low and the high ends, respectively. Taking the liberal estimation of $D = 1000 \mu\text{m}^2/\text{s}$ for aspartate, cells that are moved along the concentration gradient at a speed of 100 $\mu\text{m}/\text{s}$ experience the change from 10% to 90% of the maximum concentration over a span of about 3 seconds.

positioned into the “blank” stream containing trap motility buffer. Following measurement of the steady-state swimming behavior for up to 5 minutes, the trapped cell was moved rapidly to the “attractant” stream containing the chemoattractant (L-aspartate) and monitored for another 7 minutes. Since the trapped cells were moved at a speed of 100 $\mu\text{m/s}$, they experienced a chemical stimulus in the form of a step up in attractant concentration over a span of approximately 3 seconds. Step-down stimuli were applied in the reverse manner.

4.1.3. Description of single cell chemotactic adaptation

Figure 4-2a shows three short segments out of a ~5 minute measurement of a trapped cell undergoing a step up in L-aspartate concentration, from 0 μM to 100 μM . In the first segment the cell was in its steady state and exhibited alternating periods of oscillatory and erratic signals corresponding to runs and tumbles. In the next segment the cell underwent a prolonged oscillation (a long run) in response to the applied chemical stimulus. The last segment shows the cell after it adapted to the new level of attractant concentration, where switching between oscillatory and erratic signals resumed. The trap signal was converted to a binary time series of runs and tumbles (**Figure 4-2b**) as described in chapter 2 above.

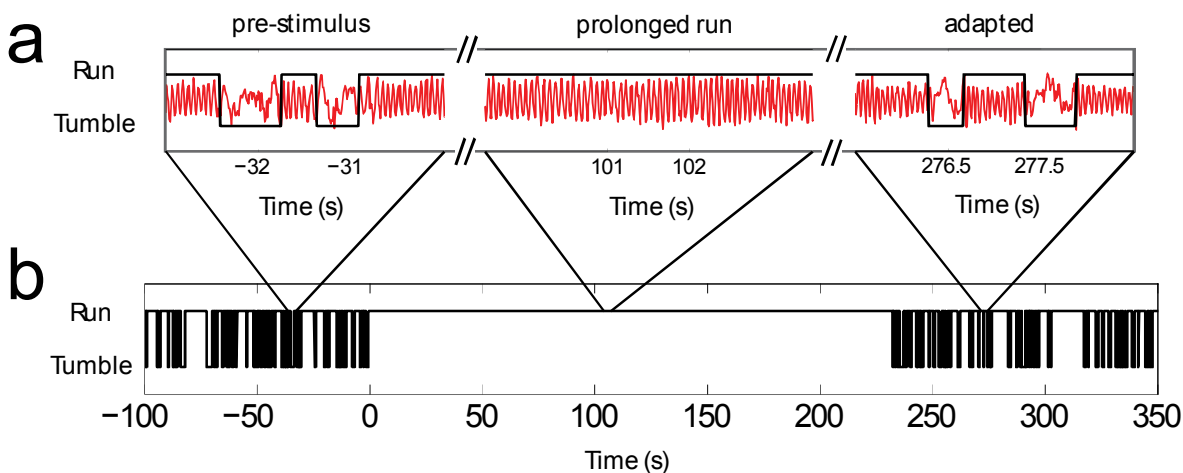


Figure 4-2. Single cell chemotactic response to addition of attractants. (a) Representative cell-body rotation signals from a trapped cell before stimulus (left), during adaptation (middle), and after adaptation is complete (right). Runs and tumbles (black line) are distinguished by using an automated routine described in chapter 2. **(b)** A long-term run-tumble binary time trace obtained from the same cell as in **a**. Stimulus was applied at $t = 0$.

4.1.4. Population average response reproduces old studies

Using the trapping method described above, we characterized the adaptation of individual cells (*E. coli* strain RP437, wild type for chemotaxis (103)) in response to a step up in L-aspartate concentration of varying strength (0 μM to 1 – 1000 μM). From each single-cell binary time series, we determined the adaptation response by calculating the tumble bias in a running 10-s time window (**Figure 4-3**). When the adaptation response was averaged over many individual cells, the average response curve showed a gradual adaptation time course (**Figure 4-4a**), similar to that observed in previous studies (14, 29, 56, 113, 115). For each stimulus, we also determined the average adaptation time, defined as the time elapsed between the application of the stimulus and the tumble bias' recovery to 50% of its pre-stimulus average value.

The dependence of adaptation time on attractant concentration (**Figure 4-4b**) exhibits the Michealis-Menten-like behavior reported in earlier studies (111, 112). The curve is also in quantitative agreement with a recent theoretical model for the chemotactic network (1). In the long term, after the transient response to the step-up stimulus, cells achieved a steady-state tumble bias.

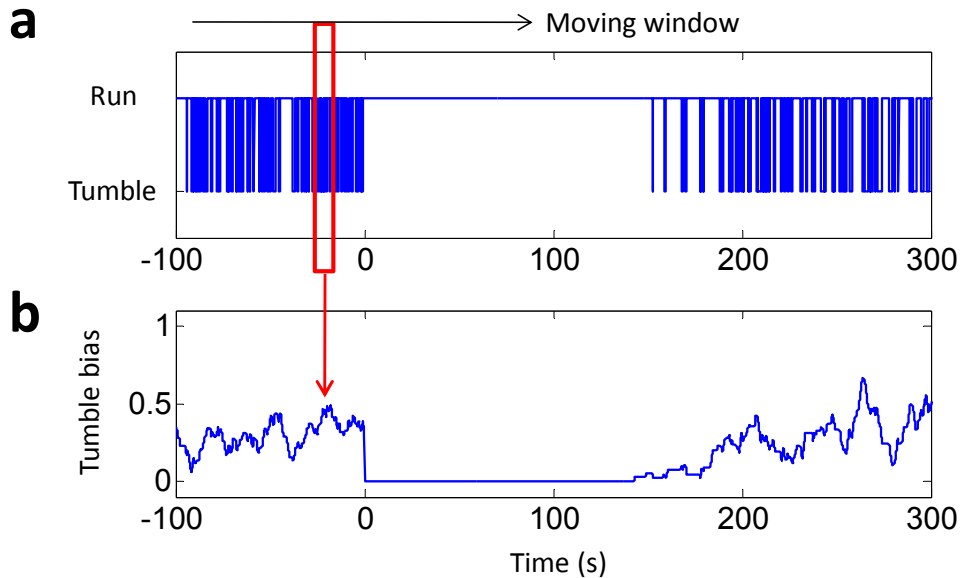


Figure 4-3. Conversion from binary trace to tumble bias time trace. (a) A 400-second segment of a binary series from a single cell that underwent a 100- μM Aspartate step-up stimulus at $t = 0$. **(b)** The tumble bias at each time point ($\Delta t = 0.01$ sec) is determined from a 10-second moving window (red box) over the binary series.

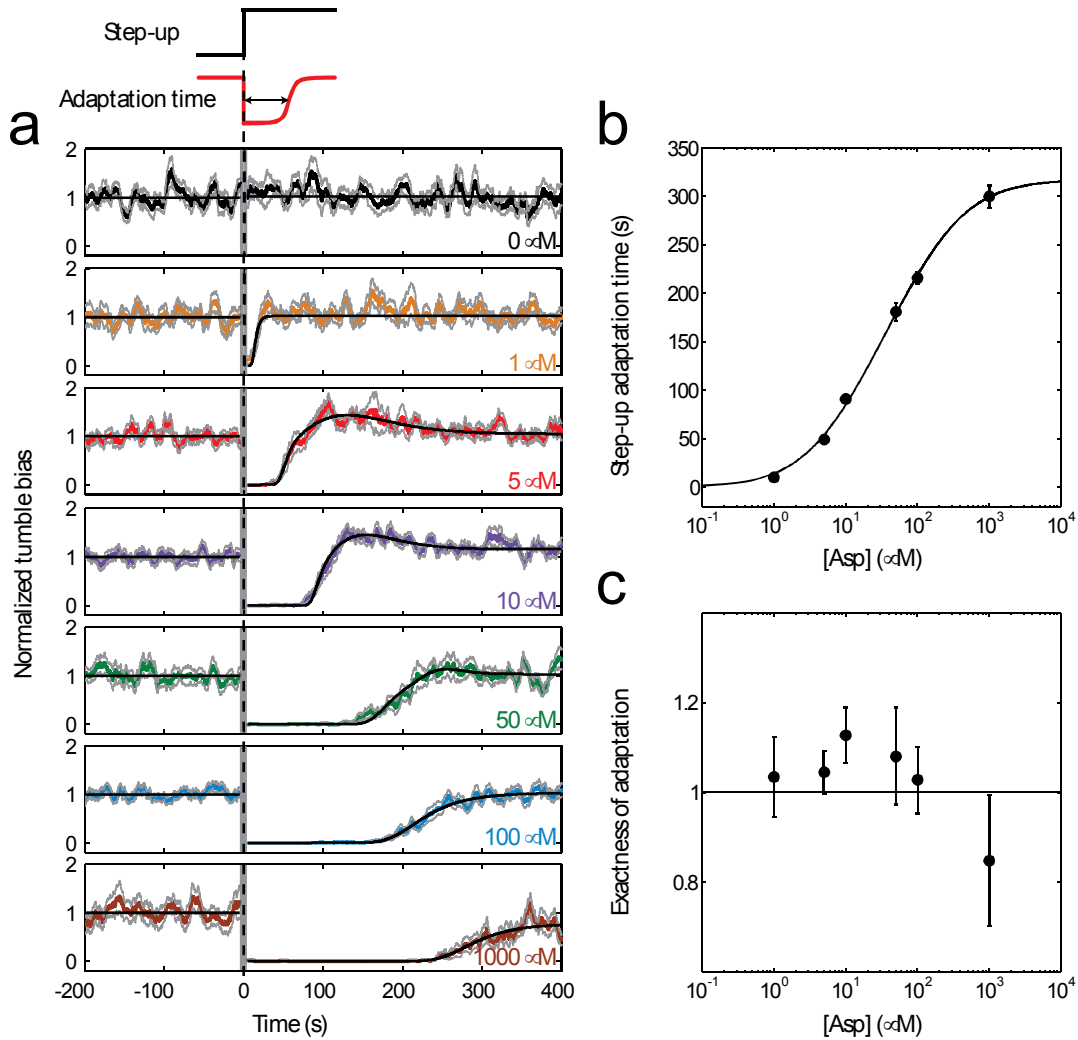


Figure 4-4. Population average response to step-up stimuli. (a) The population-average response to a step up in attractant concentration, delivered at $t = 0$. Individual tumble bias traces were normalized by the mean pre-stimulus tumble bias before averaging across the population. Solid colored lines designate the averaged response at different stimulus levels (changing from 0 μM to 0 (control), 1, 5, 10, 50, 100, and 1000 μM of L-aspartate, color-coded in black, orange, red, purple, green, blue, and brown, respectively). Light grey lines denote one standard error above and below the mean. Black lines are fits to a theoretical model of the chemotaxis network (discussed in chapter 5), with an added overshoot feature. The vertical, grey band near $t = 0$ corresponds to the time when cells were moved along the chemical gradient and data was not recorded. The number of cells included at each stimulus level: $n = 10, 13, 22, 26, 20, 39, 14$, from top to bottom. (b) The average adaptation time as a function of stimulus strength. Adaptation time in step-up experiments (solid black circles) was the time at which the model fit recovered to half the pre-stimulus tumble bias. Errorbars are error estimates obtained from bootstrapping. The solid black line is a fit to a receptor free-energy model (1). (c) The average exactness of adaptation as a function of stimulus strength. Exactness was defined as the ratio of post- to pre-stimulus steady-state tumble bias, Errorbars are error estimates obtained from bootstrapping.

For each stimulus, we determined the exactness in adaptation, defined as the ratio of post- to pre-stimulus steady-state tumble biases. For the majority of stimulus strengths assayed, adaptation was exact within our experimental error (**Figure 4-4c**), as expected from previous studies (29, 30, 115). (For the highest step up in L-aspartate concentration (1000 μ M), we did observe a decrease in steady-state tumble bias post-stimulus, though we attribute this to limited observation time). This agreement with previous experimental and theoretical results on chemotactic adaptation, taken together with our previous report regarding the free-swimming behavior of trapped cells (28), demonstrate that optically trapped cells exhibit a normal behavior in all aspects of motility, including chemotactic response.

4.2. Analysis of chemotactic adaptation at the individual cell level

4.2.1. Event-based analysis of swimming data

The average response curves in **Figure 4-4a**, though useful when comparing our results to previous studies, mask important features of adaptation kinetics at the single-cell level. As seen from the binary time traces (**Figure 4-5**), individual cells exhibited large cell-to-cell variations in adaptation times, due to the stochastic nature of the underlying network reactions as well as variability in the chemotaxis network protein numbers (43). Thus, the population-averaged traces in **Figure 4-4a** smooth over cell-to-cell differences in adaptation kinetics.

In order to elucidate the “typical” behavior of the individual cell, we analyzed our data using a recently introduced scheme (30), in which individual traces are indexed by “events”—run and tumble pairs—rather than time. In this method, each run-tumble pair was considered an event, with a corresponding tumble bias value defined as tumble duration / (run duration + tumble duration). For visualization purposes, each event was assigned a time-duration of (run duration + tumble duration) so that the time course of the event-based traces matched the time course of the original traces (**Figure 4-6**).

Population-averaged event traces were also constructed event-by-event, where the tumble bias values were averaged across the population for each event, and the corresponding average duration was assigned. **Figure 4-7a** displays the result of averaging individual traces according to run-tumble event number, aligned relative to the delivery of the stimulus (i.e. run-tumble events were enumerated from the time the stimulus was applied). The ordinate represents the

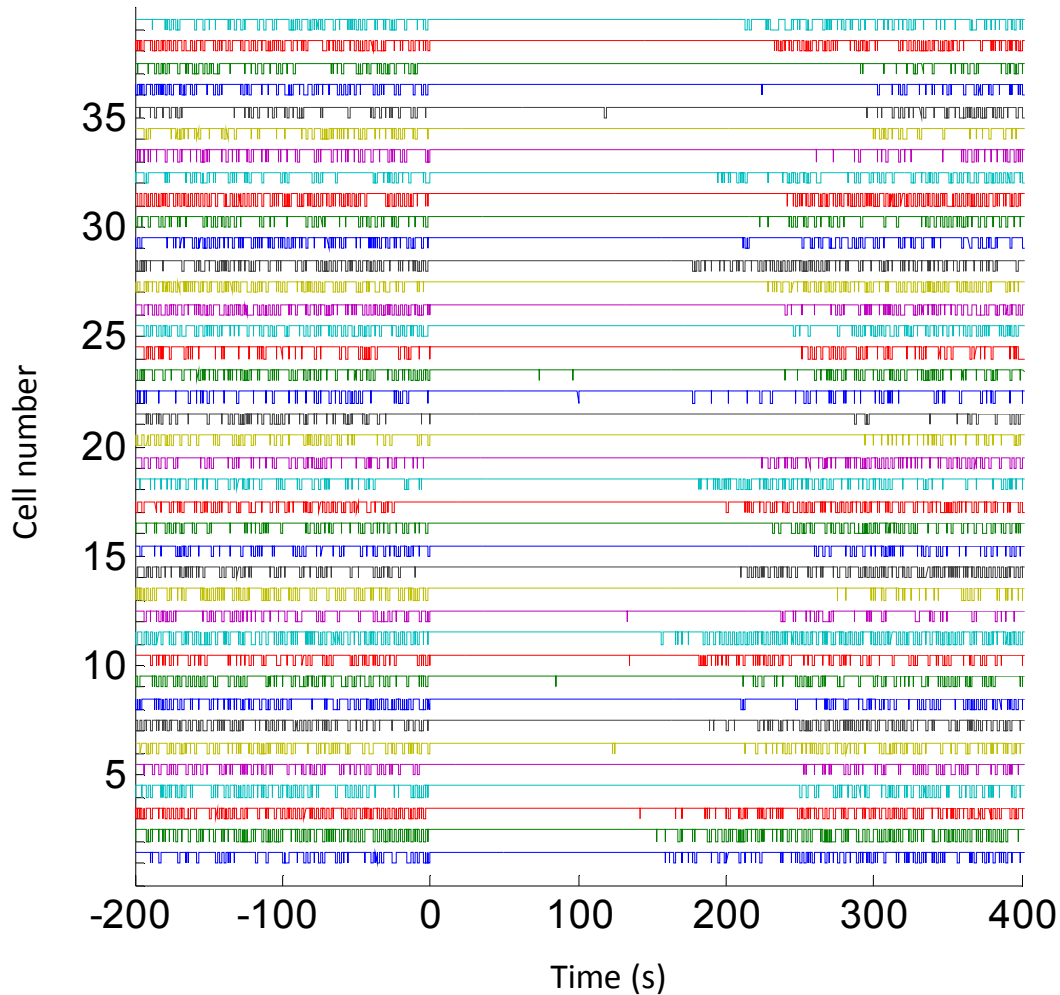


Figure 4-5. Cell-to-cell variation in adaptation time. Individual binary traces for 39 cells that underwent a 100- μ M L-aspartate step-up stimulus at $t = 0$ are shown. All cells initially respond to the step-up stimulus by entering a prolonged run state. The subsequent return to steady-state run-tumble switching occurs at different times for different cells.

mean tumble bias, the abscissa the mean duration of the i -th run-tumble pair averaged across the cell population. This averaging scheme is not subject to stochastic variability in run or tumble duration, and thus better captures the “typical” adaptation kinetics of individual cells.

4.2.2. Abruptness of adaptation as a function of stimulus

In comparison to the population-averaged response curves in **Figure 4-4a**, the corresponding event-averaged curves in **Figure 4-7a** reveal the “abruptness” with which individual cells adapt. The predominant adaptive response to a step-increase in attractant consisted of a single, long

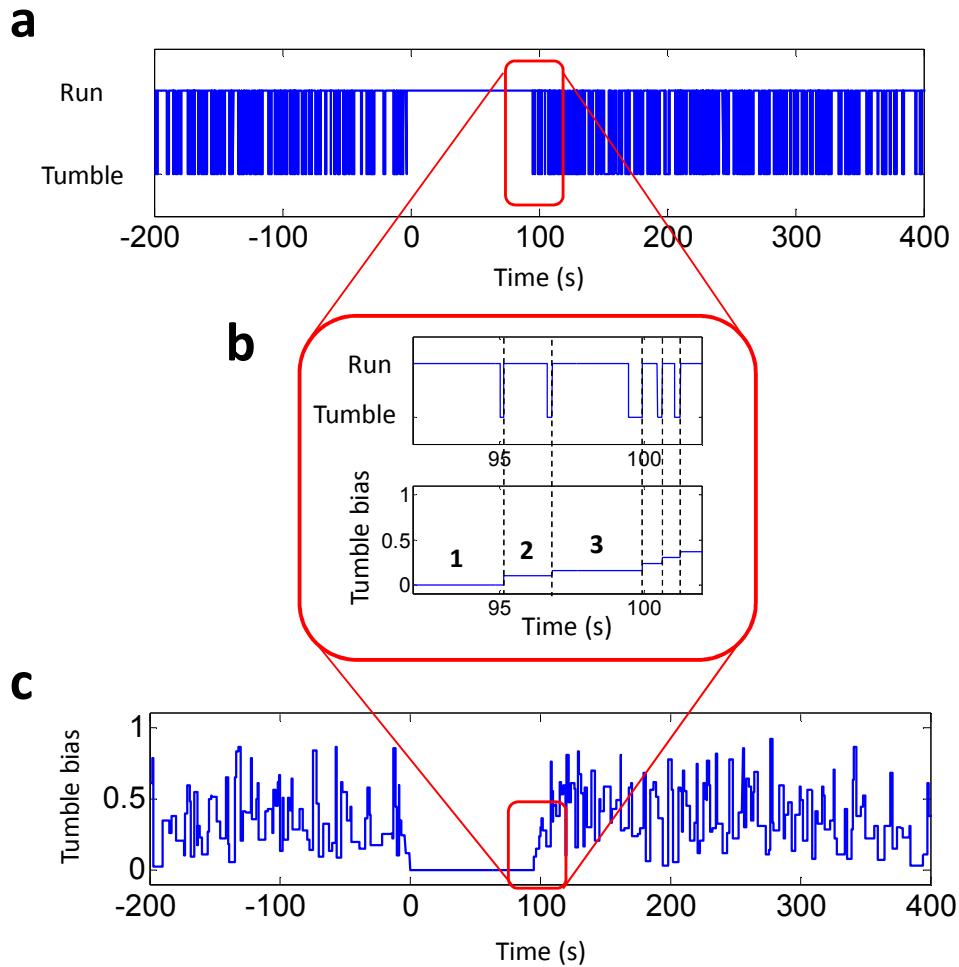


Figure 4-6. Conversion from binary trace to tumble bias event trace. (a) A 600-second segment of a binary series from a single cell that underwent a 10- μ M L-aspartate step-up stimulus at $t = 0$. **(b)** The tumble bias is calculated for each event pair consisting of a run and a tumble. Events are enumerated starting from the first event following the stimulus. **(c)** In addition to the tumble bias value, each event is aligned in time to the binary trace for visualization purposes.

run-tumble event (specifically, a single long run; tumble duration did not change significantly), after which the cell's swimming returned to its pre-stimulus behavior. Abrupt adaptation kinetics at the level of individual motors were reported many years ago for the case of saturating stimuli (111) and more recently for small stimuli (30). However, a detailed characterization of this feature, over a wide range of chemical stimuli strengths, has not been conducted.

To quantify adaptation abruptness in individual cells, we determined the number of run-tumble pair “events to adaptation” (ETA) using the Mann-Whitney U-test, a non-parametric statistical test for assessing the null hypothesis that two independently obtained samples are equal in magnitude (119). The reference sample consisted of 65 events pre-stimulus, normalized by the mean of the last 20 events post-stimulus to compensate for the possibility of non-exact adaptation. The test sample consisted of a moving 5-event window immediately following the application of stimulus. The 5-event window was moved one event at a time until adaptation was scored when the U-statistic of the test sample approached the expected U within 50% of the standard deviation in U. ETA was the number of events that led to adaptation. We found that our statistical analysis was more robust when using parameters that increase in response to stimuli and then fall back down as the cell adapts (i.e. run duration for step up, tumble bias for step down).

Histograms of single-cell ETAs are shown in **Figure 4-7b**, and are well described by exponential distributions. The ETAs were also used to define an adaptation time for individual cells, determined by summing the durations of all run-tumble pair events leading up to adaptation. **Figure 4-7c** shows the corresponding histograms of single-cell adaptation times at each stimulus level, with fits to normal distributions. We note that the single-cell-based estimates of adaptation times were in good agreement with the population-based estimates (Compare **Figures 4-4b and 4-7d**), as expected. The histograms of ETA revealed an unexpected feature of adaptation: the abruptness in an individual cell’s adaptive response depends on the stimulus strength. At low stimulus levels (up to 10 μM), the majority of individual cells adapted within one event. In contrast, for higher stimulus levels (50 – 1000 μM), event durations were typically longer than their steady-state value for several events following the stimulus. In **Figure 4-7e**, the average ETAs (extracted from the histograms in **Figure 4-7b**) are plotted against the stimulus strength. The average ETA exhibits an almost stepwise increase from 1 to ~ 5 as the stimulus level exceeds 50 μM . ETAs obtained from the population-averaged event-based adaptation curves in **Figure 4-7a** exhibited similar behavior (**Figure 4-7e**). We discuss possible explanations for the stimulus-dependent abruptness of adaptation exhibited by individual cells in chapter 5 below.

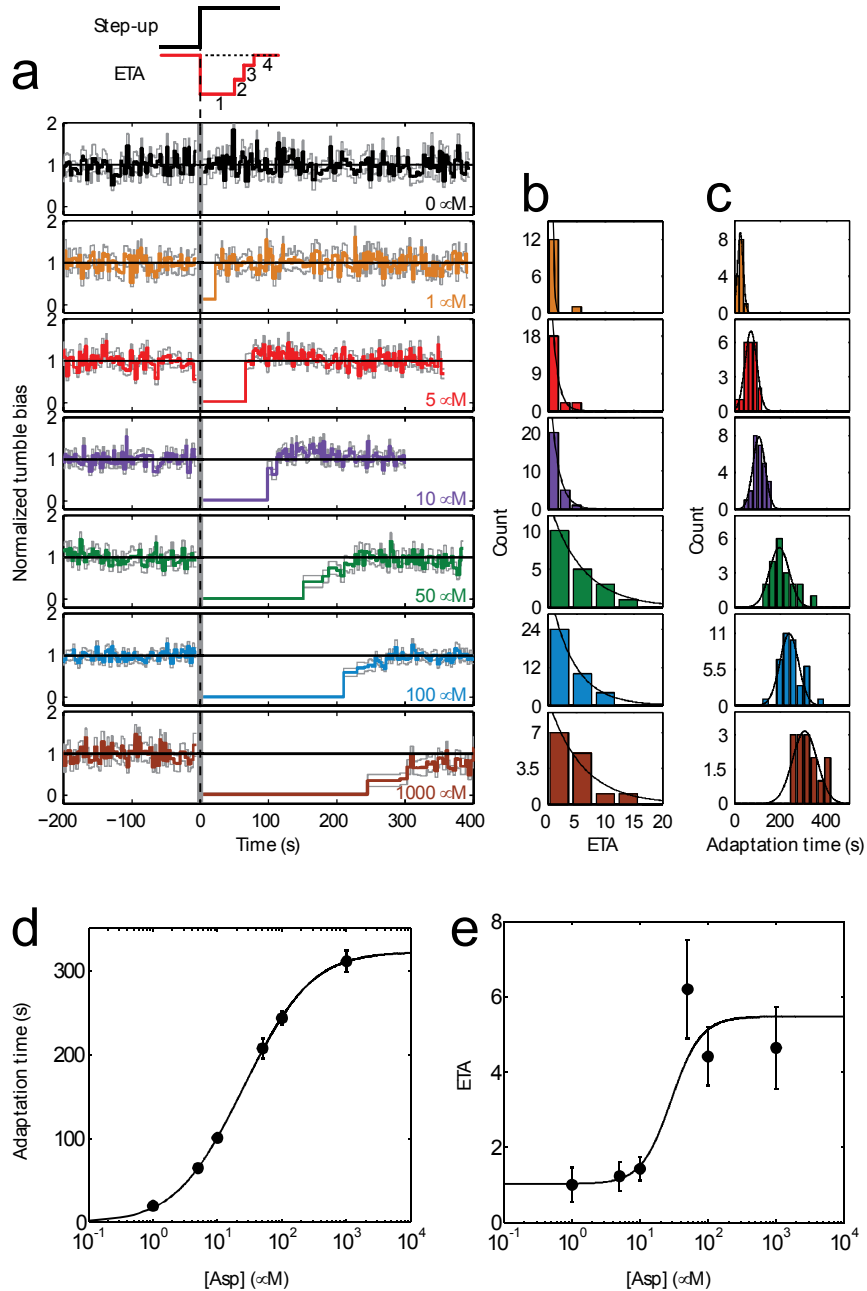


Figure 4-7. Abruptness of adaptation to step-up stimuli. (a) The event-based average response to a step-up in attractant concentration, delivered at $t = 0$. Individual tumble-bias traces were normalized by the mean pre-stimulus tumble bias. Color notations are the same as in **Figure 4-4** above. The vertical, grey band near $t = 0$ corresponds to the time when cells were moved along the chemical gradient and data was not recorded. $n = 10, 13, 22, 26, 20, 39, 14$, from top to bottom. (b) Histograms of the number of run-tumble pair events to adaptation (ETA) from individual cells. Black lines are fits to exponentials. (c) Histograms of adaptation time of individual cells. Black lines are fits to Gaussians. (d) The average adaptation time obtained from the histograms in c. Errorbars are standard errors of the mean. (e) The average number of events to adaptation (ETA) as a function of stimulus strength. Errorbars are standard errors of the mean. The solid black line is a fit to a sigmoid.

4.2.3. Overshoot response

After the application of a step-up stimulus and the resulting long run-tumble event(s) discussed above, many cell traces exhibited an “overshoot”, during which the tumble bias exceeded the pre-stimulus steady state. The tumble bias eventually returned to the pre-stimulus value. This feature was observed in population-averaged traces (*Figure 4-4a*) and event-averaged traces (*Figure 4-7a*) alike, and quantified at the single-cell level. Normalized overshoot amplitude was calculated using the formula $(\text{Bias_middle} - \text{Bias_after}) / \text{Bias_after}$, where Bias_middle was the mean tumble bias of 6-th through 15-th events following adaptation as determined above, and Bias_after was the mean tumble bias of the final 20 events post-stimulus.

Figure 4-8a displays the average amplitude of the overshoot for different stimulus strengths. Interestingly, the overshoot amplitude exhibited a non-monotonic dependence on stimulus strength, negligible at our lowest (1 μM) and highest (1 mM) stimulus strengths but peaking to a value of $\sim 20\%$ at intermediate (5-50 μM) strengths. An overshoot response of individual motors was reported many years ago (111) but is absent from later studies of chemotactic adaptation (29, 113, 115) (see Discussion below). *Figure 4-8b* displays the corresponding single-cell histograms of the overshoot.

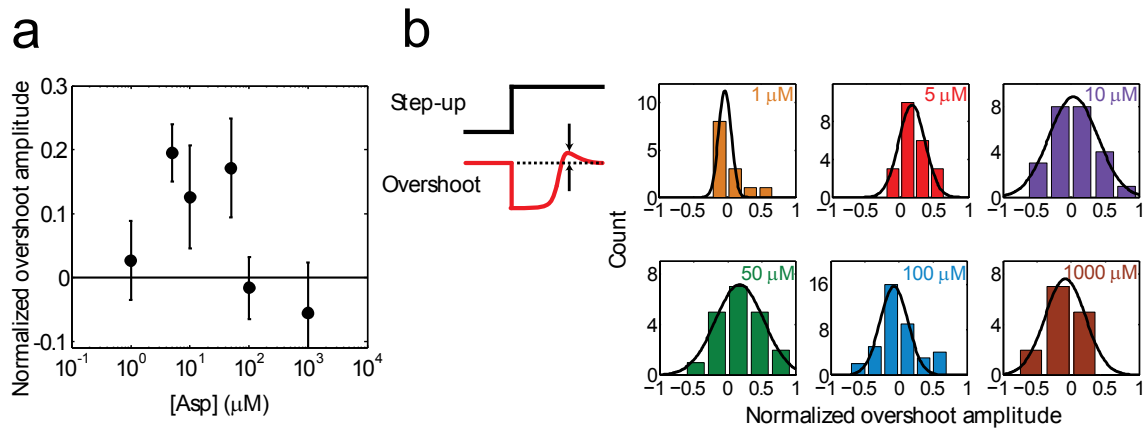


Figure 4-8. Adaptation overshoot in response to step-up stimuli. (a) The overshoot amplitude, normalized by the steady-state tumble bias and averaged over individual cells, is plotted as a function of the step-up. Errorbars are standard errors of the mean. (b) Histograms of individual cells’ overshoot amplitudes in response to step-up stimuli. Color notations and sample sizes at each stimulus level are the same as in *Figure 4-4*.

4.3. Adaptation kinetics show asymmetry in response to a step up vs. a step down

In addition to the above measurements, we also quantified the response of individual cells to a step-down in L-aspartate concentration. In agreement with recent reports (115), the chemotactic response was not merely a mirror image of that seen for a step-up stimulus; distinctly different adaptation kinetics were observed in the two cases (compare **Figure 4-4a and 4-9a**). Cells adapted to step-down stimuli in much shorter times (110). Whereas adaptation times for the step-up stimuli ranged from ~ 15 seconds to over four minutes in the range of concentration-jumps tested, adaptation times for the step-down stimuli saturated at ~ 15 seconds and showed little variation over two orders of magnitude change in the step-down concentration-jumps (**Figure 4-9b**).

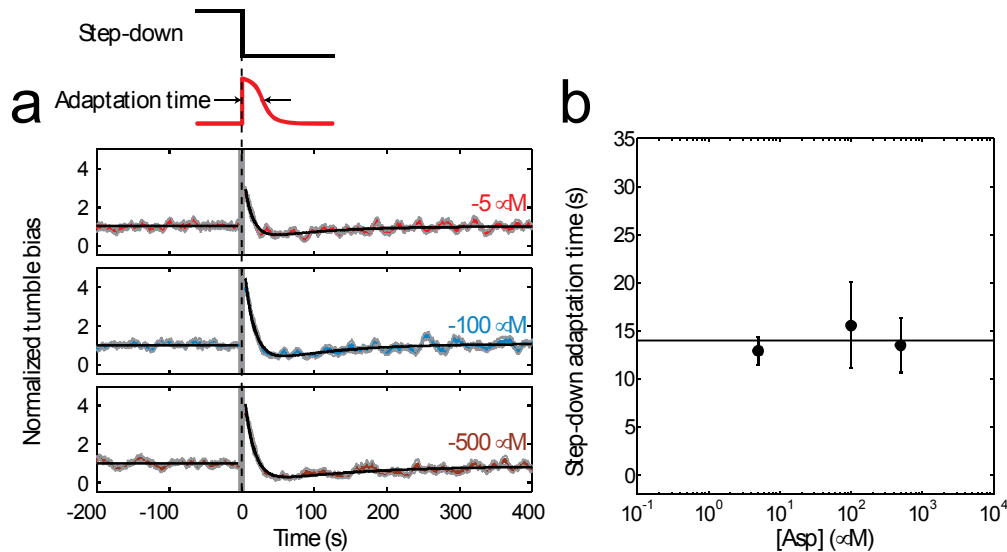


Figure 4-9. Population average response to step-down stimuli. (a) The population-average response to a step down in attractant concentration, delivered at $t = 0$. Individual tumble bias traces were normalized by the mean pre-stimulus tumble bias before averaging across the population. Solid colored lines designate the averaged response at different stimulus levels (changing from 5, 100, 500 to 0 μM of L-aspartate, color-coded in red, blue, and brown, respectively). Light grey lines denote one standard error above and below the mean. Black lines are fits to sum of two exponentials. The vertical, grey band near $t = 0$ corresponds to the time when cells were moved along the chemical gradient and data was not recorded. The number of cells included at each stimulus level: $n = 13, 15, 14$, from top to bottom. **(b)** The average adaptation time as a function of stimulus strength. Adaptation time in step-down experiments (solid black circles) was the time at which the model fit recovered halfway from the peak to the pre-stimulus tumble bias. Errorbars are error estimates obtained from bootstrapping. The solid black line is the mean of three data points.

Analysis of individual cell traces (*Figure 4-10a*) revealed additional differences. In contrast to adaptation to step-up stimuli, the average number of run-tumble events before adaptation to a step-down was consistently high (~ 7) and was largely independent of stimulus strength (*Figure 4-10b*). This behavior is explained by the fact that run-tumble events were significantly shorter during step-down stimuli compared to events during a step up (*Supplementary Figure 6C and D*) and the adaptation time was uniform (~ 15 seconds) across the range of stimulus strengths. Finally, adaptation traces exhibited significant overshoot ($\sim 20\%$) at all stimulus strengths tested (*Figure 4-10c & d*). Overshoot was noticeable in the population-averaged traces as well.

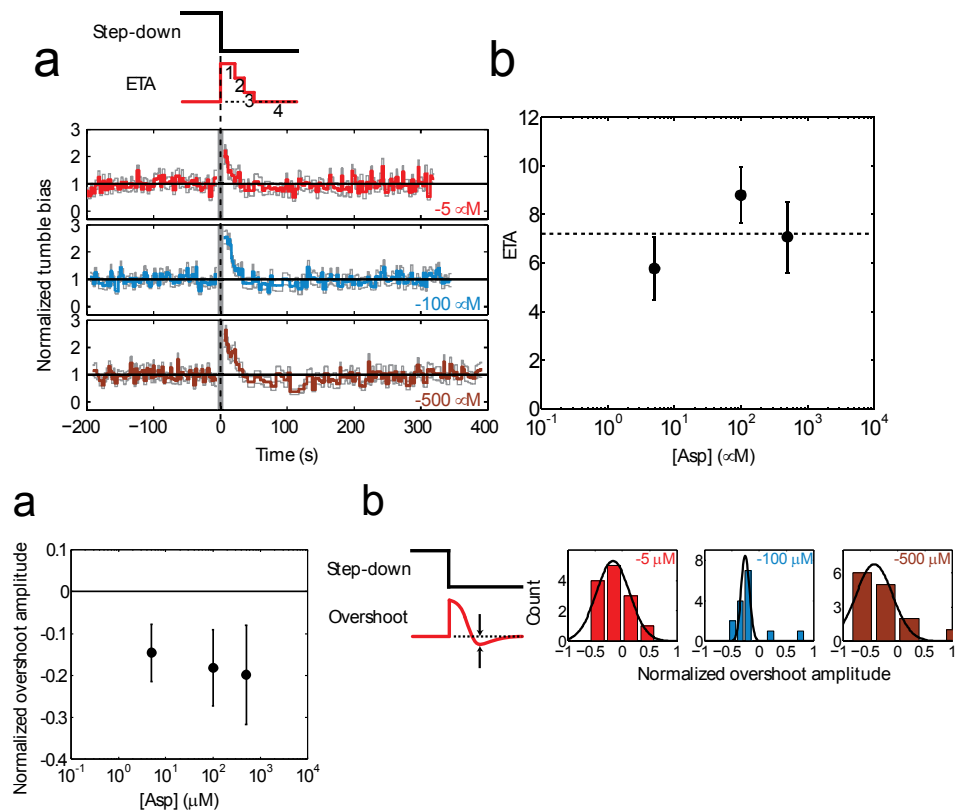


Figure 4-10. Abruptness of adaptation and overshoot to step-down stimuli. (a) The event-based average response to a step-down in attractant concentration, delivered at $t = 0$. Individual tumble-bias traces were normalized by the mean pre-stimulus tumble bias. Color notations and sample size are the same as in *Figure 4-9* above. (b) The average number of events to adaptation (ETA) as a function of stimulus strength. Errorbars are standard errors of the mean. The solid black line is the mean of the three data points. (c) The overshoot amplitude, normalized by the steady-state tumble bias and averaged over individual cells, is plotted as a function of the step-up. Errorbars are standard errors of the mean. (d) Histograms of individual cells' overshoot amplitudes in response to step-down stimuli.

Chapter 5. Theoretical investigation of chemotactic adaptation in *E. coli*

In this chapter, we examine chemotactic adaptation in *E. coli* within the framework of an existing mathematical model (1, 120). We begin by reviewing the *E. coli* chemotaxis network while describing the relevant model parameters. We then turn our attention to the molecular mechanism behind the observed abruptness in adaptation (chapter 4). We argue that abruptness cannot be explained by the ultrasensitive switching behavior of the flagellar motor (121). Instead, we suggest a model where dynamic clustering of chemoreceptors gives rise to both the abruptness in adaptation and its dependence on stimulus strength. Lastly, we investigate the effect of noise in the chemotaxis signaling pathway on abruptness of adaptation.

5.1. Review of the *E. coli* chemotaxis network

A cell's swimming state is controlled by a cascade of interactions (23, 24) (**Figure 5-1**). Chemical input signals from the environment are sensed by transmembrane receptors that are coupled to the intracellular kinase CheA. Commonly, CheA activity is parametrized by the quantity A , the probability (ranging from 0 to 1) that the kinase is in its active (phosphorylating) state. The activity is a function of the receptor ligand concentration (122); an increase in

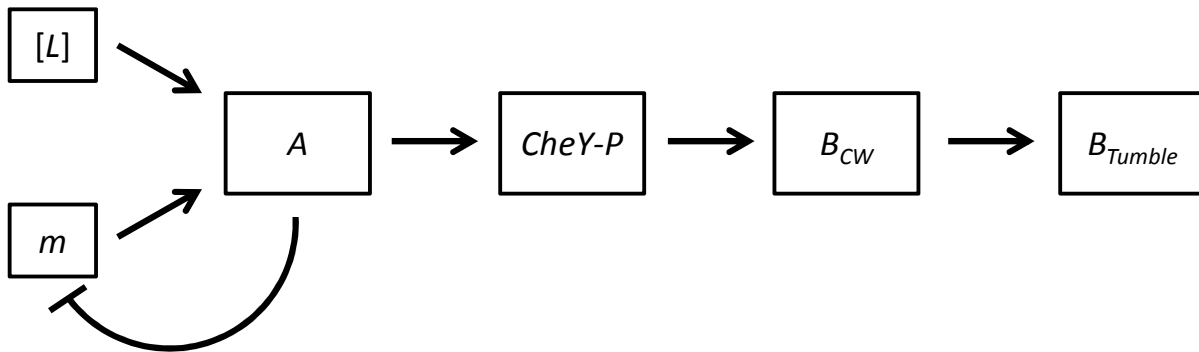


Figure 5-1. Cascade of events leading to *E. coli*'s swimming behavior. Ligand concentration ($[L]$) and methylation level (m) determine the activity of CheA (A), which phosphorylates CheY into CheY-P ($CheY-P$). CheY-P then binds flagellar motors and biases them for counter-clockwise rotation (B_{CW}). Hydrodynamic Interaction of multiple rotating flagella on a given cell determines the cell's swimming behavior, tumble bias (B_{tumble}). Adaptation to persistent changes in ligand concentration occurs via CheA activity's negative feedback on the methylation level.

chemoattractant leads to a decrease in activity and vice versa. In addition to ligand binding, methylation of the receptors also modulates kinase activity; the higher the methylation, the higher the activity (123). Thus,

$$A = A([L], m), \quad (5-1)$$

where $[L]$ is the ligand concentration and m is the number of methylated receptor sites (ranging from 0 to 8). Notably, A is an *increasing* function of the methylation m . Receptors are also known to interact and cooperatively modulate CheA kinase activity (14, 124). Ligand binding to one receptor affects the CheA activity in a neighborhood of N interacting receptors (124). The net consequence of this interaction is to multiply the effect of methylation m on A by the interacting cluster size N (124, 125).

At the same time, the methylation rate of the receptors is also a function of CheA activity. Methylation and demethylation are controlled by the proteins CheB and CheR, respectively, whose activity depends on A (31). Thus,

$$\frac{dm}{dt} = F(A). \quad (5-2)$$

Though the detailed functional form of $F(A)$ depends on the model used (1, 120), for our purposes it is sufficient to state that $F(A)$ is a *decreasing* function of A ; as CheA activity increases, the rate of methylation decreases. Equations (5-1) and (5-2) describe the negative feedback loop that is responsible for adaptation. As CheA activity is perturbed from its steady state (by a step-up or step-down in chemoattractant concentration, for example), this feedback loop ensures its eventual return to the same steady state (29, 31, 52, 126).

The next link in this chain of interactions is the phosphorylation of the signaling protein CheY by CheA. In its active form, CheY-P binds to the flagellar motors and induces a conformational switch from CCW to CW rotation (33, 34). This interaction is known to be highly cooperative, and described by a sigmoidal function (121). At sub-saturating conditions, the concentration of CheY-P is proportional to CheA activity, and the CW bias of the motor B (defined as the fraction of time spent in the CW state, a number ranging from 0 to 1) can be written as a Hill function

$$B = \frac{A^H}{A^H + K_A^H}, \quad (5-3)$$

where $H \approx 10$. Importantly, measurements have shown that the steady-state CheA activity sits in the steepest part of this function: $A_\infty = 0.33$, $B_\infty = 0.35$ (where the subscript ∞ denotes the steady state), and $K_A = 0.35$ (1, 121).

The last component of the cascade of interactions occurs between the flagellar motors and the whole cell. As individual motors that comprise the flagellar bundle undergo a conformational switch from CCW to CW rotation, the cell swimming state switches from a run to a tumble (127). It is important to note that the individual motors in the cell are not perfectly synchronized (67, 68, 128), and that the manner in which the collective CCW/CW state of the motors dictates the run-tumble state of the whole cell remains poorly understood (3, 4).

5.2. Ultrasensitive flagellar motor is not the cause of abruptness

In the literature, chemotactic adaptation is typically described as a gradual process (14, 29, 56, 110, 113, 115). It is important to note, however, that those studies all involved averaging over multiple cells. As noted in chapter 4, such averaging masks important features of single-cell adaptation kinetics, due to the asynchrony in adaption between different cells. In studies where the response of individual flagellar motors was examined, the motors were described to undergo abrupt switches in behavior during the course of adaptation (30, 111), but this abruptness was not quantified in detail. Our measurements extended these findings by quantifying the level of abruptness as a function of stimulus strength, and by moving from the level of single flagellar motors to the (physiologically relevant) whole-cell swimming behavior.

What is the source of abrupt adaptation, and what makes the abruptness stimulus-dependent? As noted above, abruptness is already observed at the single-motor level (30). Therefore, the source of abruptness cannot be in the transition from the individual motors to the whole-cell behavior. Rather, the source must lie upstream in the cascade of interactions. At first glance, it is natural to assume that the switch-like manner in which the flagellar rotational state depends on CheY-P level (equation (5-3)) plays a role in abruptness of adaptation. However, we found that this cooperativity, parameterized by the large Hill coefficient ($H \sim 10$) (121), has little to no

effect on the abruptness of adaptation (**Figure 5-2**). The derivation that follows explains this in the context of accepted mathematical model of chemotaxis network.

The strong nonlinearity in the Hill equation (5-3) and the fact that the CheA steady-state level is in the steepest portion of the curve mean that the bias B is only sensitive to changes in A near its steady state level A_∞ . In the context of adaptation, the temporal response in B is almost solely determined by A in its approach to the steady state. For example, in a chemoattractant step-up experiment, 75% of the amplitude of the adaptation response in bias B (as it increases from ~ 0 to B_∞) comes from the last $\sim 15\%$ of the amplitude of the response in A as it approaches A_∞ .

To quantify this effect, we consider the temporal response in $B(t)$ and $A(t)$ at a reference time point t_{adapt} , the adaptation time. This was defined in chapter 4 as the time elapsed between the stimulus and when the bias returned to half of its steady state value. Expanding $A(t)$ in a Taylor series about this time yields

$$A(t_{adapt}) \approx A_\infty + \left. \frac{dA}{dB} \right|_{B_\infty} (B(t_{adapt}) - B_\infty) = A_\infty - \left. \frac{dA}{dB} \right|_{B_\infty} \cdot \frac{B_\infty}{2}. \quad (5-4)$$

The second term depends inversely on the slope of the Hill function, dB/dA , which is proportional to H . Using previously determined values (121), the second term is approximately $0.25/H = 0.025 \ll A_\infty$, i.e. small when H is large. Thus, we may write $A(t) = A_\infty - \Delta A(t)$, valid for times $t \gtrsim t_{adapt}$, where ΔA is small ($\ll A_\infty$) and proportional to $1/H$.

Based on this observation, we can determine the temporal response of $A(t)$ for $t \gtrsim t_{adapt}$, i.e. how A approaches A_∞ in time. Taking equation (5-2) and Taylor expanding $F(A)$ near the steady state,

$$\frac{dm}{dt} \approx F(A_\infty) - \left. \frac{dF}{dA} \right|_{A_\infty} \Delta A(t) = - \left. \frac{dF}{dA} \right|_{A_\infty} \Delta A(t). \quad (5-5)$$

Where, by definition, $F(A_\infty) = dm/dt = 0$ at the steady state. Using the chain rule, we can further write the rate of change for CheA activity in terms of the rate of change in methylation:

$$\frac{dA}{dt} = \frac{dA}{dm} \frac{dm}{dt} = - \frac{d\Delta A}{dt}. \quad (5-6)$$

Substituting equation (5-5) into equation (5-6), we obtain

$$\frac{d\Delta A}{dt} \approx \left. \frac{dA}{dm} \frac{dF}{dA} \right|_{A_\infty} \Delta A. \quad (5-7)$$

The first factor on the right-hand side of the equation represents how CheA activity is amplified by methylation; this factor is positive, and also proportional to N , the cluster size for interacting receptors. The second factor represents how the methylation rate depends on CheA activity at the steady state; this factor is negative. These two factors combine to define the time constant with which CheA activity approaches its steady state:

$$\frac{d\Delta A}{dt} \approx - \frac{N}{T} \Delta A, \quad (5-8)$$

where we have made the dependence on cluster size N explicit. Thus, CheA approaches its steady state exponentially according to $\Delta A(t) = \Delta A_0 \exp(-Nt/T)$ (depicted in **Figure 5-2**).

Based on the above, we now use the Hill function, equation (5-3), to estimate the temporal response in bias $B(t)$, given $A(t)$ near the steady state. For our purposes, we specifically determine the rate of change in $B(t)$ at the adaptation time; this will provide an approximate measure for the *abruptness* of the adaptation response (see **Figure 5-2**), and its dependence on network parameters. Based on equations (5-4) and (5-8), the rate of change in CheA activity at the adaptation time is

$$\left. \frac{dA}{dt} \right|_{t_{adapt}} \approx \frac{N}{T} \Delta A(t_{adapt}) = \frac{N}{T} \frac{B_\infty}{2} \left. \frac{dA}{dB} \right|_{B_\infty} \propto \frac{1}{H} \frac{N}{T}, \quad (5-9)$$

proportional to $1/H$. Using the chain rule, the rate of change in $B(t)$ at the adaptation time is then

$$\left. \frac{dB}{dt} \right|_{t_{adapt}} = \left. \frac{dB}{dA} \right|_{A(t_{adapt})} \left. \frac{dA}{dt} \right|_{t_{adapt}} \propto H \cdot \frac{1}{H} \frac{N}{T} \propto \frac{N}{T}, \quad (5-10)$$

which is *independent* of H , given equation (5-9) and the fact that the slope of the Hill function dB/dA at the adaptation time is proportional to H . Thus, the abruptness in the adaptation response

for motor bias B does not depend on the sigmoidicity of the Hill function, equation (5-3), provided that H is sufficiently large. This is depicted schematically in **Figure 5-2**. While cooperativity amplifies the motor's response to changes in CheA activity (by a factor of H), it

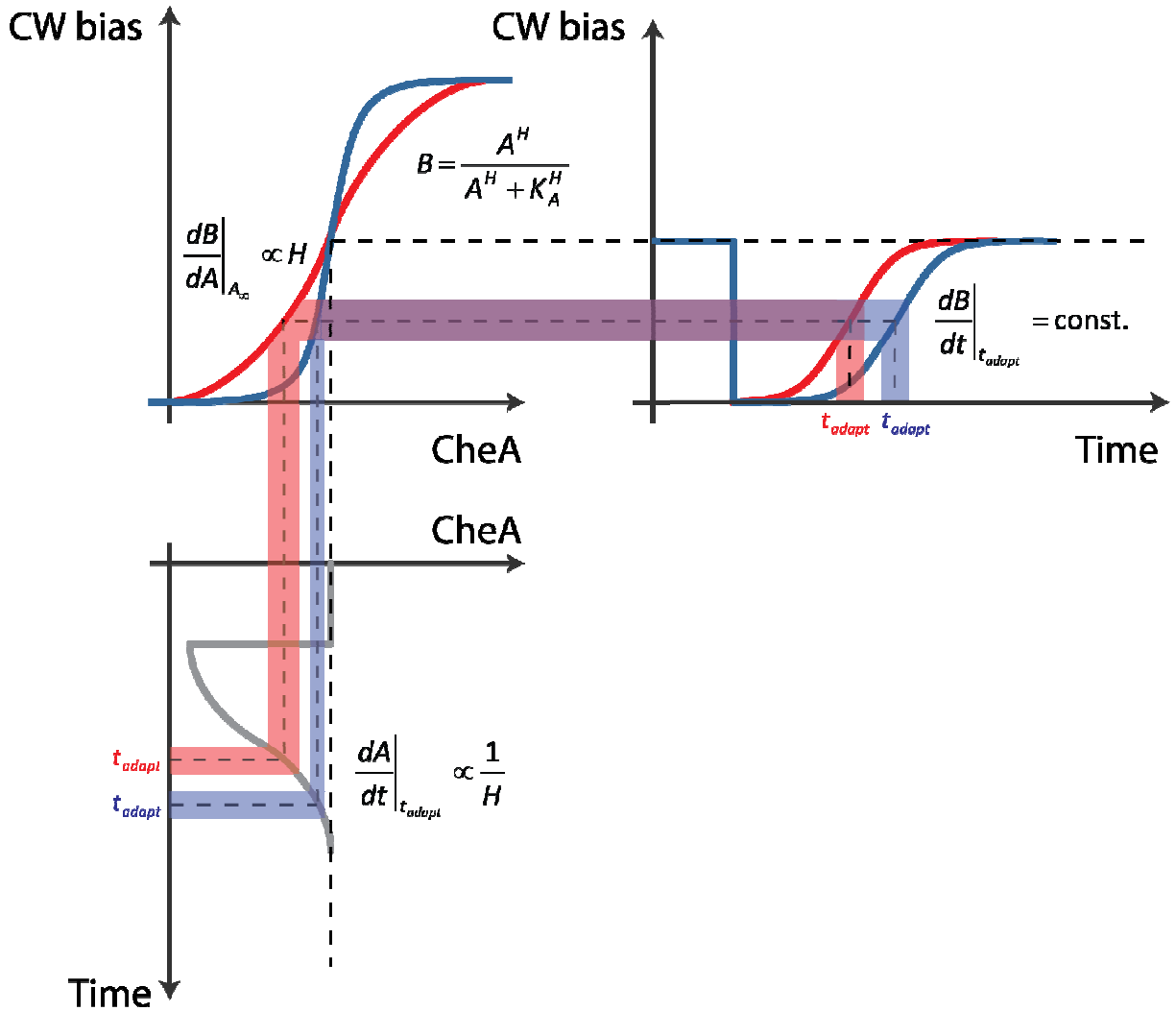


Figure 5-2. Abruptness and its dependence on cooperative switching of the flagellar motor.

The schematic describes how the time course in CheA activity during adaptation, $A(t)$, (grey trace, bottom; CheY-P level is proportional to CheA activity) is mapped into a corresponding motor bias time course, $B(t)$, (blue and red traces, right) through the sigmoidal motor bias vs. CheA activity function $B(A)$ (red and blue traces, center). Two different Hill functions are shown, with high Hill coefficient H (blue) and low H (red). At the adaptation time t_{adapt} , the high- H function amplifies changes in $A(t)$ near its steady-state where its rate of change (represented by the shaded blue area) is small. Conversely, for the low- H function, the rate of change in $A(t)$ at t_{adapt} is larger (shaded red area), but amplifies less. These compensating effects lead to a motor bias time course whose rate of change at t_{adapt} (its abruptness) is largely independent of H .

also makes the motor sensitive to small changes in CheA activity only near its steady state. As CheA activity exponentially approaches steady state during adaptation, its rate of change becomes smaller. Thus, the larger H is, the smaller the rate of change in CheA activity that engenders the motor response. These compensating effects result in a flagellar motor temporal adaptation response whose abruptness is largely independent of H (**Figure 5-2**). (Note that H does affect the adaptation time, but to a good approximation the *shape* of the response $B(t)$ remains unchanged). Importantly, however, the dependence on cluster size N remains.

5.3. Role of receptor clustering in stimulus-dependent adaptation abruptness

5.3.1. Chemoreceptors cluster at the cell poles

Instead of the strong cooperativity of the flagellar motor behavior, we believe the evidence points towards a role for strongly-interacting receptor clusters in creating the stimulus-dependent adaptation abruptness observed in our experiments. Several experiments on receptor interaction and dynamics in addition to our own numerical simulations of the chemotactic network support this view.

Clusters of chemotaxis receptors are known to be localized predominantly at the cell poles (129, 130), where the number of receptors in each cluster can range from tens to over one thousand in the case of the Tar receptor (131). As mentioned above, experimental evidence indicates that receptors interact together to amplify their effect on CheA activity in response to external chemical inputs (124).

The mathematical model for the chemotaxis network above (1, 120) further predicts that larger numbers of interacting receptors will result in a more abrupt response in CheA activity. Thus, abruptness in adaptation response likely originates from the clusters of interacting receptors that cooperatively modulate the activity of the kinase CheA. The abruptness at the level of CheA activity then propagates through the network to the level of whole-cell swimming behavior. Experimentally, CheA activity has only been measured in cell populations (14, 114, 115). We believe this may explain why abrupt adaptation kinetics in CheA has not yet been observed.

5.3.2. Chemoreceptor clustering is dynamic

Experimental evidence also indicates that receptor clustering may be dynamic; when *E. coli* and *Bacillus subtilis* cells are stimulated with saturating amounts of attractant, the polar clusters disintegrate upon stimulation and reappear after the cells have had enough time to adapt (132, 133). In another study, Borrok et al. (134) found through chemical cross-linking studies that attractants destabilize receptor clusters and repellents stabilize them. These studies support a model where the degree of chemoreceptor clustering changes dynamically depending on ligand binding.

Given that the degree of receptor clustering decreases at higher attractant concentrations, it would be expected that their cooperative effect on CheA activity—and thus the abruptness in adaptation—would decrease. We note, however, that a number of studies found that receptor methylation level increases the degree of receptor clustering and hence the response cooperativity (125). Since methylation should increase with stimulus, this would predict that abruptness would decrease with stimulus, counter to the experimentally observed trend. We speculate that methylation level is low under our experimental conditions, and that this effect may be negligible. Unfortunately, experimental estimates of the methylation level exist only for mutant strains, lacking native receptors (125). Furthermore, theoretical estimates for the parameters that determine the steady-state methylation level vary greatly between different studies (1, 120). It is also conceivable that the changes in receptor cluster size due to methylation are small compared to those produced by ligand binding. More studies are needed to quantify the importance of these competing trends.

5.3.3. Simulating the effect of chemoreceptor clustering on abruptness of adaptation

To investigate further the possible role of receptor clusters on abruptness of adaptation, we performed simulations of chemotactic adaptation generalized to allow for strongly-interacting receptor clusters of size N . All simulations were implemented in MATLAB. We followed closely the model by Tu *et al.* (120). The kinase activity of CheA, A , was determined as a function of ligand concentration ($[L]$) and methylation level (m) according to

$$A([L], m) = \frac{1}{1 + e^{N(f_L([L]) + f_m(m))}} , \quad (5-11)$$

where N is the receptor cluster size, and $f_L = \ln(1 + [L]/K_{off}) - \ln(1 + [L]/K_{on})$ and $f_m = 2(0.5 - m)$ are the free energy functions that depend only on $[L]$ and m , respectively (120). Free energies were in units of $k_B T$. Note that the value of A ranges from 0 to 1. A can be interpreted as the probability that each CheA is in its active (phosphorylating) state. K_{off} (5 μM) and K_{on} (254 μM) are ligand binding constants for receptors associated with CheA in inactive and active states, respectively. The values for K_{off} and K_{on} were obtained from fitting the expression for f_L to our adaptation time data (**Figure 4-4b**). The exact values of K_{off} and K_{on} affect only the adaptation time and not the abruptness of adaptation.

At each time step ($\Delta t = 0.01$ sec, chosen to match the data rate. Using smaller time steps did not change the results of simulations), the average methylation level of the receptor-CheA complex was adjusted according to

$$\frac{dm}{dt} = V_R(1 - A) - V_B(A). \quad (5-12)$$

V_R (0.01 s^{-1}) and V_B (0.02 s^{-1}) are methylation and demethylation rates, respectively (135). As with K_{off} and K_{on} , the exact values of V_R and V_B only affect the adaptation time. The CheA activity, A , was then converted to the flagellar motor bias, B , via a highly cooperative relation

$$B = \frac{A^H}{A^H + K_A^H} \quad (5-3)$$

(121). Note that as with A , B ranges from 0 to 1. K_A is the value of A at which B is 1/2. Although technically B is a function of CheY-P concentration and not CheA activity, it is commonly assumed that they are proportional since CheY-P levels equilibrate faster than other processes (14).

Since a general model on how the motor bias gets converted to the cell's tumble bias is lacking, we assumed they are proportional. At the first time point, every simulated cell started from the tumble state. At each subsequent time point, the cell had a constant probability of switching to the run state. When the cell was in the run state, on the other hand, its probability of switching to the tumble state depended on the tumble bias. As a result, the average tumble duration did not depend on tumble bias but the average run duration depended on it. This was

consistent with a previous study and our own data (34). For each combination of N and H values, 100 run-tumble binary time traces were generated. The simulated traces were analyzed in the same way as the experimental data as described above.

Numerically solving the response to step up and step down in attractant concentration, we found that the simulated ETAs vary inversely with cluster size N (**Figure 5-3a**). Specifically, the experimentally observed stimulus-dependent abruptness (**Figure 4-7e**) can be reproduced by assuming that N varies between ~ 18 and ~ 3 , decreasing with stimulus strength (**Figure 5-3b**). This range of values is consistent with numbers cited in the literature for wild-type (14, 125, 136) and mutant strains (125) and follows the expected trend with stimulus level. Thus, our simulations support the notion of dynamic receptor clustering as the source for adaptation abruptness and stimulus dependence. We also note that simulations corroborate our view that ETA is unaffected by the cooperativity H exhibited by CheY-P (**Figure 5-3a**, inset).

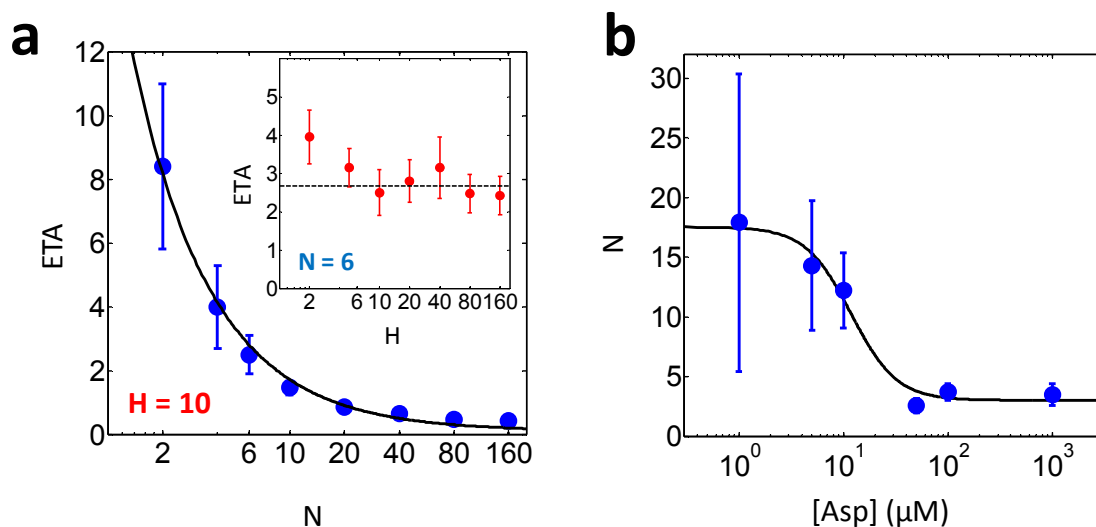


Figure 5-3. Stimulus-dependent receptor clustering can explain the observed abruptness of adaptation. (a) The number of events to adaptation (ETA) as a function of the receptor cluster size N . Chemotactic response of individual cells to a 100 μM step up in L-aspartate concentration was simulated by numerically solving a stochastic model of the chemotaxis response, and the mean ETA was obtained by fitting exponential functions to the histogram of individual ETA values from 100 cells. Errorbars denote the fitting uncertainty. The cooperativity of the flagellar motor switching behavior, H , was set at 10. Black lines is a model fit in the form of $a/N + b$. Inset: The effect of varying H on ETA. The receptor cluster size, N , was set at 6. (b) The estimated receptor cluster size N as a function of the step-up stimulus. N was estimated from the experimentally measured ETA values (**Figure 4-7e**), using the theoretical relation between ETA and N (panel b). Errorbars designate the experimental standard error.

5.3.4. Fluctuations alone cannot cause abrupt adaptation

Cellular parameters such as CheA activity are subject to temporal fluctuations, due to thermal noise and the small number of protein molecules involved in the signaling network (2). To investigate the effect of noise on the abruptness of adaptation, we incorporated noise into the CheA activity in our simulations using the linear noise approximation scheme (114, 137). In this approximation, CheA activity is perturbed from its steady-state by a white noise source, η , and returns to steady-state with a relaxation time τ_a , such that $d\Delta A(t)/dt = -\Delta A(t)/\tau_a + \sigma\eta(t)$. Here, ΔA is the deviation of CheA activity from its steady-state and σ is the noise strength. In our simulations, we used $\tau_a = 29$ sec (114) and σ was varied from 10% to 40% of CheA activity (*Figure 5-4*).

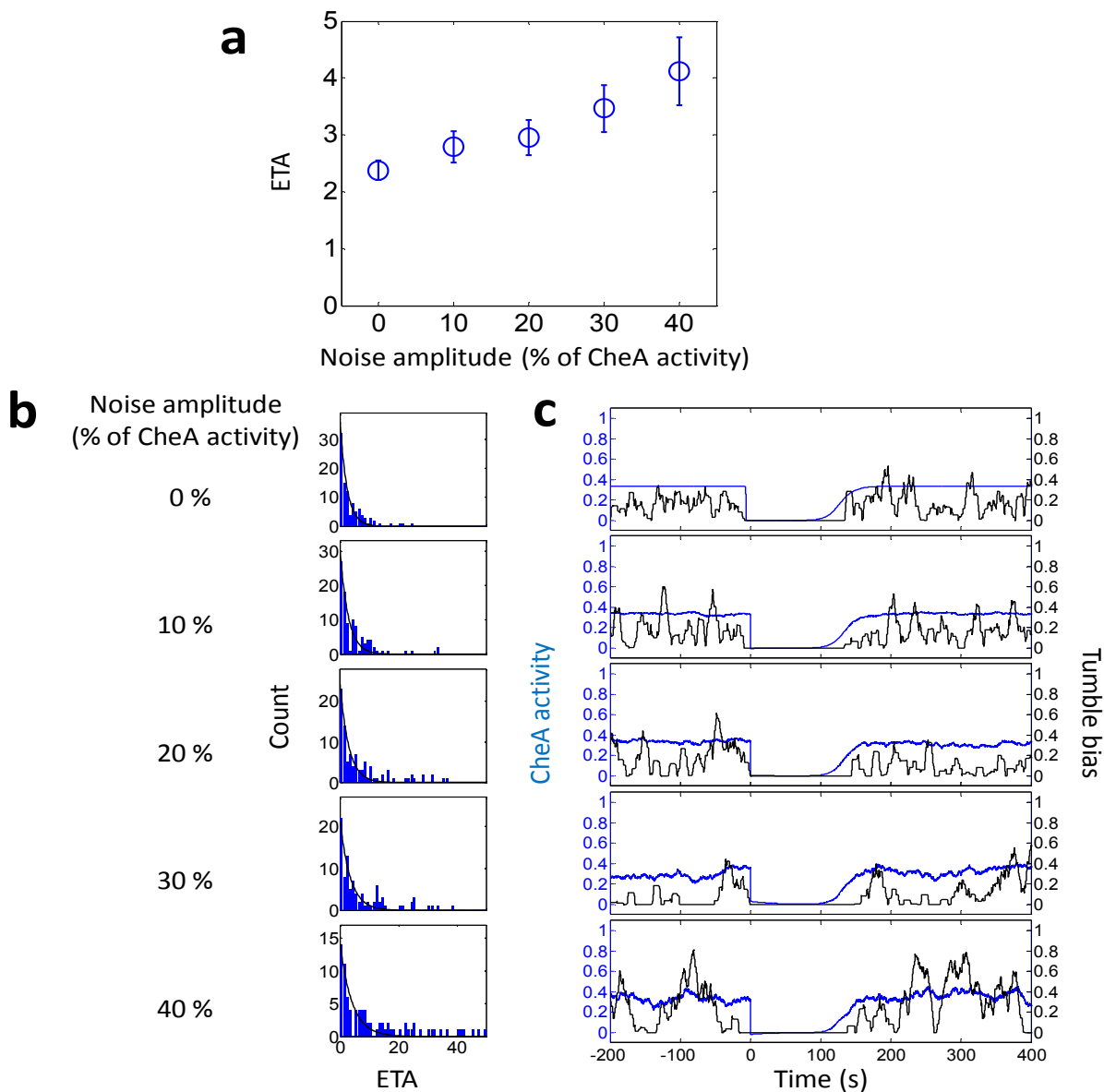


Figure 5-4. Simulated effect of noise on adaptation abruptness. (a) The average number of events to adaptation (ETA) as a function of the CheA noise amplitude. The mean ETA was obtained by fitting exponential functions to the histogram of individual ETA values from 100 cells. Errorbars denote the fitting uncertainties. The receptor cluster size, N , was set at 6, and the cooperativity of the flagellar motor switching behavior, H , was set at 10. The exact value of stimulus strength does not change results of the simulation. (b) Histograms of individual ETA values from 100 simulated cells. Black lines are exponential fits. (c) Example simulated time traces of CheA activity (blue) and tumble bias (black) at each noise amplitude.

Chapter 6. Summary and outlook

6.1. Studying *E. coli* chemotaxis using optical traps

In the past several decades, *E. coli* chemotaxis has been studied using various methods including tracking of swimming cells, tethering flagella to a surface or a bead, and measuring the FRET (Förster Resonance Energy Transfer) signal from protein-protein interaction. Of these, the tethering method allowed long-term measurements of single-cell behavior. However, the results from tethering studies had limited implications to the physiologically-relevant swimming behavior, since multiple flagella on a given cell show limited synchrony. Multiple flagella on a given cell showed limited synchrony.

In this work we have developed a novel method for studying long-term swimming behavior of individual *E. coli* cells using optical traps. Use of oxygen scavenging enzymes prevented cell damage, whereas back focal plane detection method enabled high speed data acquisition of the sub-micron swimming motion. Automated data analysis routine using continuous wavelet transform facilitated analysis of higher-order swimming features such as direction reversal and multiple swimming speeds. Interestingly, we observed run durations in swimming cells to be exponentially distributed with a heavy tail, in a manner similar to the distribution of counter-clockwise duration in single flagella. Tumble durations were distributed exponentially, also similarly to the clockwise durations in single flagella.

We have also studied the chemotactic adaptation behavior in single *E. coli* cells. We applied step-up and step-down chemical stimuli by moving trapped cells along the chemical concentration gradient created in a laminar flow chamber. At the population average level, the adaptation behavior of trapped cells reproduced existing results. However, when we analyzed the adaptation behavior at the single cell level, we observed two striking features: 1) Individual cells showed *abrupt* adaptation, often returning to the pre-stimulus behavior after a single prolonged run; and 2) Individual cells showed adaptation overshoot, with their tumble bias exhibiting excessive response before the return to pre-stimulus behavior. Furthermore, these two features of adaptation showed dependence on stimulus strength, and asymmetry between step-up and step-down adaptation.

6.2. Outstanding questions

The molecular mechanism responsible for the abrupt adaptation is not known, although we believe the evidence points towards a role for strongly-interacting receptor clusters. Chemotaxis receptors are known to be localized predominantly at the cell poles (129, 130), where their number can range from tens to over one thousand in the case of the Tar receptor (which binds L-aspartate) (131). It is known that receptors interact together to amplify their effect on CheA activity in response to external chemical inputs (124). Theoretical models (1, 120) further predict that larger numbers of interacting receptors will result in a more abrupt response.

For the mechanism responsible for adaptation overshoot, a recent theoretical model (118) postulates that the overshoot response is caused by the difference in methylation kinetics between different types of receptors. In this model, two major receptor types, Tar (aspartate receptor) and Tsr (serine receptor), exhibit “crosstalk”: Tsr receptors respond (albeit weakly) to L-aspartate and Tar receptors to L-serine. Furthermore, the two receptor types exhibit different methylation kinetics depending on whether they are bound to the type-specific ligand or not. Overshoot is thus predicted to occur when Tsr receptors show transient methylation in response to L-aspartate stimuli (118).

6.3. Receptor expression and its effect on adaptation abruptness

To establish a direct link between receptor cluster size and adaptation abruptness, we plan to manipulate experimentally the cluster size by varying receptor expression. Past studies have found the cluster size to depend on the receptor expression level (124, 125, 138, 139) and the degree of receptor methylation (125). We have a mutant strain (UU2612-pLC113, gift of John Parkinson, University of Utah (140, 141)) lacking endogenous receptors, but in which Tar receptors can be expressed under the tight control of an inducible promoter. This strain will allow us to vary the receptor cluster size in a controlled manner (124, 138, 139). Our plan is to repeat our single-cell adaptation measurements with this mutant strain at varying receptor expression levels. If our model is correct, we expect that, compared to wild-type cells, mutant cells in which Tar receptor is overexpressed will exhibit abrupt adaptation kinetics (i.e. $ETA \sim 1$) across the full range of stimulus strengths. In contrast, cells that underexpress these receptors relative to wild-type should exhibit more gradual adaptation time traces ($ETA \geq 5$).

Studies (124, 138) suggest that while modest increases in receptor expression level do not damage chemotactic response, disproportionately high amounts of receptors relative to CheA and CheW lead to formation of dysfunctional receptor arrays. Therefore we need to take caution when varying the expression level of Tar. When exploring disproportionately high amounts of Tar relative to the native expression of CheA and CheW, we will concurrently increase the expression levels of CheA and CheW from a separate plasmid (138). Chemotactic ability of cells expressing various amounts of Tar, CheA, and CheW will be verified using the standard swarm plate assay (142). As an alternative strategy for varying receptor levels (and therefore cluster size), we can use the fact that *E. coli* express different levels of chemotaxis proteins (including receptors, CheA, and CheW) in different growth media (118).

6.4. Receptor dynamics during the chemotactic response

Although the proposed experiments above will establish a link between receptor clustering and adaptation kinetics, they do not explain why we observed changes in abruptness with stimulus strength. What makes the abruptness stimulus-dependent? Experimental evidence indicates that receptor clustering may be *dynamic*; when *E. coli* and *Bacillus subtilis* cells are stimulated with saturating amounts of attractant, the polar clusters disintegrate upon stimulation and reappear after the cells have had enough time to adapt (132, 133). A previous study (134) using chemical cross-linking found that attractants destabilize receptor clusters and repellents stabilize them. In addition, a number of studies found methylation to stabilize receptor clustering and increase response cooperativity (125, 143). Taken together, these studies support a model where the degree of chemoreceptor clustering changes dynamically depending on ligand binding and methylation. Thus, a mechanism where the functional size of receptor clusters tends to be smaller at saturating ligand concentrations can explain our observations. In our simulations, we found an inverse relation between cluster size and ETA. To best fit our observed increase in ETA with increasing stimulus strength, N decreased from ~ 18 to ~ 3 (**Figure 5-3b**), following the expected trend. Thus, our simulations support the notion of dynamic receptor clustering as the source for adaptation abruptness and stimulus dependence.

To test this hypothesis, we propose to visualize the receptor localization in individual cells while tracking their chemotactic response simultaneously. To this end, we will use a strain expressing a fusion of Tar receptor to YFP (yellow fluorescent protein) (144). Though not fully

functional, the Tar-YFP fusion clusters with the endogenous, functional receptors and thus serves to detect cluster localization (145). In *B. subtilis*, receptor cluster localization of fluorescently-labeled receptors has been observed to change *in vivo* (133).

Once disrupted upon stimulation, polar localization is observed to return in adapted cells (132, 133). However the relative timing of receptor cluster reorganization and behavioral adaptation is unknown due to the limited time resolution of the available methods (132, 133). By following the pattern of receptor localization at various stages of chemotactic adaptation, we will be able to measure directly receptor dynamics with abruptness of adaptation.

Cells adapting from a step-up in attractant gradually increase their receptor methylation, reaching a steady-state level that depends on ligand concentration. Interestingly, highly methylated receptors have been found to form larger clusters (125). This appears to conflict with our observed trend, in that cells stimulated with a large step-up would be expected to have *highly* methylated receptors, *large* receptor clusters, and thus *abrupt* adaptation kinetics. Therefore, following the time course of receptor localization throughout the entire adaptation process will be crucial in distinguishing the effects due to ligand binding and methylation. Our imaging will allow us to see whether the changes in receptor cluster size occur simultaneously with ligand binding and methylation (as evidenced by adaptation), or if there is a time lag between the stimulus and clustering. If there is no time lag, our data suggests that effects produced by ligand binding overwhelm those by methylation. If there is a time lag, it would mean that return of polar clustering upon adaptation by methylation simply occurs too late to influence the adaptation abruptness.

6.5. Cross talk between receptors for different ligands and its effect on the adaptive overshoot

Since the proposed mechanism for adaptation overshoot relies on crosstalk between Tar and Tsr receptors, it should be possible to abolish this feature by removing all receptors of one kind. We will test this potential mechanism by performing single-cell chemotaxis experiments using strains that express Tar or Tsr only. We have obtained such strains (UU2612-pLC113 or UU2612-pPA114, respectively; gift of John Parkinson, University of Utah (140, 141)). We will test each with our trapping assay under a range of stimulus conditions and compare single-cell adaptation responses to wild-type.

Cells expressing Tar only have been shown to display different sensitivity to L-aspartate compared to wildtype cells (124). Since we observe a stimulus-dependent overshoot response to step-up attractant stimuli, we may need to compensate for the shift in chemotactic sensitivity when comparing the overshoot responses in Tar-only cells and wildtype cells. We will obtain the adaptation time dose-response curve in Tar-only cells, and quantify the shift in sensitivity.

Appendix A. Strains, growth media, and trapping media

A.1. Strains

The genotypes and sources of all *E. coli* strains used in this study are given in **Table A1**. RP437 is wild type for chemotaxis (103). CR20 and CR33 are “runner” (run only) and “tumbler” (no runs) mutants, due to *cheY* and *cheZ* deletions, respectively. PS2001 is a strain where environmental signals are decoupled from the behavior of flagellar motors (2, 34). Tumbling bias in this strain can be adjusted by expressing CheYD13K (106) from a plasmid (pMS164), under an inducible promoter. As opposed to the wild-type CheY, CheYD13K does not require phosphorylation to be active (2). Thus, all CheYD13K proteins expressed in the cell are able to bias flagellar motors for longer clockwise rotation. Clockwise rotation of flagellar motors tends to cause the swimming cell to tumble (104).

A.2. Growth media and conditions

E. coli cells were harvested from a single colony on an agar plate and grown overnight in 1 ml tryptone broth (1% Bacto tryptone, 0.8% NaCl) (146). The overnight culture was diluted 100-fold into 1 ml tryptone broth in a 14-ml round bottom Falcon tube and grown for 4.5 hours to mid-log phase ($OD_{600} \sim 0.5$). The PS2001-pMS164 strain was grown with antibiotics chloramphenicol (34 $\mu\text{g/ml}$), kanamycin (40 $\mu\text{g/ml}$), and various levels (1-100 μM) of the inducer isopropyl- β -D-galactopyranoside (IPTG) (34). All bacterial growth in this study was done at 30°C with 265 rpm rotation (60). Cells were washed from growth medium by centrifugation (2,000 g, 10 min) followed by gentle resuspension in trapping medium. Resuspension by pipetting was minimized, as it can cause the flagella to break due to shear forces.

A.3. Solutions used in trapping experiments

A.3.1. Trapping medium

Trapping medium contained tryptone broth (TB) supplemented with 2% glucose, 100 mM Tris-Cl (pH7.5), and an oxygen scavenging system (20 $\mu\text{g/ml}$ glucose oxidase and 4 $\mu\text{g/ml}$ catalase, Sigma; adapted from (147)) in order to reduce trap-mediated oxidative damage to the cells. The oxygen scavenging system was added 2 hours before use in order to reach a steady oxygen level. Resazurin (Sigma) was added (0.0001%) as an oxygen indicator. Glucose acts as a

substrate for the oxygen scavenging system and provides energy for the cells swimming in anaerobic condition (148). Tryptone broth is an appropriate growth medium for obtaining reproducible cell motility (149). However, it is not suitable for chemotaxis studies, since it contains amino acids that can act as chemoattractants.

We also examined cell behavior in a “motility buffer” containing 70 mM NaCl (3), supplemented by 100 mM Tris-Cl, 2% glucose and the oxygen scavenging system. As shown in **Table A2**, trapped cells under these conditions display the same behavior as those described in the main text: they remain motile for long durations, exhibit similar flagellar and body rotation rates, and tumble at similar frequencies. A high buffering capacity is necessary to prevent acidification of the medium by gluconic acid, a side product of the oxygen scavenging reactions (150). Though a 100 mM Tris-Cl buffer is preferable for long-term stability of our trapping medium, a lower molarity is acceptable for shorter time periods (~1 hr) if ionic strength is a concern. Cells resuspended in a buffer containing 70 mM NaCl, 10 mM Tris-Cl, 2% glucose and the oxygen scavenging system are well-behaved in our trap, as shown in **Table A2**.

A.3.2. Trap motility buffer

Trap motility buffer (TMB) contained 70 mM NaCl, 0.1 mM methionine, 100 mM Tris-Cl, 2% (wt/vol) glucose, and an oxygen scavenging system (80 $\mu\text{g ml}^{-1}$ glucose oxidase and 13 $\mu\text{g ml}^{-1}$ catalase; EMD Chemicals 345386 and 219001, respectively) to reduce oxidative damage to the cells by the infrared trapping light (28, 93). The oxygen scavenging system was added immediately before the beginning of the experiment. Methionine provides the methyl groups necessary for chemotactic adaptation to occur (29). Glucose acts as a substrate for the oxygen scavenging system and provides energy for cell swimming under anaerobic condition (148). Various concentrations of L-aspartate (1-1000 μM) were added as a chemical stimulus.

Table A1: Strains and plasmid used

Strain	Genotype	Comments	Source
RP437	<i>(F- thi thr leu his met eda rpsL)</i>	Wild type for chemotaxis	Parkinson and Houts (1982) (103) Rao lab stocks
CR20	RP437 <i>(cheY::FRT)</i>	“runner” mutant	This study
CR33	RP437 <i>(cheZ::cm)</i>	“tumbler” mutant	This study
PS2001	<i>ΔcheBcheYcheZ</i>	Contains the plasmid pMS164 for adjustable tumble bias	Alon et al. (1998) (34) Gift of Philippe Cluzel
Plasmid			
pMS164	Low copy, <i>cheYD13K</i> under <i>lac</i> promoter, Cm ^R	Expresses constitutively active mutant version of CheY	Alon et.al. (1998) (34) Gift of Philippe Cluzel

Table A2: Comparison of trapping media

Buffer	Contents	Body roll rate Ω (Hz)	Flagella rotation rate ω (Hz)	Tumble frequency (Hz)
Trapping medium	TB, 100 mM Tris, 2% glucose, oxygen scavenging system	11.4 ± 0.5 (mean±s.e .m., N=43)	86.1 ± 1.7	0.22 ± 0.02
High ionic-strength motility buffer	70 mM NaCl, 100 mM Tris, 2% glucose, oxygen scavenging system	7.0 ± 1.1 (mean±s.e .m., N=8)	80.5 ± 3.8	0.23 ± 0.03
Low ionic-strength motility buffer	70 mM NaCl, 10 mM Tris, 2% glucose, oxygen scavenging system	9.1 ± 1.1 (mean±s.e .m., N=7)	72.9 ± 1.7	0.25 ± 0.02

Appendix B. Detailed Description of Experimental Protocols

B.1. Flagella labeling protocol

Wild-type cells were labeled with Cy3 monofunctional NHS ester (GE Healthcare) following a previously reported protocol (27). Cells were grown to mid-log phase in tryptone broth and washed twice (1000 g, 10 min) with the final resuspension concentrating cells 20-fold in a buffer containing 10 mM KPO₄ (pH 7.0), 70 mM NaCl and 0.1 mM EDTA. Cy3 dye suspended in 25 μ l of 1 M NaHCO₃ was added to 500 μ l of the culture. The labeling reaction was incubated with slow rotation (~10 rpm) at room temperature in the dark for 90 minutes. The labeled culture was washed once and diluted 100-fold in 1 ml of modified trapping medium. The modified trapping medium contained 50 mM ascorbic acid (Sigma) in place of the oxygen scavenging system. Ascorbic acid is known to quench oxygen radicals and reduce photobleaching (151).

B.2. 2-D assay protocol

B.2.1. Construction of the 2-D chamber

A small drop (~5 μ l) of trapping medium containing *E. coli* cells at OD₆₀₀ ~0.1 was placed on a coverlip (Fisher, No. 1.5) and spread evenly by gently covering with a 22 mm x 22 mm coverslip (Fisher, No. 1) from the top (34). Care was taken to prevent formation of air bubbles. Coverslips were used directly out of the box (4). To prevent drift due to evaporation, open sides were sealed with molten wax. 2-D swimming of *E. coli* cells confined in the resulting ~10 μ m-thick fluid chamber was observed in phase contrast with a 10X objective (Nikon Eclipse TE2000-E). 30-second video images were taken at 30 frames per second at various locations on each slide (34).

B.2.2. Analysis of the 2-D swimming track data

The field of view of video images was 512 x 512 pixels, covering approximately 320 μ m x 320 μ m. Images were analyzed using a custom routine written in Matlab, loosely based on previously reported algorithms (34, 152). Images were adjusted for contrast, and a threshold was applied to discriminate cells as black objects against a white background. Contiguous black objects between 3-30 pixels in size were identified as cells, and their centroid and long-axis orientation were determined. Trajectories connecting the cell positions in successive image frames were tracked by matching each cell with one cell in the next frame that was within 5

pixels. A trajectory was terminated if there were no cells or multiple cells connected in the next frame. Trajectories shorter than 3 μm in contour length or 1.33 s in duration were discarded. The remaining trajectories were filtered using a modified median filter following Alon *et al.* (34). The filtered trajectories were then analyzed to determine run-tumble statistics, distributions of angle changes, run speed, and other parameters of potential interest. Of particular interest were run and tumble durations. Tumbles were identified by setting thresholds in both linear velocity and angular velocities. First, the “average speed” of a cell was defined by sorting the linear velocity values for each cell, excluding the top and bottom 10%, and taking the mean of the remaining velocities. The tumble threshold was then defined as any drop in linear velocity below half the “average speed” of the cell, and an increase in angular velocity to three times the average angular velocity (similar to the algorithm used in Amsler (152)). The end of each tumble was determined by comparing the speed after a tumble to the "running speed", which was defined as the mean of the fastest 10% of speeds in a trajectory (34). After initiation of a tumble a standard student's t-test was applied to compare a moving 3-point window of speeds to the running speed. When the t-test had a p-value higher than 0.05, the ends of tumbles were scored.

References

1. Keymer JE, Endres RG, Skoge M, Meir Y, & Wingreen NS (2006) Chemosensing in *Escherichia coli*: two regimes of two-state receptors. *Proc Natl Acad Sci U S A* 103(6):1786-1791.
2. Korobkova E, Emonet T, Vilar JMG, Shimizu TS, & Cluzel P (2004) From molecular noise to behavioural variability in a single bacterium. *Nature* 428(6982):574-578.
3. Darnton NC, Turner L, Rojevsky S, & Berg HC (2007) On torque and tumbling in swimming *Escherichia coli*. *Journal of Bacteriology* 189(5):1756-1764.
4. Turner L, Ryu WS, & Berg HC (2000) Real-time imaging of fluorescent flagellar filaments. *Journal of Bacteriology* 182(10):2793-2801.
5. Berg HC & Brown DA (1972) Chemotaxis in *Escherichia coli* analysed by three-dimensional tracking. *Nature* 239(5374):500-504.
6. Paster E & Ryu WS (2008) The thermal impulse response of *Escherichia coli*. *Proc Natl Acad Sci U S A* 105(14):5373-5377.
7. Li C & Adler J (1993) *Escherichia coli* shows two types of behavioral responses to osmotic upshift. *J Bacteriol* 175(9):2564-2567.
8. Wright S, Walia B, Parkinson JS, & Khan S (2006) Differential activation of *Escherichia coli* chemoreceptors by blue-light stimuli. *J Bacteriol* 188(11):3962-3971.
9. Khan S, *et al.* (1993) Excitatory signaling in bacterial probed by caged chemoeffectors. *Biophys J* 65(6):2368-2382.
10. Burret RB & Stock AM (2002) Molecular information processing: lessons from bacterial chemotaxis. *J Biol Chem* 277(12):9625-9628.
11. Szurmant H & Ordal GW (2004) Diversity in chemotaxis mechanisms among the bacteria and archaea. *Microbiol Mol Biol Rev* 68(2):301-319.
12. Mao H, Cremer PS, & Manson MD (2003) A sensitive, versatile microfluidic assay for bacterial chemotaxis. *Proc Natl Acad Sci U S A* 100(9):5449-5454.
13. Segall JE, Block SM, & Berg HC (1986) Temporal comparisons in bacterial chemotaxis. *Proc Natl Acad Sci U S A* 83(23):8987-8991.
14. Sourjik V & Berg HC (2002) Receptor sensitivity in bacterial chemotaxis. *Proc Natl Acad Sci U S A* 99(1):123-127.
15. Mesibov R & Adler J (1972) Chemotaxis toward amino acids in *Escherichia coli*. *J Bacteriol* 112(1):315-326.
16. Alon U, Surette MG, Barkai N, & Leibler S (1999) Robustness in bacterial chemotaxis. *Nature* 397(6715):168-171.
17. Berg HC (1993) *Random walks in biology* (Princeton University Press, Princeton, N.J.) Expanded Ed p 152 p.
18. Dusenbery DB (1997) Minimum size limit for useful locomotion by free-swimming microbes. *Proc Natl Acad Sci U S A* 94(20):10949-10954.
19. Jones GW, Richardson LA, & Uhlman D (1981) The invasion of HeLa cells by *Salmonella typhimurium*: reversible and irreversible bacterial attachment and the role of bacterial motility. *J Gen Microbiol* 127(2):351-360.
20. Lane MC, Alteri CJ, Smith SN, & Mobley HL (2007) Expression of flagella is coincident with uropathogenic *Escherichia coli* ascension to the upper urinary tract. *Proc Natl Acad Sci U S A* 104(42):16669-16674.

21. Celli JP, *et al.* (2009) Helicobacter pylori moves through mucus by reducing mucin viscoelasticity. *Proc Natl Acad Sci U S A* 106(34):14321-14326.
22. Ottemann KM & Lowenthal AC (2002) Helicobacter pylori uses motility for initial colonization and to attain robust infection. *Infect Immun* 70(4):1984-1990.
23. Baker MD, Wolanin PM, & Stock JB (2006) Signal transduction in bacterial chemotaxis. *Bioessays* 28(1):9-22.
24. Wadhams GH & Armitage JP (2004) Making sense of it all: bacterial chemotaxis. *Nat Rev Mol Cell Biol* 5(12):1024-1037.
25. Berg HC (2003) The rotary motor of bacterial flagella. *Annu Rev Biochem* 72:19-54.
26. Turner L, Ryu WS, & Berg HC (2000) Real-time imaging of fluorescent flagellar filaments. *J Bacteriol* 182(10):2793-2801.
27. Darnton NC, Turner L, Rojevsky S, & Berg HC (2007) On torque and tumbling in swimming Escherichia coli. *J Bacteriol* 189(5):1756-1764.
28. Min TL, *et al.* (2009) High-resolution, long-term characterization of bacterial motility using optical tweezers. *Nat Methods* 6(11):831-835.
29. Alon U, Surette MG, Barkai N, & Leibler S (1999) Robustness in bacterial chemotaxis. *Nature* 397(6715):168-171.
30. Park H, *et al.* (2010) Interdependence of behavioural variability and response to small stimuli in bacteria. *Nature* 468(7325):819-823.
31. Barkai N & Leibler S (1997) Robustness in simple biochemical networks. *Nature* 387(6636):913-917.
32. Cluzel P, Surette M, & Leibler S (2000) An ultrasensitive bacterial motor revealed by monitoring signaling proteins in single cells. *Science* 287(5458):1652-1655.
33. Scharf BE, Fahrner KA, Turner L, & Berg HC (1998) Control of direction of flagellar rotation in bacterial chemotaxis. *Proc Natl Acad Sci U S A* 95(1):201-206.
34. Alon U, *et al.* (1998) Response regulator output in bacterial chemotaxis. *EMBO J* 17(15):4238-4248.
35. Lidstrom ME & Konopka MC (2010) The role of physiological heterogeneity in microbial population behavior. *Nat Chem Biol* 6(10):705-712.
36. Davidson CJ & Surette MG (2008) Individuality in bacteria. *Annu Rev Genet* 42:253-268.
37. Kiefer JC (2007) Epigenetics in development. *Dev Dyn* 236(4):1144-1156.
38. Davies J & Davies D (Origins and evolution of antibiotic resistance. *Microbiol Mol Biol Rev* 74(3):417-433.
39. Bigger WB (1944) Treatment of staphylococcal infections with penicillin by intermittent sterilization. *Lancet* 2:497-500.
40. Balaban NQ, Merrin J, Chait R, Kowalik L, & Leibler S (2004) Bacterial persistence as a phenotypic switch. *Science* 305(5690):1622-1625.
41. Novick A & Weiner M (1957) Enzyme Induction as an All-or-None Phenomenon. *Proc Natl Acad Sci U S A* 43(7):553-566.
42. Ozbudak EM, Thattai M, Lim HN, Shraiman BI, & Van Oudenaarden A (2004) Multistability in the lactose utilization network of Escherichia coli. *Nature* 427(6976):737-740.
43. Spudich JL & Koshland DE, Jr. (1976) Non-genetic individuality: chance in the single cell. *Nature* 262(5568):467-471.
44. Paulsson J (2004) Summing up the noise in gene networks. *Nature* 427(6973):415-418.

45. Raj A & van Oudenaarden A (2008) Nature, nurture, or chance: stochastic gene expression and its consequences. *Cell* 135(2):216-226.
46. Korobkova E, Emonet T, Vilar JM, Shimizu TS, & Cluzel P (2004) From molecular noise to behavioural variability in a single bacterium. *Nature* 428(6982):574-578.
47. Block SM, Segall JE, & Berg HC (1982) Impulse responses in bacterial chemotaxis. *Cell* 31(1):215-226.
48. Matthaus F, Jagodic M, & Dobnikar J (2009) E. coli superdiffusion and chemotaxis-search strategy, precision, and motility. *Biophys J* 97(4):946-957.
49. Tu Y & Grinstein G (2005) How white noise generates power-law switching in bacterial flagellar motors. *Phys Rev Lett* 94(20):208101.
50. Matthaus F, Jagodic M, & Dobnikar J (2009) E. coli Superdiffusion and Chemotaxis-Search Strategy, Precision, and Motility. *Biophysical Journal* 97(4):946-957.
51. Stocker R, Seymour JR, Samadani A, Hunt DE, & Polz MF (2008) Rapid chemotactic response enables marine bacteria to exploit ephemeral microscale nutrient patches. *Proceedings of the National Academy of Sciences of the United States of America* 105(11):4209-4214.
52. Block SM, Segall JE, & Berg HC (1983) Adaptation Kinetics in Bacterial Chemotaxis. *Journal of Bacteriology* 154(1):312-323.
53. Brown DA & Berg HC (1974) Temporal stimulation of chemotaxis in Escherichia coli. *Proc Natl Acad Sci U S A* 71(4):1388-1392.
54. Khan S, Amoyaw K, Spudich JL, Reid GP, & Trentham DR (1992) Bacterial chemoreceptor signaling probed by flash photorelease of a caged serine. *Biophys J* 62(1):67-68.
55. Khan S, *et al.* (1993) Excitatory Signaling in Bacteria Probed by Caged Chemoeffectors. *Biophysical Journal* 65(6):2368-2382.
56. Jasuja R, Keyoung J, Reid GP, Trentham DR, & Khan S (1999) Chemotactic responses of Escherichia coli to small jumps of photoreleased L-aspartate. *Biophys J* 76(3):1706-1719.
57. Block SM, Segall JE, & Berg HC (1982) Impulse Responses in Bacterial Chemotaxis. *Cell* 31(1):215-226.
58. Sager BM, Sekelsky JJ, Matsumura P, & Adler J (1988) Use of a computer to assay motility in bacteria. *Anal Biochem* 173(2):271-277.
59. Shi W, Li C, Louise CJ, & Adler J (1993) Mechanism of adverse conditions causing lack of flagella in Escherichia coli. *J Bacteriol* 175(8):2236-2240.
60. Staropoli JF & Alon U (2000) Computerized analysis of chemotaxis at different stages of bacterial growth. *Biophysical Journal* 78(1):513-519.
61. Silverman M & Simon M (1974) Flagellar rotation and the mechanism of bacterial motility. *Nature* 249(452):73-74.
62. Sowa Y, *et al.* (2005) Direct observation of steps in rotation of the bacterial flagellar motor. *Nature* 437(7060):916-919.
63. Berg HC & Brown DA (1972) Chemotaxis in Escherichia-Coli Analyzed by 3-Dimensional Tracking. *Nature* 239(5374):500-&.
64. Berg HC & Purcell EM (1977) Physics of chemoreception. *Biophys J* 20(2):193-219.
65. Frymier PD, Ford RM, Berg HC, & Cummings PT (1995) Three-dimensional tracking of motile bacteria near a solid planar surface. *Proc Natl Acad Sci U S A* 92(13):6195-6199.

66. Vigeant MA & Ford RM (1997) Interactions between motile Escherichia coli and glass in media with various ionic strengths, as observed with a three-dimensional-tracking microscope. *Appl Environ Microbiol* 63(9):3474-3479.
67. Ishihara A, Segall JE, Block SM, & Berg HC (1983) Coordination of Flagella on Filamentous Cells of Escherichia-Coli. *Journal of Bacteriology* 155(1):228-237.
68. Macnab RM & Han DP (1983) Asynchronous Switching of Flagellar Motors on a Single Bacterial-Cell. *Cell* 32(1):109-117.
69. Ashkin A, Dziedzic JM, Bjorkholm JE, & Chu S (1986) Observation of a single-beam gradient force optical trap for dielectric particles. *Opt Lett* 11(5):288.
70. Neuman KC & Block SM (2004) Optical trapping. *Rev Sci Instrum* 75(9):2787-2809.
71. Tolic-Norrelykke SF, *et al.* (2006) Calibration of optical tweezers with positional detection in the back focal plane. *Review of Scientific Instruments* 77(10).
72. Gittes F & Schmidt CF (1998) Interference model for back-focal-plane displacement detection in optical tweezers. *Opt Lett* 23(1):7-9.
73. Moffitt JR, Chemla YR, Izhaky D, & Bustamante C (2006) Differential detection of dual traps improves the spatial resolution of optical tweezers. *Proceedings of the National Academy of Sciences of the United States of America* 103(24):9006-9011.
74. Cheng W, Arunajadai SG, Moffitt JR, Tinoco I, Jr., & Bustamante C (2011) Single-base pair unwinding and asynchronous RNA release by the hepatitis C virus NS3 helicase. *Science* 333(6050):1746-1749.
75. Moffitt JR, *et al.* (2009) Intersubunit coordination in a homomeric ring ATPase. *Nature* 457(7228):446-450.
76. Chemla YR, *et al.* (2005) Mechanism of force generation of a viral DNA packaging motor. *Cell* 122(5):683-692.
77. Wen JD, *et al.* (2008) Following translation by single ribosomes one codon at a time. *Nature* 452(7187):598-603.
78. Wang MD, *et al.* (1998) Force and velocity measured for single molecules of RNA polymerase. *Science* 282(5390):902-907.
79. Bustamante C, Smith SB, Liphardt J, & Smith D (2000) Single-molecule studies of DNA mechanics. *Curr Opin Struct Biol* 10(3):279-285.
80. Henon S, Lenormand G, Richert A, & Gallet F (1999) A new determination of the shear modulus of the human erythrocyte membrane using optical tweezers. *Biophys J* 76(2):1145-1151.
81. Raucher D & Sheetz MP (1999) Characteristics of a membrane reservoir buffering membrane tension. *Biophys J* 77(4):1992-2002.
82. Suzuki K, Sterba RE, & Sheetz MP (2000) Outer membrane monolayer domains from two-dimensional surface scanning resistance measurements. *Biophys J* 79(1):448-459.
83. Winckler B, Forscher P, & Mellman I (1999) A diffusion barrier maintains distribution of membrane proteins in polarized neurons. *Nature* 397(6721):698-701.
84. Wei X, Tromberg BJ, & Cahalan MD (1999) Mapping the sensitivity of T cells with an optical trap: polarity and minimal number of receptors for Ca(2+) signaling. *Proc Natl Acad Sci U S A* 96(15):8471-8476.
85. Kress H, *et al.* (2009) Cell stimulation with optically manipulated microsources. *Nat Methods* 6(12):905-909.
86. Berns MW, *et al.* (1989) Use of a laser-induced optical force trap to study chromosome movement on the mitotic spindle. *Proc Natl Acad Sci U S A* 86(12):4539-4543.

87. Ashkin A, Schutze K, Dziedzic JM, Euteneuer U, & Schliwa M (1990) Force generation of organelle transport measured in vivo by an infrared laser trap. *Nature* 348(6299):346-348.
88. Eriksson E, *et al.* (2007) A microfluidic system in combination with optical tweezers for analyzing rapid and reversible cytological alterations in single cells upon environmental changes. *Lab on a Chip* 7(1):71-76.
89. Ashkin A, Dziedzic JM, & Yamane T (1987) Optical Trapping and Manipulation of Single Cells Using Infrared-Laser Beams. *Nature* 330(6150):769-771.
90. Sinha RP & Hader DP (2002) UV-induced DNA damage and repair: a review. *Photochem Photobiol Sci* 1(4):225-236.
91. Macnab R & Koshland DE, Jr. (1974) Bacterial motility and chemotaxis: light-induced tumbling response and visualization of individual flagella. *J Mol Biol* 84(3):399-406.
92. Mohanty SK, Sharma M, & Gupta PK (2006) Generation of ROS in cells on exposure to CW and pulsed near-infrared laser tweezers. *Photochem Photobiol Sci* 5(1):134-139.
93. Neuman KC, Chadd EH, Liou GF, Bergman K, & Block SM (1999) Characterization of photodamage to Escherichia coli in optical traps. *Biophysical Journal* 77(5):2856-2863.
94. Liang H, *et al.* (1996) Wavelength dependence of cell cloning efficiency after optical trapping. *Biophys J* 70(3):1529-1533.
95. Landry MP, McCall PM, Qi Z, & Chemla YR (2009) Characterization of photoactivated singlet oxygen damage in single-molecule optical trap experiments. *Biophys J* 97(8):2128-2136.
96. Liu Y, *et al.* (1995) Evidence for localized cell heating induced by infrared optical tweezers. *Biophys J* 68(5):2137-2144.
97. Peterman EJ, Gittes F, & Schmidt CF (2003) Laser-induced heating in optical traps. *Biophys J* 84(2 Pt 1):1308-1316.
98. Liu Y, Sonek GJ, Berns MW, & Tromberg BJ (1996) Physiological monitoring of optically trapped cells: assessing the effects of confinement by 1064-nm laser tweezers using microfluorometry. *Biophys J* 71(4):2158-2167.
99. Gross SP (2003) Application of optical traps in vivo. *Methods Enzymol* 361:162-174.
100. Neidhardt FC, Ingraham JL, & Schaechter M (1990) *Physiology of the bacterial cell : a molecular approach* (Sinauer Associates, Sunderland, Mass.) pp xii, 506 p.
101. Chattopadhyay S, Moldovan R, Yeung C, & Wu XL (2006) Swimming efficiency of bacterium Escherichia coli. *Proceedings of the National Academy of Sciences of the United States of America* 103(37):13712-13717.
102. Rowe AD, Leake MC, Morgan H, & Berry RM (2003) Rapid rotation of micron and submicron dielectric particles measured using optical tweezers. *J. Mod. Opt.* 50(10):1539-1554.
103. Parkinson JS & Houts SE (1982) Isolation and behavior of Escherichia coli deletion mutants lacking chemotaxis functions. *J Bacteriol* 151(1):106-113.
104. Berg HC (2004) *E. coli in motion* (Springer, New York) pp xi, 133 p., [131] col. plate.
105. Misiti M, Misiti Y, Oppenheim G, & Poggi J-M (1996) *Wavelet Toolbox for Use with MATLAB* (The MathWorks, Inc., Massachusetts).
106. Korobkova EA, Emonet T, Park H, & Cluzel P (2006) Hidden stochastic nature of a single bacterial motor. *Phys Rev Lett* 96(5):058105.
107. Matthaus F, Mommer MS, Curk T, & Dobnikar J (2011) On the origin and characteristics of noise-induced Levy walks of E. coli. *PLoS One* 6(4):e18623.

108. Berg HC & Turner L (1995) Cells of Escherichia-Coli Swim Either End Forward. *Proceedings of the National Academy of Sciences of the United States of America* 92(2):477-479.
109. Cisneros L, Dombrowski C, Goldstein RE, & Kessler JO (2006) Reversal of bacterial locomotion at an obstacle. *Physical Review E* 73(3):-.
110. Macnab RM & Koshland DE, Jr. (1972) The gradient-sensing mechanism in bacterial chemotaxis. *Proc Natl Acad Sci U S A* 69(9):2509-2512.
111. Berg HC & Tedesco PM (1975) Transient response to chemotactic stimuli in Escherichia coli. *Proc Natl Acad Sci U S A* 72(8):3235-3239.
112. Spudich JL & Koshland DE, Jr. (1975) Quantitation of the sensory response in bacterial chemotaxis. *Proc Natl Acad Sci U S A* 72(2):710-713.
113. Segall JE, Block SM, & Berg HC (1986) Temporal Comparisons in Bacterial Chemotaxis. *Proceedings of the National Academy of Sciences of the United States of America* 83(23):8987-8991.
114. Shimizu TS, Tu Y, & Berg HC (2010) A modular gradient-sensing network for chemotaxis in Escherichia coli revealed by responses to time-varying stimuli. *Mol Syst Biol* 6:382.
115. Meir Y, Jakovljevic V, Oleksiuk O, Sourjik V, & Wingreen NS (2010) Precision and kinetics of adaptation in bacterial chemotaxis. *Biophys J* 99(9):2766-2774.
116. Sanders DA & Koshland DE, Jr. (1988) Receptor interactions through phosphorylation and methylation pathways in bacterial chemotaxis. *Proc Natl Acad Sci U S A* 85(22):8425-8429.
117. Hansen CH, Sourjik V, & Wingreen NS (2010) A dynamic-signaling-team model for chemotaxis receptors in Escherichia coli. *Proc Natl Acad Sci U S A* 107(40):17170-17175.
118. Lan G, Schulmeister S, Sourjik V, & Tu Y (2011) Adapt locally and act globally: strategy to maintain high chemoreceptor sensitivity in complex environments. *Mol Syst Biol* 7:475.
119. Lehmann EL & D'Abrera HJM (2006) *Nonparametrics : statistical methods based on ranks* (Springer, New York) Rev. 1st Ed pp xvi, 463 p.
120. Tu Y, Shimizu TS, & Berg HC (2008) Modeling the chemotactic response of Escherichia coli to time-varying stimuli. *Proc Natl Acad Sci U S A* 105(39):14855-14860.
121. Cluzel P, Surette M, & Leibler S (2000) An ultrasensitive bacterial motor revealed by monitoring signaling proteins in single cells. *Science* 287(5458):1652-1655.
122. Liu JD & Parkinson JS (1989) Role of CheW protein in coupling membrane receptors to the intracellular signaling system of bacterial chemotaxis. *Proc Natl Acad Sci U S A* 86(22):8703-8707.
123. Springer MS, Goy MF, & Adler J (1979) Protein methylation in behavioural control mechanisms and in signal transduction. *Nature* 280(5720):279-284.
124. Sourjik V & Berg HC (2004) Functional interactions between receptors in bacterial chemotaxis. *Nature* 428(6981):437-441.
125. Endres RG, *et al.* (2008) Variable sizes of Escherichia coli chemoreceptor signaling teams. *Mol Syst Biol* 4:211.
126. Yi TM, Huang Y, Simon MI, & Doyle J (2000) Robust perfect adaptation in bacterial chemotaxis through integral feedback control. *Proc Natl Acad Sci U S A* 97(9):4649-4653.

127. Larsen SH, Reader RW, Kort EN, Tso WW, & Adler J (1974) Change in direction of flagellar rotation is the basis of the chemotactic response in *Escherichia coli*. *Nature* 249(452):74-77.
128. Terasawa S, *et al.* (2011) Coordinated Reversal of Flagellar Motors on a Single *Escherichia coli* Cell. *Biophys J* 100(9):2193-2200.
129. Maddock JR & Shapiro L (1993) Polar location of the chemoreceptor complex in the *Escherichia coli* cell. *Science* 259(5102):1717-1723.
130. Briegel A, *et al.* (2009) Universal architecture of bacterial chemoreceptor arrays. *Proc Natl Acad Sci U S A* 106(40):17181-17186.
131. Greenfield D, *et al.* (2009) Self-organization of the *Escherichia coli* chemotaxis network imaged with super-resolution light microscopy. *PLoS Biol* 7(6):e1000137.
132. Lamanna AC, Ordal GW, & Kiessling LL (2005) Large increases in attractant concentration disrupt the polar localization of bacterial chemoreceptors. *Mol Microbiol* 57(3):774-785.
133. Wu K, Walukiewicz HE, Glekas GD, Ordal GW, & Rao CV (2011) Attractant binding induces distinct structural changes to the polar and lateral signaling clusters in *Bacillus subtilis* chemotaxis. *J Biol Chem* 286(4):2587-2595.
134. Borrok MJ, Kolonko EM, & Kiessling LL (2008) Chemical probes of bacterial signal transduction reveal that repellents stabilize and attractants destabilize the chemoreceptor array. *ACS Chem Biol* 3(2):101-109.
135. Vladimirov N, Lovdok L, Lebiedz D, & Sourjik V (2008) Dependence of bacterial chemotaxis on gradient shape and adaptation rate. *PLoS Comput Biol* 4(12):e1000242.
136. Mello BA & Tu Y (2007) Effects of adaptation in maintaining high sensitivity over a wide range of backgrounds for *Escherichia coli* chemotaxis. *Biophys J* 92(7):2329-2337.
137. Emonet T & Cluzel P (2008) Relationship between cellular response and behavioral variability in bacterial chemotaxis. *Proceedings of the National Academy of Sciences of the United States of America* 105(9):3304-3309.
138. Zhang P, Khursigara CM, Hartnell LM, & Subramaniam S (2007) Direct visualization of *Escherichia coli* chemotaxis receptor arrays using cryo-electron microscopy. *Proc Natl Acad Sci U S A* 104(10):3777-3781.
139. Khursigara CM, *et al.* (2011) Lateral density of receptor arrays in the membrane plane influences sensitivity of the *E. coli* chemotaxis response. *EMBO J* 30(9):1719-1729.
140. Zhou Q, Ames P, & Parkinson JS (2011) Biphasic control logic of HAMP domain signalling in the *Escherichia coli* serine chemoreceptor. *Mol Microbiol* 80(3):596-611.
141. Ames P, Studdert CA, Reiser RH, & Parkinson JS (2002) Collaborative signaling by mixed chemoreceptor teams in *Escherichia coli*. *Proc Natl Acad Sci U S A* 99(10):7060-7065.
142. Adler J (1966) Chemotaxis in bacteria. *Science* 153(737):708-716.
143. Shiomi D, Banno S, Homma M, & Kawagishi I (2005) Stabilization of polar localization of a chemoreceptor via its covalent modifications and its communication with a different chemoreceptor. *J Bacteriol* 187(22):7647-7654.
144. Kentner D & Sourjik V (2009) Dynamic map of protein interactions in the *Escherichia coli* chemotaxis pathway. *Mol Syst Biol* 5:238.
145. Kentner D, Thiem S, Hildenbeutel M, & Sourjik V (2006) Determinants of chemoreceptor cluster formation in *Escherichia coli*. *Molecular Microbiology* 61(2):407-417.

146. Saini S, Brown JD, Aldridge PD, & Rao CV (2008) FliZ Is a posttranslational activator of FlhD4C2-dependent flagellar gene expression. *J Bacteriol* 190(14):4979-4988.
147. Selvin PR, et al. (2008) *In Vitro and In Vivo FIONA and Other Acronyms for Watching Molecular Motors Walk, in Single-Molecule Techniques: A Laboratory Manual*, P. Selvin, T.J. Ha, Editor (Cold Spring Harbor Laboratory Press, Cold Spring Harbor, N.Y.) pp vii, 507 p.
148. Adler J & Templeton B (1967) The effect of environmental conditions on the motility of *Escherichia coli*. *J Gen Microbiol* 46(2):175-184.
149. Berg HC & Turner L (1990) Chemotaxis of bacteria in glass capillary arrays. *Escherichia coli*, motility, microchannel plate, and light scattering. *Biophys J* 58(4):919-930.
150. Joo C & Ha T (2008) *Single-Molecule FRET with Total Internal Reflection Microscopy, in Single-Molecule Techniques: A Laboratory Manual*, P. Selvin, T.J. Ha, Editor (Cold Spring Harbor Laboratory Press, Cold Spring Harbor, N.Y.) pp vii, 507 p.
151. van Dijk MA, Kapitein LC, Mameren J, Schmidt CF, & Peterman EJ (2004) Combining Optical Trapping and Single-Molecule Fluorescence Spectroscopy: Enhanced PhotoBleaching of Fluorophores. *Journal of Physical Chemistry B* 108:6479-6484.
152. Amsler CD (1996) Use of computer-assisted motion analysis for quantitative measurements of swimming behavior in peritrichously flagellated bacteria. *Anal Biochem* 235(1):20-25.